A High-Order Finite Difference Investigation of Boundary Layer Perturbations

Michael Togneri $^{\rm 1}$

February 17, 2011

¹Department of Mathematics, University of Cardiff, CF24 4AG, United Kingdom

UMI Number: U558723

All rights reserved

INFORMATION TO ALL USERS

The quality of this reproduction is dependent upon the quality of the copy submitted.

In the unlikely event that the author did not send a complete manuscript and there are missing pages, these will be noted. Also, if material had to be removed, a note will indicate the deletion.



UMI U558723

Published by ProQuest LLC 2013. Copyright in the Dissertation held by the Author.

Microform Edition © ProQuest LLC.

All rights reserved. This work is protected against unauthorized copying under Title 17, United States Code.



ProQuest LLC 789 East Eisenhower Parkway P.O. Box 1346 Ann Arbor, MI 48106-1346

Abstract

We present a new numerical treatment of the vorticity-velocity form of the governing equations of fluid motion, based on the application of compact finite differences. The mathematical formulation of these equations is discussed, as are the techniques used to discretise them. The solver thus obtained is validated against analytical solutions to model problems, and against the more physical test case of developing Tollmien-Schlichting waves in a parallelised Blasius boundary layer.

We then use this solver to examine a reduced-order model of streaks in a turbulent boundary layer. The properties of the streaks produced by the solver are discussed, with a particular focus on the means of their generation.

Following this, we examine the use of spanwise oscillation of the wall, which is known to reduce drag in turbulent boundary layers. The parameters of the oscillation (specifically its magnitude, its frequency and the phase difference between the wall motion and the streak forcing) are altered and their influence on streak development investigated. It is found that in certain cases, the modification to the basis flow by wall oscillation means that the perturbations can grow exponentially. We also investigate the effects of altering the pattern of oscillation from sinusoidal in time to a smoothed square wave or sawtooth wave. Finally, the results are reviewed and conclusions drawn, and possible extensions to the research presented in the thesis are suggested.

Acknowledgements

There are many people without whose help and support I could not have finished this work and to whom I owe thanks.

To my friends and family, and particularly to my wife Hannah.

To Dr. Christopher Davies, my supervisor, for his advice and guidance throughout the course of my study at Cardiff.

To the other staff and fellow students in the School of Mathematics, who were willing to help whenever I asked.

To EPSRC, whose generous grant made this project possible.

Tae Vince an Steve, dinnae fash.

Contents

1	Introduction & background 4						
	1.1	Turbulent boundary layers	4				
	1.2	Streaks	0.				
	1.3	Wall control	6				
2	Mathematical formulation 20						
	2.1	Governing equations	20				
		2.1.1 Two-dimensional equations	24				
		2.1.2 Nonlinear formulation	25				
		2.1.3 Secondary perturbations	26				
	2.2	Domain	28				
		2.2.1 Wall-normal transformation	28				
		2.2.2 Solution constraints	29				
	2.3	Tollmien-Schlichting waves and boundary layer eigenvalues					
	2.4	Prescribing the basic state	34				
		2.4.1 The Blasius boundary layer	34				
		2.4.2 The turbulent boundary layer	35				
	2.5	Spanwise forcing	10				
3	Numerical methods						
	3.1	General features	14				
		3.1.1 Domain discretisation	14				

		3.1.2	Compact finite differences	46			
	3.2	Vortic	city transport equation solver	47			
		3.2.1	Time stepping scheme	47			
		3.2.2	Spatial discretisation	49			
		3.2.3	Calculation of the explicit terms	50			
		3.2.4	Numerical integration	52			
	3.3	Poisso	on equation solver	58			
	3.4	Comp	olete program	62			
4	Solver validation 65						
	4.1	Order	of accuracy	65			
	4.2	Tollm	nien-Schlichting waves	67			
	4.3	Spanw	wise forcing	74			
5	Turbulent streaks 80						
	5.1	Influe	ence of k_x	84			
	5.2	Influe	ence of forcing time profile	96			
	5.3	Influe	ence of Reynolds number	105			
6	Spanwise forcing 109						
	6.1	Imple	ementation and initial case	109			
	6.2	Frozer	n oscillation	128			
	6.3	Expor	nential growth of normal modes	135			
	6.4	Effect	t of changing T^+	141			
	6.5	The o	oscillatory cycle of the wall	162			
7		nmary					

Chapter 1

Introduction & background

1.1 Turbulent boundary layers

Despite many years of investigation, our understanding of turbulent flow remains relatively incomplete; its nature and behaviour are arguably among the last major unsolved problems in classical physics. A particular area of interest is the turbulent boundary layer (TBL). At low to moderate Reynolds numbers, boundary layers are laminar, with layers of fluid at different heights from the wall travelling at different speeds and slipping smoothly over one another. At sufficiently high Reynolds numbers, boundary layer flow undergoes transition and becomes highly chaotic, with large spatial and temporal fluctuations at a wide range of scales. These fluctuations are physically associated with flow features called eddies, which exist at a range of spatial and temporal scales. The largest are on the scale of the boundary layer thickness; the smallest are on the 'Kolmogorov microscales', where the kinetic energy of the turbulent fluctuations is dissipated into heat.

Because of these chaotic fluctuations, there are no straightforward analytic solutions to the equations governing fluid motion for turbulent flows comparable to the familiar laminar flow solutions such as the Blasius and Falkner-Skan boundary layers or Poiseuille and Couette channel flows (although analytic solutions of a form resembling the structures found in turbulent boundary layers are attested in the literature [78]). In fact, it is very difficult to treat turbulent boundary layer flows with the usual governing equations at all, and we are normally forced to take a different tack: either to attempt numerical solution, or to use some kind of time averaging to modify the governing equations, which has its own set of associated difficulties.

The result of averaging the governing equations in time is to introduce several new variables representing the effects of the turbulent fluctuations. However, the governing equations of fluid flow (the Navier-Stokes equations, the continuity equation and the energy transport equation) fully and exactly express the conservation of mass, momentum and energy for a continuous Newtonian fluid. This means that the details of the turbulent fluctuations elided by the time-averaging are under-specified. Thus, we must introduce a turbulence model, which attempts to close the system by the use of model equations coupling the variables of the mean flow with the new variables, representing the stresses resulting from turbulent fluctuations.

These new variables appear as additional stress terms. Most turbulence models use the Boussinesq assumption i.e., they assume that these additional stress terms vary in direct proportion to the spatial gradients of the mean velocity. This means that these turbulent stresses are in effect treated as an increment on the viscosity, usually referred to as the turbulent, apparent or eddy viscosity, and denoted ϵ_m . Across most of a turbulent boundary layer, the eddy viscosity is much larger than the molecular viscosity. Almost every turbulence model relies at least in part on empirical data to specify the pseudo-viscous effects of the turbulent fluctuations. Note that the usual technique of time-averaging is referred to as Reynolds averaging, and thus simulations using these governing equations and turbulence models are often called Reynolds-averaged Navier-Stokes (RANS) calculations.

With a suitable choice of turbulence model, it is possible to solve the time-averaged governing equations to obtain analytic solutions for turbulent flows. The averaging means

that fluctuations below certain time-scales are smeared into the variables representing turbulent stresses; thus, these solutions do not, by their very nature, predict every detail of the flow. There are some common features that can be seen across the entire class of wall-bounded turbulent flows for which analytic solutions exist, possibly the most important of which is the division of the flow into two layers. Near the wall we find the inner region (also called the wall region) where the behaviour of the flow is strongly influenced by the proximity of the wall. Within the wall region, the area in closest proximity to the wall is almost entirely dominated by viscous effects, and is thus called the viscous sublayer. Further away from the wall we find the outer region, where the wall affects the flow only indirectly. This is often called the core region for channel and pipe flows or the wake region for boundary layer flows. For all wall-bounded flows at the same Reynolds number the mean flow profile in the wall region is identical. There is some variation in the outer region, but they nevertheless share many similar features. There is not an instant switch between the inner and outer layers, but a smooth transition. The wall-normal extent in which this transition occurs is usually referred to as the overlap or buffer region.

Even without detailed turbulence modelling, a good deal of information can be deduced about the mean turbulent boundary layer profile. The division between inner and outer regions can be thought of as a division between those parts of the boundary layer that are directly affected by the viscosity and the wall condition (which condition is embodied in the wall shear stress), and those parts which are affected only indirectly. Let us consider the inner region. We wish to specify the mean velocity profile $\bar{U}(z)$, where a bar indicates time-averaging and z is the normal distance from the wall. In addition to z, the velocity profile also depends on the wall stress τ_w and the physical properties of the fluid as embodied by the density ρ and the viscosity μ . Thus we have:

$$\bar{U} = f(z, \tau_w, \rho, \mu) \tag{1.1}$$

From the Buckingham- Π theorem, we can express this as a relationship of two dimensionless groups. Let us first define the wall-friction velocity u_{τ} as a velocity scale:

$$u_{\tau} = \sqrt{\frac{\tau_w}{\rho}} \tag{1.2}$$

Then our dimensionless relationship can be written as:

$$\frac{\bar{U}}{u_{\tau}} = f\left(\frac{u_{\tau}z}{\nu}\right) \tag{1.3}$$

Where ν is the kinematic viscosity, $\nu = \mu/\rho$. In the viscous sublayer very close to the wall, turbulent fluctuations are almost completely damped out and the shear stress is roughly constant at the wall value. Thus we can say that in the sublayer:

$$\mu \frac{\partial \bar{U}}{\partial z} = \tau_w \tag{1.4}$$

Solving this equation and rearranging gives us:

$$\frac{\bar{U}}{u_{\tau}} = \frac{u_{\tau}z}{\nu} \tag{1.5}$$

Thus there is a linear relationship between the mean velocity and the wall-normal displacement. u_{τ} is a natural velocity scale for turbulent boundary layer flows and $\delta_v = \nu/u_{\tau}$ a natural length scale. Quantities nondimensionalised by these scales are said to be in wall units, and denoted by a superscript +. Thus, equation 1.5 can be recast simply as:

$$\bar{U}^+ = z^+ \tag{1.6}$$

Having found an equation that deals with the part of the flow near the wall where viscous effects are significant, let us now consider the outer flow, where viscosity plays only an indirect role. Here, the influential parameters are the distance from the wall z, the wall stress τ_w and the fluid density ρ . In addition the boundary layer thickness, δ , is an important length scale. Note that conventionally in this layer we express the velocity profile as a 'defect' (i.e., difference) from the freestream velocity $U_{\infty} - \bar{U}$, rather than simply as the velocity itself. For this reason, the law governing the variation of velocity in the outer region is often called the velocity defect law. This can be expressed in a similar fashion to equation 1.1 as:

$$U_{\infty} - \bar{U} = g(z, \tau_w, \rho, \delta) \tag{1.7}$$

Using the Buckingham-II theorem to nondimensionalise as before, and defining a dimensionless outer length scale by $\zeta = z/\delta$, we find the relevant dimensionless relationship.

$$\frac{U_{\infty} - \bar{U}}{u_{-}} = g(\zeta) \tag{1.8}$$

As mentioned above, unlike the profile for the inner region, the details of the outer region profile vary across different flows.

We must also deal with the buffer region between the inner and outer flows. In the buffer region, the inner and outer profiles must overlap smoothly. We can use this to say that the sum of our general expressions for the inner and outer profiles must be differentiable. Using the boundary layer thickness expressed in wall units to mediate between the inner and outer variables by writing $z^+ = \zeta \delta^+$, we see that:

$$\frac{U_{\infty} - \bar{U}}{u_{\tau}} + \frac{\bar{U}}{u_{\tau}} = g\left(\frac{z}{\delta}\right) + f\left(\frac{zu_{\tau}}{\nu}\right)
U_{\infty}^{+} = g(\zeta) + f(\zeta\delta^{+})$$
(1.9)

If we differentiate twice in succession, once with respect to ζ and once with respect to δ^+ , we find:

$$f'(\zeta\delta^{+}) + \zeta\delta^{+}f''(\zeta\delta^{+}) = 0$$

$$f'(z^{+}) + z^{+}f''(z^{+}) = 0$$

$$\frac{d}{dz^{+}}(z^{+}\frac{df}{dz^{+}}) = 0$$
(1.10)

We can integrate this to show that $z^+ \cdot df/dz^+$ is equal to a constant. This constant is conventionally represented as $1/\kappa$; κ is called von Kármán's constant. If we integrate once more we find a logarithmic profile, of the form:

$$\bar{U}^{+} = f(z^{+}) = \frac{1}{\kappa} \ln z^{+} + B$$
 (1.11)

Where B is another constant of integration. The values of κ and B have been determined experimentally as $\kappa = 0.41$ and B = 5.5 (although see the results discussed by Marusic et al., which suggest that the values of these constants are not as universal as originally thought [51]).

An alternative to seeking analytic solutions for turbulent flow is to seek numerical solutions instead. There are a range of approaches to numerical solution of the equations. For flow configurations which are not amenable to analytic solutions (because of complicated geometry, for instance) we can retain the turbulence modelling but solve the model equations numerically. This is reasonably practical in terms of computational resource requirements, but more complex flow configurations are often very different from the configurations used to generate the empirical data on which the turbulence models rely. Thus, they may not predict the physics of real flows very closely.

Instead of incorporating the turbulence modelling into the numerical model, it is also possible to attempt to solve the governing equations with no time averaging, including all the details of the turbulent fluctuations. This is called direct numerical simulation (DNS), and brings in its own set of difficulties. For instance, as mentioned earlier, turbulent fluctuations occur at a wide range of scales. This means that DNS simulations require very fine resolution to capture the smallest scales, making them extremely demanding in terms of computational resources. DNS of the full governing equations for fluid motion, with no simplification, has historically been restricted for all practical purposes to relatively low Reynolds numbers. However, as more and more computing power becomes available, the range of problems amenable to investigation by DNS is growing. Wu et al. recently used a DNS approach to look at boundary layer transition, using experimentally-measured slabs of isotropic turbulence in the freestream to trigger bypass transition in an initially laminar boundary layer [80]. Although the Reynolds number of the simulated flow was still far too low for many practical purposes, it is still an important and interesting step forward. The brief note by Marusic, published in the same journal as the paper of Wu

et al., is a good summary of the current state of DNS, and clearly expresses the place of their investigation within this context [49].

There is also an intermediate choice between RANS and DNS called large eddy simulation (LES). With this technique, we explicitly calculate the turbulent fluctuations on larger temporal and spatial scales, as is done in DNS, but use turbulence modelling to account for the effects of smaller-scale fluctuations. The rationale is that smaller scales are in some sense more generic, and therefore that the difficulties in using turbulence models for broad classes of flows are somewhat alleviated.

1.2 Streaks

Although early investigations of turbulent boundary layers emphasised the statistics of turbulent fluctuations (see for instance the work of Klebanoff [42]), subsequent studies have more often focussed on particular structures within the boundary layer. Robinson's review paper gives a good overview of the various structures that have been proposed as dominating the kinematics and dynamics of the boundary layer [67]. Undoubtedly, however, one of the most important of these phenomena is the set of near-wall structures called streaks. Streaks are regions in a turbulent boundary layer where streamwise velocity is significantly higher or lower than the spanwise mean. They are relatively long in the streamwise direction (that is, in the direction aligned with the mean flow) and relatively narrow in the spanwise direction (that is, in the direction normal to the streamwise direction but still in the plane of the wall). They are found in the regions of the boundary layer closest to the wall, $z^+ < 30$. The streaks are not perfectly parallel to the wall, but are tilted upwards. It is generally accepted that streaks are of central importance to the maintenance of the energetic fluctuations of the turbulent boundary layer, although there is not a broad consensus on the details; it is certain, however, that streakiness is associated with strong transient growth of perturbations. Concomitant with these streaks are quasi-streamwise vortices; the term quasi-streamwise is used because they are tilted

in the same way as the streaks.

Streaks have been observed experimentally since at least the 1960s. Kline et al. [44] presented one of the earliest thorough investigations of streaks, and were among the first to surmise that streaks are central to the maintenance of boundary layer turbulence. They proposed a life-cycle for the streaks wherein they appear near the wall, are randomly subject to a lift-up process that pulls them out towards the main body of the flow, and then become unstable. This instability takes the form of growing oscillations and then a violent breakdown, or burst, involving the ejection of low-speed fluid outwards from the vicinity of the wall. Kline's paper proposed that the bursting of the streaks was a main contributor to the high levels of production of turbulent kinetic energy near the wall. Also noted was the apparent natural spanwise scale of the streaks: an average spanwise separation of 100 wall units was observed across a range of different flows, suggesting that the streaks scale with inner variables i.e. u_{τ} and ν . This scaling is also found in many other studies, for instance those of Kim et al. and Klewicki & Falco [41,43].

Several of the most important results from the next decade-and-a-half's investigations into streaks are summarised in the review paper of Cantwell [10]. Kline $et\ al$.'s suggestion that the streak bursts were responsible for producing a great deal of turbulent energy was confirmed, at least for $z^+<100$. The average spanwise streak spacing was confirmed as 100 wall units, but it was found that the separation of streaks was somewhat skewed, with the median spacing a little smaller at 80 wall units (see for instance the work of Smith and Metzler [71]). The wall-normal range of the streaks was found to be largely restricted to within the log-law region (i.e. the buffer region). More recently, Cossu $et\ al$ found that numerical simulations of disturbances in a turbulent boundary layer indicated that streaky structures with a spanwise spacing of approximately 80 wall units reached greater magnitude than similar structures with any other spacing [19], which suggests that structures of this spanwise scale would be observed most frequently i.e., would be the median structures.

Although the streaks are observed to scale with inner variables, that doesn't mean that the inner part of the flow where the streaks are found does not interact at all with the outer flow. See, for instance, the results of Rao et al. [63], which suggested that although the spatial scale of the streaks scale with the inner variables, the temporal frequency of the bursting events associated with the streaks scale with the outer variables, implying that the outer part of the boundary layer still influences the development of structures near the wall. More recent and very interesting results exploring the connection between large-scale structures in the outer part and streaks nearer the wall of the boundary layer are presented in the experimental investigation of Hutchins and Marusic, and the numerical results of Cossu et al. and Jiménez et al. [19,30,34,50]. Aubry et al. used a dynamical systems approach to modelling the streamwise vortices (referred to here, as occasionally elsewhere in the literature, as 'rolls') and similarly found that the pressure footprint of the outer flow is vital in determining the bursting frequency [2].

There are a number of theories as to the relationship between the quasi-streamwise vortices and the streaks. The conventional view is that the vortices act to pump low-speed fluid away from the wall towards the main flow, and similarly bring high-speed fluid down into the wall region. As these vortices are convected in the streamwise direction, they leave behind the streaks as a sort of trail of vertically-convected high- or low-speed fluid [58,74]. The vortices are often supposed to be in pairs of opposite sign, perhaps representing the legs of a hairpin vortex. Hairpin vortices are observed in many studies of turbulent boundary layers, and are thought to be created by mean-shear stretching of closed-loop vortices forming on the wall. Jeong et al. used a sophisticated criterion to educe vortical structures in a canonical numerical dataset [32], and found that their solutions contained complicated arrays of approximately streamwise vortices. The relationships and mutual influence of these vortices are very complex, but most appear to share some quite precise characteristics, including their streamwise extent and their inclination with respect to the streamwise direction. Unlike the more recent data of Wu &

Moin [80], which found veritable forests of hairpins, Jeong et al. found no hairpins in the buffer region, although they suggest that the heads or loops of the hairpins may be located outwith the wall-normal range they investigated, with the observed vortices being the legs of these structures. Whether or not this is the case, the streaks were observed to occur in the expected location in relation to the vortices. It has also been pointed out that the turbulent boundary layer naturally tends to form streak-like structures, even from random perturbations in wall-normal velocity [12], although the fact that many things could produce streaks does not preclude the vortices from being the actual source of the streaks.

Streaks are also associated with so-called 'ejection' and 'sweep' processes. In an ejection, low-speed fluid from near the wall is thrown out, and in a sweep, high-speed fluid is convected towards the wall. This obviously creates larger velocity gradients near the wall, and thus higher skin friction. Thus we can anticipate that the streaks, apart from their association with the turbulent self-maintenance, are also directly responsible for at least part of the strong friction drag in turbulent boundary layers. This is borne out by the work of Jeon et al., who performed statistical analysis on skin friction data from a series of DNS simulations and found that regions of high friction on the wall correlated well with the quasi-streamwise vortices, and thus with the streaks [31]. Orlandi and Jiménez's simplified 2D model of near-wall vortices also implied that there is a connection between the vortices, the streaks and the generation of high skin friction values [56].

The mechanisms by which the streaks grow and the mechanisms by which the quasistreamwise are generated vortices are not fully settled; one possibility is that the streaks themselves generate the streaks. This idea seems plausible but has not been rigorously proven, although several hypotheses have been proposed. Possibly the most common idea is that the wall-normal vorticity profiles that arise from alternating high-speed and low-speed streaks are prone to inflectional instabilities. Exponential growth of these instabilities would produce wall-normal rather than streamwise vortices, but the shear of the mean profile would tilt these to produce the expected quasi-streamwise alignment. This cycle is explored in some detail by Hamilton et al., who looked at turbulence in a Couette flow [28]. In order to exclude extraneous detail, they simulated turbulence in a streamwise- and spanwise-periodic box, then reduced the size of this box to the minimum size that permitted self-regenerating turbulence. That such a limit exists implies there is a natural scale to wall-bounded turbulence. As might be expected from the natural spacing of the streaks, turbulence was found to eventually decay for domains narrower than 100 wall units in the spanwise direction. This investigation also found a natural time scale to the turbulence cycle, with streaks being created, breaking down and then being recreated over a time period of $t^+ \approx 100$. It was found that the streaky profiles are indeed linearly unstable, but that the growth in a real flow, developing in time, is significantly greater than the growth rate found by freezing the background flow and allowing perturbations to grow as normal modes. One of the most important suggestions was that the individual processes of the turbulence regeneration cycle (streak generation, streak breakdown, vortex formation) each have, for a given spatial scale, a particular temporal scale. The natural length scale of the near wall structures is the smallest spatial scale at which the temporal scales of all the processes coincide appropriately. Thus, even although structures of the right type occur at a wide range of scales, only those at the correct scale are reinforced and therefore observed in real turbulent boundary layers. Jiménez et al. used a similar technique to isolate an individual self-sustaining unit of near-wall turbulence [33, 35, 36]. This allowed several insights into the complex interactions of near-wall structures that dominate turbulent dynamics. Waleffe later showed that a similar selfsustaining process occurred in a sinusoidal shear flow, with both no-slip and free-slip conditions at the wall [79], which suggests that the cycle may be generic in wall-bounded shear flows.

Alternatively, Schoppa and Hussain proposed a transient growth mechanism for streaks which are steady to normal-mode perturbations [70]. This growth is algebraic but sufficiently strong in the short term that it may cause normal-mode-steady streaks to grow to an amplitude where nonlinear effects become significant before the streak perturba-

tions begin to decay exponentially. This mechanism of streak growth creates a sheet of streamwise vorticity which eventually rolls up to form the quasi-streamwise vortices. Note that it is possible that more than one self-maintaining turbulent cycle exists theoretically; among all possible cycles, the one that produces the strongest turbulence will be the one that is most often observed physically.

A further candidate for the source of the quasi-streamwise vortices is that, in addition to generating the streaks, they generate their own successors, a process sometimes called parent-child vortex generation. If there is a streamwise vortex situated above a wall, it will induce on the wall a region of vorticity having the opposite sign to itself. The same lift-up mechanism by which the vortices generate the streaks then (by this proposed mechanism) lifts these zones of induced vorticity away from the wall, which then roll up to create new vortices even as the vortices that originally create them dissipate or are annihilated by turbulent fluctuations. This hypothesis has somewhat fallen out of favour, since little evidence has been found to back it up; Jiménez and Pinelli found that suppressing the physical processes necessary for this did not prevent the formation of new vortices, while Orlandi and Jiménez found that in a two-dimensional model of turbulent streaks and vortices, the vorticity sheets near the wall would never roll up to form new vortices [36,56].

The above discussion outlines the current state of understanding of turbulent boundary layers, but it should be borne in mind that much of the knowledge we have gained is highly conjectural, and that even many quite fundamental aspects of turbulent boundary layer behaviour (for instance, is the von Kármán constant truly a constant?) are still subject to continued scrutiny. The recent review paper by Marusic *et al.* examines the state of the art in many parts of boundary layer studies, and demonstrates the uncertain nature of many of the tentative conclusions that have been drawn about turbulent flow [51].

1.3 Wall control

Having established that streaks are of importance in maintaining turbulent boundary layers and generating large values of skin friction, we may ask if there is some way in which we can influence the development of the streaks in order to control turbulence. The ultimate goal of such a task would be either to inhibit turbulence, so that we could reduce friction drag in turbulent boundary layers, or to strengthen turbulence, in order to prevent or delay boundary layer separation. A range of forcing strategies have been investigated, including riblets aligned with the mean flow (see Choi [15]), suction-injection devices (see the paper of Kim which summarises many years of numerical investigation, or the work of Choi et al. [13,40]) and spanwise oscillation of the wall. More exotic approaches such as the use of electrohydrodynamic Lorentz forces for conducting fluids (see for instance the work of Breuer et al. [7,8]), seeding the flow with microbubbles (modelled numerically by Xu et al. as a body force [81]) or injecting polymers into the fluid have also been attempted. There are several very good review papers discussing various aspects of the mechanisms used to reduce drag in turbulent boundary layers [38,39]. In addition to the fluid mechanics behind the techniques used to influence the turbulent boundary layer, significant attention has been paid to the development of appropriate control systems [4, 25, 52]. Sophisticated control schemes are relevant if we want to develop a mechanism for manipulating the turbulent flow that responds to the instantaneous condition of the flow; thus we would need not only a means of influencing the flow but a means of measuring it as well, which introduces its own set of difficulties.

The control mechanism we intend to investigate is spanwise oscillation of the wall. There are many studies that implement this forcing method, both numerical and experimental. The pioneering numerical study was by Jung et al. [1,37], who built on earlier studies by (among others) Moin et al. examining the effects of a constant transverse motion of the wall [53]. Experimental studies of the same phenomena were carried out at around the same time, for instance those of Laadhari et al. [45], and continue to be pursued.

Although both methods of investigation find that oscillation of the wall can significantly reduce drag in turbulent boundary layers, DNS investigations tend to predict larger reductions than experiments: ~ 40% compared to ~ 25%, see for instance the discussion by Ricco and Wu [66]. Quadrio and Ricco suggest that at least part of this discrepancy may be caused by experimental measurements being made at locations where the spatial transient effects of the leading edge of the oscillating section of wall are still significant [60]. In addition to the mean flow effect of reduced drag, most studies agree that changes to statistical measures of the flow are alse found, including reductions in turbulence production, magnitude of turbulent fluctuations and an upward shift of the logarithmic part of the mean velocity profile. This shift is indicative of a thickening of the viscous sublayer and is characteristic of drag reduction in turbulent flows. Rotating a pipe about its flow axis has been found to have similar results on turbulent pipe flows to wall oscillations in channel and flat plate boundary layer flows; see for instance the work of Orlandi and Fatica, or Quadrio and Sibilla [55,62].

The principle advantages offered by spanwise oscillation over other control methods are twofold. Firstly, it requires no feedback, so we do not need to deal with the additional layer of complexity added by flow detection and control schemes, and secondly, it is a mechanism that works by manipulating the entire flow. Therefore, it does not need to be applied on the scale of the boundary layer structures themselves, but can instead be much larger. This is an advantage at higher Reynolds numbers (aircraft flight Reynolds numbers, for instance) where the structures of the boundary layer become much smaller and therefore creating devices on the same scale becomes much more difficult.

In addition to the obvious parameters of the wall motion (e.g. amplitude or frequency), a potentially useful means of characterising the wall motion is through the use of the parameter S, as introduced by Choi et al. [14] and investigated by Ricco and Quadrio [61,65]. This parameter is used in an attempt to find a straightforward relationship between the wall oscillation (as characterised by its amplitude and frequency, or equivalents) and the

amount of drag reduction. Its definition is not fully analytic, but instead incorporates some empirical data. This data is selected in order to give a best fit (quadratic for Choi et al., linear for Ricco and Quadrio) to the drag reduction data. The results presented in Quadrio and Ricco's 2004 paper, in particular, show a remarkable linear fit for drag reduction on this parameter, on the condition that they restrict themselves to wall oscillations characterised by a period $T^+ < 150$. In common with many investigations of spanwise wall oscillations, they find that an optimum drag reduction is obtained with an oscillatory period of $T^+ \approx 100 - 125$.

A common explanation for the effectiveness of wall oscillations in reducing turbulent drag is directly related to the streaks. Most studies find that the spanwise velocities induced by the wall motion are very well approximated by the laminar oscillatory Stokes problem. It is theorised that the layer of spanwise-moving fluid (the so-called Stokes layer) induced by the spanwise motion of the wall breaks up the spatial coherence of the quasi-streamwise vortices and the streaks, so that instead of pumping low-speed fluid from near the wall into the low-speed streaks and high-speed fluid from further out in the boundary layer into the high-speed streaks, the vortices do the opposite, and thus the streak formation is inhibited. This hypothesised mechanism is predicated on the wall-normal separation between the vortices and the streaks, such that a Stokes layer of the appropriate thickness will induce a relative separation. This explanation, or similar, is advanced by many different researchers [3, 16, 23, 24].

Onorato et al. propose a different mechanism for turbulent drag reduction by wall oscillation [54]. They suggest that the oscillating Stokes layer induced by the wall motion works to annihilate the wall-normal vorticity that flanks the low-speed streaks, thus hindering the process by which the streaks generate new streamwise vortices. Of course, given the highly interactive nature of the near-wall vortices and streaks and their complex relationships, which are not fully understood, it is quite possible that the wall oscillation might interfere with more than one part of the autonomous turbulence cycle. Furthermore, interfering with any part of the cycle will have a knock-on effect on other parts, which in an experiment or a complete DNS simulation may make it difficult to disentangle the direct effects of the oscillation from the indirect ones. In this thesis, we intend to use a reduced-order model of streaks to try to elucidate some of the mechanisms by which spanwise wall oscillations manipulate near-wall structures in turbulent boundary layers.

Chapter 2

Mathematical formulation

2.1 Governing equations

We seek a suitable model for investigating the behaviour of small disturbances to flatplate boundary layer solutions, with an eye towards producing a reduced-order model of streaks in turbulent boundary layers. The formulation that we use has been used before, and is described quite thoroughly in a comprehensive paper by Davies and Carpenter [22]; its application to various problems of interest, including the use of compliant walls to influence disturbance growth in flat-plate and rotating-disc boundary layers is presented in a later paper by Davies as well as the references therein [20]. Since this formulation is at the heart of our work here we will nevertheless discuss it in some detail. We begin by considering the three-dimensional nondimensionalised Navier-Stokes equations for an incompressible Newtonian fluid.

$$\frac{\partial \mathbf{U}}{\partial t} + (\mathbf{U} \cdot \nabla)\mathbf{U} = -\nabla P + \frac{\Delta \mathbf{U}}{Re}$$
 (2.1)

Where Re, the Reynolds number, is defined as:

$$Re = \frac{U_{\infty}d}{\nu} \tag{2.2}$$

With ν the kinematic viscosity of the fluid, d an appropriate length scale and U_{∞} the

freestream velocity (i.e., the flow velocity that would exist in the absence of the plate). The Navier-Stokes equations can be thought of as momentum transport equations, and by taking the curl of the Navier-Stokes equations we can change them into vorticity transport equations (VTEs).

$$\frac{\partial \Omega}{\partial t} + (\mathbf{U} \cdot \nabla)\Omega = (\Omega \cdot \nabla)\mathbf{U} + \frac{\Delta \Omega}{Re}$$
 (2.3)

The principal advantage of solving the VTEs instead of the Navier-Stokes equations is the elimination of pressure. Finding suitable boundary conditions for pressure has been known to present considerable difficulties [73]; finding appropriate boundary conditions for vorticity has also proved problematic historically, but by using integral conditions (as described in section 2.2.2) this problem is overcome. Furthermore, since we are investigating boundary layer stability, solving for the vorticity field directly is helpful in that vortical features are thought to be central to mechanisms of the self-sustaining turbulence cycle.

We are faced with a problem in attempting to solve these equations. There are three VTEs, one for each of the Cartesian spatial dimensions. However, there are six variables: three components of vorticity, Ω , and three components of velocity, U. We must therefore find some closure for the system of equations, a relationship between velocity and vorticity. A very simple relationship that immediately suggests itself is the definition of vorticity:

$$\mathbf{\Omega} = \nabla \times \mathbf{U} \tag{2.4}$$

However, as will become clear in the chapter discussing the numerical techniques employed for solving these equations, we will be solving the VTEs to obtain the components of velocity, and solving the equations we use to close the system to obtain the components of velocity. It is therefore convenient to take the curl of the definition of vorticity, as this decouples the velocity components. By taking into account the continuity condition,

 $\nabla \cdot \mathbf{U} = 0$, we are left with three Poisson equations.

$$\Delta \mathbf{U} = -\nabla \times \mathbf{\Omega} \tag{2.5}$$

We are interested in the development of perturbations to known boundary layer solutions. To that end, we will represent each of the solution variables as the sum of a basis solution, known to satisfy the governing equations, and a small perturbation to that solution. Thus, we write:

$$\Omega = \Omega_B + \omega
\mathbf{U} = \mathbf{U}_B + \mathbf{u}$$
(2.6)

And we substitute these expressions into the governing equations. Since the basis solution satisfies the governing equations by definition, all terms involving only the basis variables can be eliminated. If we assume that the perturbations are infinitesimally small, then we can linearise by eliminating the products of perturbation terms. The governing equations for the perturbation variables can therefore be written:

$$\frac{\partial \boldsymbol{\omega}}{\partial t} + (\mathbf{U}_B \cdot \nabla) \boldsymbol{\omega} + (\mathbf{u} \cdot \nabla) \boldsymbol{\Omega}_B = (\boldsymbol{\Omega}_B \cdot \nabla) \mathbf{u} + (\boldsymbol{\omega} \cdot \nabla) \mathbf{U}_B + \frac{\Delta \boldsymbol{\omega}}{Re}$$

$$\Delta \mathbf{u} = -\nabla \times \boldsymbol{\omega}$$
(2.7)

Since we are interested in boundary layer flows, further simplifications are possible. Let us assume that the basis solution for the boundary layer takes the form:

$$\mathbf{U}_{B} = (U_{B}(z), 0, 0)$$

$$\mathbf{\Omega}_{B} = (0, U'_{B}(z), 0)$$
(2.8)

Where z is the spatial dimension normal to the wall that creates our boundary layer and the prime indicates differentiation with respect to this dimension. In doing this we have assumed that there is no development of the boundary layer in the direction of the mean flow i.e. we have assumed a parallelised flow. Our VTEs can then be rewritten as follows:

$$\frac{\partial \omega_x}{\partial t} + U_B \frac{\partial \omega_x}{\partial x} - U_B' \frac{\partial u_y}{\partial x} = \frac{\Delta \omega_x}{Re}$$
 (2.9)

$$\frac{\partial \omega_x}{\partial t} + U_B \frac{\partial \omega_x}{\partial x} - U_B' \frac{\partial u_y}{\partial x} = \frac{\Delta \omega_x}{Re}$$

$$\frac{\partial \omega_y}{\partial t} + U_B \frac{\partial \omega_y}{\partial x} - U_B' \frac{\partial u_y}{\partial y} + U_B'' u_z = \frac{\Delta \omega_y}{Re}$$
(2.9)

$$\frac{\partial \omega_z}{\partial t} + U_B \frac{\partial \omega_z}{\partial x} - U_B' \frac{\partial u_z}{\partial y} = \frac{\Delta \omega_z}{Re}$$
 (2.11)

The subscripts are used to mark the different components according to which spatial dimension they are aligned with. Thus we have obtained a set of six equations to solve for six variables. However, it is possible to make life slightly easier for ourselves by a division of our solution variables into primary and secondary groups. In this scheme, the secondary variables are defined explicitly in terms of the primary variables. Thus, we need only solve for the primary variables, reducing the number of governing equations we need to solve. The primary variables are $\{\omega_x, \omega_y, u_z\}$ and the secondary variables $\{u_x, u_y, \omega_z\}$. Our secondary variables can be defined as:

$$u_{x}(z) = -\int_{z}^{\infty} \left(\omega_{y} + \frac{\partial u_{z}}{\partial x}\right) d\bar{z}$$

$$u_{y}(z) = \int_{z}^{\infty} \left(\omega_{x} - \frac{\partial u_{z}}{\partial y}\right) d\bar{z}$$

$$\omega_{z}(z) = \int_{z}^{\infty} \left(\frac{\partial \omega_{x}}{\partial x} + \frac{\partial \omega_{y}}{\partial y}\right) d\bar{z}$$

$$(2.12)$$

With \bar{z} a dummy variable. The definitions of u_x and u_y are obtained by integrating the definitions of ω_y and ω_x , respectively, along the wall-normal dimension. The definition of ω_z is obtained by integrating the solenoidality condition on vorticity in a similar fashion. Note that these definitions make use of the boundary condition that all variables go to zero infinitely far from the wall. Boundary conditions are discussed in more detail in section 2.2.2.

In the spanwise dimension, we apply a Fourier transformation:

$$f(x, y, z, t) = \int_{-\infty}^{\infty} f_{\beta}(x, z, t) e^{i\beta y} d\beta$$
 (2.13)

Where f is any solution variable. Since we have linearised our governing equations, each Fourier wavenumber is independent of all others. Thus we can investigate the stability of our boundary layer solutions to perturbations of a particular spanwise wavenumber, β , by solving the following set of equations:

$$\frac{\partial \omega_x}{\partial t} + U_B \frac{\partial \omega_x}{\partial x} - U_B' \frac{\partial u_y}{\partial x} = \frac{(\tilde{\Delta} - \beta^2)}{Re} \omega_x \tag{2.14}$$

$$\frac{\partial \omega_y}{\partial t} + U_B \frac{\partial \omega_y}{\partial x} - i\beta U_B' u_y + U_B'' u_z = \frac{(\tilde{\Delta} - \beta^2)}{Re} \omega_y$$
 (2.15)

$$(\tilde{\Delta} - \beta^2)u_z = i\beta\omega_x - \frac{\partial\omega_y}{\partial x}$$
 (2.16)

Which we obtain by substituting the Fourier transformation in equation 2.13 into equations 2.9, 2.10 and the wall-normal component of the velocity Poisson equation in 2.7. Here, $\tilde{\Delta}$ is a modified Laplacian:

$$\tilde{\Delta} = \left(\frac{\partial^2}{\partial x^2} + \frac{\partial^2}{\partial z^2}\right)$$

Note that the subscript β used in the definition of the Fourier transformation has been dropped in the above statement of the governing equations to aid comprehensibility.

2.1.1 Two-dimensional equations

A simpler two-dimensional form of the equations can also be derived. In this formulation, we have only the streamwise and wall-normal dimensions. One upshot of this is that vorticity is no longer a vector quantity, but a scalar. The two-dimensional vorticity can be defined, in a way analogous to the spanwise component of three-dimensional vorticity, as:

$$\omega = \frac{\partial u_x}{\partial z} - \frac{\partial u_z}{\partial x} \tag{2.17}$$

Note that we have retained from the three-dimensional formulation the convention that x denotes the streamwise direction and z the wall-normal. This (x, z) pair is somewhat

unusual but hopefully will help avoid confusion in comparing 2D and 3D results. The twodimensional VTE is obtained by subtracting the x-derivative of the wall-normal Navier-Stokes equation from the z-derivative of the streamwise Navier-Stokes equation. We can also think of it as simply being the only non-zero component of the three-dimensional VTE if we assume spanwise uniformity and $u_y = 0$. If we then distinguish between basis and perturbation variables, as in equation (2.6), assume the same form for the basis flow as in equation (2.8), and finally linearise as before, we obtain the following two-dimensional VTE:

$$\frac{\partial \omega}{\partial t} + U_B \frac{\partial \omega}{\partial x} + U_B'' u_z = \frac{\Delta \omega}{Re}$$
 (2.18)

We see that this is similar to the three-dimensional VTE for the spanwise component of vorticity, equation (2.10). The equation above contains two solution variables, ω and u_z ; to close the system we use a Poisson equation for u_z . This is derived by differentiating the definition of the two-dimensional vorticity with respect to x and applying the continuity condition:

$$\Delta u_z = -\frac{\partial \omega}{\partial x} \tag{2.19}$$

2.1.2 Nonlinear formulation

If we introduce the perturbation decomposition 2.6 into the basic vector form of the VTEs 2.3, but don't linearise, we obtain a nonlinear formulation. With a nonlinear formulation, it makes little sense to investigate a single spanwise mode. The assumption that all solution variables vary as $e^{i\beta y}$ is unsuitable, since nonlinear multiplication of the perturbation variables would result in the different modes (that is, different values of β) influencing one another, and disentangling a single mode becomes very difficult.

We can, however, investigate a certain limited sort of nonlinearity. Ordinarily, if boundary layer perturbations have grown to the stage that nonlinear effects have become significant,

then the flow has also become three-dimensional. However, if we artificially suppress three-dimensionality by setting all spanwise derivatives to zero (equivalent to taking $\beta = 0$), then we can investigate a subset of nonlinear effects. Doing this yields the following streamwise and spanwise VTEs:

$$\frac{\partial \omega_x}{\partial t} + (U_B + u_x) \frac{\partial \omega_x}{\partial x} + u_z \frac{\partial \omega_x}{\partial z} = U_B' \omega_z + \omega_x \frac{\partial u_x}{\partial x} + \omega_z \frac{\partial u_x}{\partial z} + \frac{\Delta \omega_x}{Re}$$
(2.20)

$$\frac{\partial \omega_{y}}{\partial t} + (U_{B} + u_{x}) \frac{\partial \omega_{y}}{\partial x} + u_{z} \frac{\partial \omega_{y}}{\partial z} + U_{B}'' u_{z} = \omega_{x} \frac{\partial u_{y}}{\partial x} + \omega_{z} \frac{\partial u_{y}}{\partial z} + \frac{\Delta \omega_{y}}{Re}$$
(2.21)

Since $\mathbf{U}_B = (U_B(z), 0, 0)$ and $\mathbf{\Omega}_B = (0, U_B'(z), 0)$, we would retain only one term each from $(\mathbf{U}_B \cdot \nabla)\boldsymbol{\omega}$ and $(\mathbf{\Omega}_B \cdot \nabla)\mathbf{u}$. But, since we are assuming spanwise uniformity, all spanwise derivatives go to zero, meaning that the single term from $(\mathbf{\Omega}_B \cdot \nabla)\mathbf{u}$ in fact vanishes altogether. This is also the reason only two of three terms have been retained from $(\mathbf{u} \cdot \nabla)\boldsymbol{\omega}$ and $(\boldsymbol{\omega} \cdot \nabla)\mathbf{u}$. Since there is no x-component in $\mathbf{\Omega}_B$, $(\mathbf{u} \cdot \nabla)\mathbf{\Omega}_B$ makes no contribution to the streamwise VTE, and we can make a similar statement for $(\boldsymbol{\omega} \cdot \nabla)\mathbf{U}_B$ in the spanwise VTE. In both of these cases, since our basis flow has been parallelised, we need only include the wall-normal derivatives of basis variables.

2.1.3 Secondary perturbations

There is another method that allows us to investigate nonlinear, or at least quasi-nonlinear, phenomena: the introduction of a secondary perturbation. In this method, we set $\beta=0$ and then solve either the nonlinear formulation described in section 2.1.2 or the linear formulation to get a spanwise-uniform solution to the perturbation equations. Let us call the velocity and vorticity fields of this solution \mathbf{u}_1 and $\boldsymbol{\omega}_1$ respectively. This solution is then scaled appropriately and added to our basis solution to get a new, secondary basis solution, defined as $\mathbf{U}_S = \mathbf{U}_B + \epsilon \mathbf{u}_1$ and $\boldsymbol{\Omega}_S = \boldsymbol{\Omega}_B + \epsilon \boldsymbol{\omega}_1$, where ϵ is the scaling factor. Note that, unlike the primary basis flows, there is more than one nonzero component of the basis variables, so we introduce the notation $\mathbf{U}_S = (U_{Sx}, U_{Sy}, U_{Sz})$ and $\boldsymbol{\Omega}_S = (\Omega_{Sx}, \Omega_{Sy}, \Omega_{Sz})$. We then solve the perturbation equations again for the secondary

perturbation solution, \mathbf{u}_2 and $\boldsymbol{\omega}_2$, with \mathbf{U}_S and $\boldsymbol{\Omega}_S$ as our new basic state. In short, we are using our linearised formulation to create a new basis, then linearising around this basis a second time.

The Poisson equation for the secondary component of u_z remains unchanged, but because of additional non-zero terms in \mathbf{U}_S and $\mathbf{\Omega}_S$ that do not appear in \mathbf{U}_B and $\mathbf{\Omega}_B$, far more terms representing convection and vortex stretching appear in the VTEs. If we replace \mathbf{U}_B and $\mathbf{\Omega}_B$ with \mathbf{U}_S and $\mathbf{\Omega}_S$ in equations 2.7, then we can recast the VTEs that are solved, after some manipulation, as:

$$\frac{\partial \omega_{2x}}{\partial t} + U_{Sx} \frac{\partial \omega_{2x}}{\partial x} + i\beta U_{Sy} \omega_{2x} + U_{Sz} \frac{\partial \omega_{2x}}{\partial z} + u_{2x} \frac{\partial \Omega_{Sx}}{\partial x} + u_{2z} \frac{\partial \Omega_{Sx}}{\partial z}
= -\Omega_{Sx} \left(i\beta u_{2y} + \frac{\partial u_{2z}}{\partial z} \right) + i\beta \Omega_{Sy} u_{2x} + \Omega_{Sz} \left(\omega_{2y} + \frac{\partial u_{2z}}{\partial x} \right)
+ \omega_{2x} \frac{\partial U_{Sx}}{\partial x} + \omega_{2z} \frac{\partial U_{Sx}}{\partial z} + \frac{(\tilde{\Delta} - \beta^2)\omega_{2x}}{Re}$$
(2.22)

$$\frac{\partial \omega_{2y}}{\partial t} + U_{Sx} \frac{\partial \omega_{2y}}{\partial x} + i\beta U_{Sy} \omega_{2y} + U_{Sz} \frac{\partial \omega_{2y}}{\partial z} + u_{2x} \frac{\partial \Omega_{Sy}}{\partial x} + u_{2z} \frac{\partial \Omega_{Sy}}{\partial z}
= i\beta \Omega_{Sx} u_{2x} + i\beta \Omega_{Sy} u_{2y} + \Omega_{Sz} (i\beta u_{2z} - \omega_{2x}) + \omega_{2x} \frac{\partial U_{Sy}}{\partial x} + \frac{(\tilde{\Delta} - \beta^2)\omega_{2y}}{Re}$$
(2.23)

Here, β is the spanwise wavenumber of the variation in the secondary perturbation variables. The equations have been recast so as to minimise the number of terms involving secondary variables that need to be calculated. Note that 'secondary' is used with two meanings in this work, referring both to the variables that are not calculated directly (as defined by equation 2.12) and to the secondary perturbations from the formulation given here.

2.2 Domain

We need to choose a domain suitable for the problem we are interested in: the development of small disturbances in a flat-plate boundary layer. The most obvious choice is a semi-infinite Cartesian domain over an infinite flat plate. The spatial dimensions are x, which is aligned with the direction of the basis flow, and which we call the streamwise direction; y, orthogonal to x in the plane of the wall, which we call the spanwise direction; and z, the wall-normal direction.

We define streamwise limits on the domain such that the all points in domain satisfy $0 < x < L_x$. We call the boundary at x = 0 the inlet and the boundary at $x = L_x$ the outlet. In the wall normal direction, the domain stretches from z = 0 at the wall to infinity. A transformation used to map the semi-infinite wall-normal domain to a finite one is discussed in section 2.2.1.

As mentioned previously, in the three-dimensional case a Fourier transformation is applied to the spanwise dimension, and only individual modes are investigated in any given solution. Thus we can think of our spanwise domain as being periodic and infinite in extent.

2.2.1 Wall-normal transformation

It is intended to use finite difference methods to solve the governing equations. However, finite differences cannot be straightforwardly applied to a semi-infinite domain. Thus, a transformation is applied to the wall-normal coordinate. The transformation used maps $z \mapsto \eta$ such that all η -coordinates belong to the range [0,1]:

$$\eta = \frac{l}{l+z} \tag{2.24}$$

l here is a parameter that controls the stretchedness of the transformed wall-normal domain compared to the untransformed domain.

This transformation for the numerical method changes the ways in which the wall-normal derivatives and integrals are treated. Consider:

$$\frac{\partial f}{\partial z} = -\frac{\eta^2}{l} \frac{\partial f}{\partial \eta} \tag{2.25}$$

$$\frac{\partial z}{\partial z^2} = \frac{l}{l^2} \frac{\partial \eta}{\partial \eta^2} + \frac{2\eta^3}{l^2} \frac{\partial f}{\partial \eta}$$
 (2.26)

Consider also:

$$\int_{z}^{\infty} f d\bar{z} = l \int_{0}^{\eta} \frac{f}{\bar{\eta}^{2}} d\bar{\eta} \tag{2.27}$$

With \bar{z} and $\bar{\eta}$ being dummy variables. Specifically:

$$\int_0^\infty f dz = l \int_0^1 \frac{f}{\eta^2} d\eta \tag{2.28}$$

In these expressions, f stands in for any arbitrary function. Note that since (per equation 2.24) $\eta \to 0$ as $z \to \infty$, we can see from equation 2.25 that in order for $\partial f/\partial \eta$ to remain bounded in the limit $\eta \to 0$, $\partial f/\partial z$ must vanish at an infinite distance from the solid boundary. Similar considerations apply for the higher-order wall-normal derivatives.

2.2.2 Solution constraints

We are interested in the growth or decay of perturbations to a boundary layer solution. We will introduce these perturbations at some particular point or region of the domain. Since we have a semi-infinite wall-normal domain, we can say that any point in the domain is infinitely separated from the upper boundary (i.e. $z \to \infty$). This is intended to be a model of a physical problem, so we apply the condition that all model variables go to zero infinitely far from the wall. However, note that, although pressure does not explicitly appear in our formulation, for an incompressible fluid pressure changes propagate infinitely fast.

We also apply a zero boundary condition on all primary variables at the inlet. It is expected that the upstream influence of the perturbations will be relatively small, so this condition should not introduce any difficulties as long as the perturbations are located, in some sense, sufficiently far downstream of the inlet.

The outlet condition is more problematic. If we assume that our perturbations will grow or decay in an oscillatory manner, then a possible appropriate boundary condition is:

$$\frac{\partial^2 f}{\partial x^2} = -\alpha^2 f,\tag{2.29}$$

where f is any perturbation variable. This is consistent with a sinusoidal variation of wavenumber α in the streamwise direction. There is now a further problem: the selection of a suitable α . In certain cases, such as the Tollmien-Schlichting waves discussed in section 4.2 we will have an anticipated wavenumber, which allows us to specify α . Elsewhere, for transiently growing solutions which we do not expect to pass through the outflow boundary, we set $\alpha = 0$.

At the wall, all components of velocity are fully specified by the no-slip condition. However, there is no natural condition on vorticity at the wall. In order to overcome this difficulty, we apply an integral condition to vorticity, as discussed in the paper of Davies and Carpenter [22]. This specifies constraints on the variation of vorticity along any given wall normal line by taking the integral of the definition of vorticity along this line. For the components of vorticity which are primary variables, we have the following integral conditions:

$$\int_{0}^{\infty} \omega_{x} dz = \int_{0}^{\infty} \left(\frac{\partial u_{z}}{\partial y}\right) dz + \hat{u}_{y}$$

$$\int_{0}^{\infty} \omega_{y} dz = \hat{u}_{x} - \int_{0}^{\infty} \left(\frac{\partial u_{z}}{\partial x}\right) dz$$
(2.30)

Here the hatted variables represent the specified wall velocities. The integral condition on vorticity in the two-dimensional case is identical to the three-dimensional integral condition on ω_y . These constraints are equivalent to the no-slip condition on velocity.

2.3 Tollmien-Schlichting waves and boundary layer eigenvalues

In experimental investigations of boundary layer transition, growing waves, referred to as Tollmien-Schlichting waves, are frequently observed [68]. It is surmised that these are caused by the selective amplification of perturbations present in the outer flow. The attempt to describe Tollmien-Schlichting waves analytically through mathematical models of the boundary layer is part of primary stability theory, and it is these analytic solutions that we will use to verify the numerics. One of the most important tools in primary stability theory is the classical Orr-Sommerfeld equation, which we derive by assuming the existence of wavelike solutions to the equation [69]:

$$\left[\left(\frac{\partial}{\partial t} \Delta + U_B \frac{\partial}{\partial x} \Delta - U_B'' \frac{\partial}{\partial x} - \frac{\Delta^2}{Re} \right) \right] u_z = 0$$
 (2.31)

This equation is obtained by eliminating pressure from the linearised and parallelised perturbation form of the wall-normal Navier-Stokes equation. If we specify the wavelike form of the solution to be:

$$u_y(x, y, z, t) = \tilde{u}_y(z)e^{i(\alpha x + \beta y - \gamma t)}, \qquad (2.32)$$

then the classical Orr-Sommerfeld equation drops out:

$$\left[(-i\gamma + i\alpha U_B)(D^2 - \alpha^2 - \beta^2) - i\alpha U_B'' + \frac{(D^2 - \alpha^2 - \beta^2)^2}{Re} \right] \tilde{u}_y = 0$$
 (2.33)

Here, D is a differential operator denoting differentiation with respect to z. This equation, together with suitable boundary conditions, defines an eigenvalue problem. If we assume that the flow is specified (meaning that we know the values of Re and the flow profile $U_B(z)$) and we are given a spanwise wavenumber β , then we are interested in solving this

eigenvalue problem for either γ , the temporal frequency, or α , the streamwise wavenumber. There is no restriction to real frequencies or wavenumbers in general. Traditionally, however, the approach has been to assume a real α and find the corresponding γ eigenvalues. This corresponds to having a perturbation that is uniform throughout space and seeing whether it grows (i.e. $Im(\gamma) < 0$) or decays $(Im(\gamma) > 0)$ in time. Solving for γ rather than α is also more straightforward in that γ appears only in the order 1, whereas α appears in the order 4.

However, this is not necessarily very realistic; or at least, it does not necessarily correspond very well to the types of perturbation that are more often observed empirically. Typically, we will have a perturbation of specified temporal frequency which evolves in space. In the Orr-Sommerfeld equation, this corresponds to a known real γ and a complex α that we must calculate. Unfortunately, as mentioned above, this is made difficult by the higher order α terms in the eigenvalue problem.

In order to obtain complex spatial eigenvalues for validation of numerical results, the method used by Thomas [75] is applied, and we briefly summarise it here. This begins by assuming a wavelike solution to the two-dimensional VTE, equation (2.18), resulting in an Orr-Sommerfeld-like equation. In order to deal with the u_z term, we use a streamfunction ϕ , defined such that:

$$u_z = -\frac{\partial \phi}{\partial x}; u_x = \frac{\partial \phi}{\partial z} \tag{2.34}$$

Thus the two-dimensional Poisson equation for wall-normal velocity can be recast as a Poisson equation for the streamfunction:

$$\Delta \phi = \omega \tag{2.35}$$

Introducing the wavelike solution assumption, as in equation (2.32) but without the dependence on the spanwise dimension y, leaves us with the following paired eigenproblems.

$$-i\gamma\tilde{\omega} + i\alpha U_B\tilde{\omega} - i\alpha U_B''\tilde{\phi} = \frac{(D^2 - \alpha^2)\tilde{\omega}}{Re}$$
 (2.36)

$$(D^2 - \alpha^2)\tilde{\phi} = \tilde{\omega} \tag{2.37}$$

Thomas' method finitely expands the variables $\tilde{\omega}$ and $\tilde{\phi}$ in terms of odd Chebyshev polynomials, such that for a variable f we have:

$$f(x, z, t) = \sum_{k=1}^{N} f_k(x, t) T_{2k-1}(\eta)$$
 (2.38)

This means that if we integrate the equations (2.36) and (2.37) twice with respect to our transformed wall-normal variable η , we obtain the equations:

$$-i\gamma \mathbf{I}\underline{\tilde{\omega}} + i\alpha \mathbf{I}U_{B}\underline{\tilde{\omega}} - i\alpha \mathbf{I}U_{B}''\underline{\tilde{\phi}} = \frac{(\mathbf{K} - \alpha^{2}\mathbf{I})\underline{\tilde{\omega}}}{Re}$$
(2.39)

$$(\mathbf{K} - \alpha^2 \mathbf{I})\tilde{\phi} = \mathbf{I}\underline{\tilde{\omega}}, \tag{2.40}$$

where I and K denote tridiagonal and pentadiagonal matrices acting on the vectors $\underline{\tilde{\omega}}$ and $\underline{\tilde{\phi}}$ respectively. $\underline{\tilde{\omega}}$ and $\underline{\tilde{\phi}}$ are vectors containing the Chebyshev coefficients of $\underline{\tilde{\omega}}$ and $\underline{\tilde{\phi}}$. Coupled with discrete representations of the boundary conditions on $\underline{\tilde{\phi}}$ and the integral condition on $\underline{\tilde{\omega}}$, we can define a matrix equation of the form:

$$(B_0 + \alpha B_1 + \alpha^2 B_2)(\underline{\tilde{\omega}}, \tilde{\phi})^T = \underline{0}$$
(2.41)

We can reduce the order of α in this equation by making the substitutions:

$$\underline{x} = (\underline{\tilde{\omega}}, \underline{\tilde{\phi}})^T, \quad \underline{x}_1 = \alpha \underline{x}$$
 (2.42)

Thus we get a matrix equation which is first order in α :

$$\left(\begin{bmatrix} -B_1 & -B_0 \\ I & 0 \end{bmatrix} - \alpha \begin{bmatrix} B_2 & 0 \\ 0 & I \end{bmatrix} \right) \begin{bmatrix} \underline{x_1} \\ \underline{x} \end{bmatrix} = \underline{0}$$
(2.43)

Here, 0 and I are appropriately sized zero and identity matrices. This is a generalised eigenvalue problem for α . Given a suitable initial guess, a cubically convergent method can be used to determine the most unstable eigenvalue and thus the anticipated complex wavenumber of the Tollmien-Schlichting waves for the flow configuration specified by U_B and Re and the perturbation specified by γ .

2.4 Prescribing the basic state

2.4.1 The Blasius boundary layer

As mentioned above, and represented mathematically in equations (2.6), the topic of interest is the stability of established boundary layer solutions to small perturbations. Our principal test for validation of the model is its ability to accurately capture Tollmien-Schlichting waves, as discussed in section 2.3. In order to model this, the classical mechanism of transition from laminar to turbulent flow, we used as a basis the Blasius boundary layer, a suitable solution for a boundary layer on a semi-infinite flat plate aligned with the free-stream flow. Since a semi-infinite plate has no natural length scale, it is reasonable to assume that the boundary layer profile has no scale in the x and z directions, but rather can be characterised by a single dimension ξ , obtained by a suitable combination of x and z [57]. We take the boundary layer equations for the case where there is no external pressure gradient:

$$\frac{\partial U_x}{\partial x} + \frac{\partial U_z}{\partial z} = 0 \tag{2.44}$$

$$U_{x}\frac{\partial U_{x}}{\partial x} + U_{z}\frac{\partial U_{x}}{\partial z} = \nu \frac{\partial^{2} U_{x}}{\partial z^{2}}$$
(2.45)

We define our similarity variable ξ as:

$$\xi = z\sqrt{\frac{U_{\infty}}{\nu x}} \tag{2.46}$$

And then recast our equations in terms of a nondimensalised streamfunction. Introducing a streamfunction means that the continuity condition is automatically satisfied. We denote the nondimensional streamfunction as $f(\xi)$. Introducing these dimensionless variables into the zero pressure gradient flat plate boundary layer equations, a nonlinear ordinary differential equation is found:

$$f''' + \frac{1}{2}ff'' = 0 (2.47)$$

Suitable boundary conditions on f can be found by considering the no-slip condition at the wall and the fact that U_x must tend to U_∞ in the limit $\xi \to \infty$. There exist many standard techniques appropriate for the solution of the Blasius boundary layer equation. For the research presented here, the solutions were found using code furnished by Thomas [75].

2.4.2 The turbulent boundary layer

In addition to Tollmien-Schlichting waves, we are also interested in the behaviour of perturbations in a streaky turbulent boundary layer. Thus, we need to generate a suitable turbulent mean profile. There are many well-known results that can be used for this purpose; Prandtl, for instance, showed that the mean turbulent profile behaved linearly in the viscous sublayer very close to the wall as long ago as 1910 [59]; for further details of some of these results, see section 1.1. However, most of these results have only a limited wall-normal range in which they are applicable, as is reflected in the conventional division of the mean turbulent profile into the innermost viscous sublayer, the outer log-law layer (where viscous effects are negligible) and the intermediate buffer region. Spalding [72] formulated a new "law of the wall", valid throughout the turbulent boundary layer, by reversing the usual formulation of velocity profiles and specifying z^+ in terms of U^+ . (Note that the superscript + symbol is used to indicate wall units, which are discussed in the introductory chapter and whose implementation here is explained below.)

$$z^{+} = U^{+} + e^{-\kappa B} \left[e^{\kappa U^{+}} - 1 - \kappa U^{+} - \frac{(\kappa U^{+})^{2}}{2!} - \frac{(\kappa U^{+})^{3}}{3!} - \frac{(\kappa U^{+})^{4}}{4!} \right], \tag{2.48}$$

 κ and B constants that have been determined empirically ($\kappa = 0.41, B = 5.5$). κ is called von Kármán's constant.

Recall that we need not only the velocity profile, but also the profile of the first and second wall-normal derivatives of velocity. These can also be obtained from Spalding's law-of-the-wall, by first differentiating to obtain:

$$\frac{dz^{+}}{dU^{+}} = 1 + \kappa e^{-\kappa B} \left[e^{\kappa U^{+}} - 1 - \kappa U^{+} - \frac{(\kappa U^{+})^{2}}{2!} - \frac{(\kappa U^{+})^{3}}{3!} \right]
\frac{d^{2}z^{+}}{dU^{+2}} = \kappa^{2}e^{-\kappa B} \left[e^{\kappa U^{+}} - 1 - \kappa U^{+} - \frac{(\kappa U^{+})^{2}}{2!} \right],$$
(2.49)

and then applying the following identities to calculate the required derivatives:

$$\frac{dU^{+}}{dz^{+}} = \frac{1}{dz^{+}/dU^{+}}$$

$$\frac{d^{2}U^{+}}{dz^{+2}} = \frac{-d^{2}z^{+}/dU^{+2}}{(dz^{+}/dU^{+})^{3}}$$
(2.50)

Note that Spalding's law of the wall gives the velocity profile implicitly; thus we cannot simply calculate the values of the profile at the wall-normal nodes of the discretisation. Instead, we calculate z^+ , dU^+/dz^+ and d^2U^+/dz^{+2} for many different values of U^+ ; typically, 100K different values, where K is the number of nodes in the wall-normal discretisation. Splines for the velocity and velocity derivatives are then constructed on the spatial points that have been obtained from Spalding's law, and these splines are evaluated at the nodes in order to obtain the profiles.

In the outer part of the turbulent boundary layer, there is a gap between the experimentally observed velocity profile and the log-law profile, such that the log-law under-predicts the true velocity. Coles [18] observed that this gap was of a wake-like form. Thus, a more accurate velocity profile can be obtained from the following expression:

$$U^{+}(z^{+}) = U_{S}^{+}(z^{+}) + \frac{2\Pi}{\kappa} f\left(\frac{z^{+}}{\delta^{+}}\right)$$
 (2.51)

Here U_S^+ is the profile that we have obtained from Spalding's formulation of the law-of-the-wall (which matches the log-law profile in the outer part of the boundary layer). Π is the Coles wake parameter, which expresses the magnitude of the deviation of the velocity profile from the law-of-the-wall (for flat plate boundary layers, we have $\Pi=0.45$). $f(z^+/\delta^+)$ is an S-shaped function which is 0 at the wall $(z^+=0)$ and 1 at the boundary layer edge $(z^+=\delta^+)$. There are many forms that f has been assumed to take; in generating our turbulent profile, we use:

$$f\left(\frac{z^{+}}{\delta^{+}}\right) = 3\left(\frac{z^{+}}{\delta^{+}}\right)^{2} - 2\left(\frac{z^{+}}{\delta^{+}}\right)^{3} \tag{2.52}$$

The Coles terms are a simple additive correction to the calculated profile, and they are defined explicitly. Therefore, they are included in a straightforward fashion, by addition to the profile obtained from the evaluation of the Spalding spline at the nodes of the spatial discretisation. The derivatives of the Coles terms are also, of course, added to the velocity derivative profiles.

As mentioned earlier, the turbulent boundary layer profile is calculated in wall units; in order to make it usable, we must convert from wall variables to the dimensionless variables used in the numerical formulation. The numerical formulation in the solver does not use dimensional outer variables, but rather variables that have been non-dimensionalised using the velocity and length scales used to define the Reynolds number, as per equation 2.2. The velocity scale has previously been specified as the freestream velocity, but the length scale has heretofore been left arbitrary. For the sake of convenience, we here take the non-dimensionalising length as the boundary layer displacement thickness δ^* , as defined in equation (2.55). Thus, if we take a bar as denoting the dimensionless solver variables, we can say that:

$$z^{+} = \bar{z}\delta^{*+}; U^{+} = \bar{U}U_{\infty}^{+} \tag{2.53}$$

We can then convert the profiles that we have calculated in wall variables into the solver

variables as follows:

$$\bar{U} = \frac{U^{+}}{U_{\infty}^{+}}$$

$$\frac{d\bar{U}}{d\bar{z}} = \frac{\delta^{*+}}{U_{\infty}^{+}} \frac{dU^{+}}{dz^{+}}$$

$$\frac{d^{2}\bar{U}}{d\bar{z}^{2}} = \frac{\delta^{*+2}}{U_{\infty}^{+}} \frac{d^{2}U^{+}}{dz^{+2}}$$
(2.54)

How are we to obtain the length and velocity scales δ^{*+} and U_{∞}^{+} that will allow us to convert between the wall and outer variables? δ^{*+} is the displacement thickness in wall units; the displacement thickness in outer units is defined as:

$$\delta^* = \int_0^\infty \left(1 - \frac{U}{U_\infty} \right) dz \tag{2.55}$$

If we suppose that there is a nominal boundary layer thickness δ beyond which $U(z) = U_{\infty}$, this can be rewritten as:

$$\delta^* = \int_0^\delta \left(1 - \frac{U}{U_\infty} \right) dz \tag{2.56}$$

The length and velocity scales used to convert from outer units to wall units are ν/u_{τ} and u_{τ} respectively, where u_{τ} is the friction velocity. Thus:

$$z^+ = \frac{zu_\tau}{\nu} \tag{2.57}$$

and:

$$\delta^* = \frac{\nu}{u_{\tau}} \int_0^{\delta^+} \left(1 - \frac{U}{U_{\infty}} \right) dz^+$$

$$= \frac{\nu}{u_{\tau}} \left[\delta^+ - \frac{1}{U_{\infty}^+} \int_0^{\delta^+} U^+ dz^+ \right]$$
(2.58)

Now, if we represent U^+ as:

$$U^{+}(z^{+}) = \frac{\ln z^{+}}{\kappa} + B + \frac{2\Pi}{\kappa} \left[3 \left(\frac{z^{+}}{\delta^{+}} \right)^{2} - 2 \left(\frac{z^{+}}{\delta^{+}} \right)^{3} \right]; \tag{2.59}$$

that is to say, as the log-law profile plus the Coles wake correction, we can perform the integration in equation 2.58 analytically. This gives us:

$$\int_{0}^{\delta^{+}} U^{+} dz^{+} = \int_{0}^{\delta^{+}} \left(\frac{\ln z^{+}}{\kappa} + B + \frac{2\Pi}{\kappa} \left[3 \left(\frac{z^{+}}{\delta^{+}} \right)^{2} - 2 \left(\frac{z^{+}}{\delta^{+}} \right)^{3} \right] \right) dz^{+}$$

$$= \delta^{+} \left[\frac{\ln \delta^{+} - 1}{\kappa} + B + \frac{\Pi}{\kappa} \right]$$
(2.60)

Thus:

$$\delta^* = \frac{\nu \delta^+}{u_\tau} \left[1 - \frac{1}{U_\infty^+} \left(\frac{\ln \delta^+ - 1}{\kappa} + B + \frac{\Pi}{\kappa} \right) \right]$$

$$= \frac{\delta}{U_\infty^+} \left[U_\infty^+ - \frac{\ln \delta^+ - 1}{\kappa} - B - \frac{\Pi}{\kappa} \right]$$
(2.61)

Now, recalling how we represented U^+ in equation 2.59, we can obtain an expression for U_{∞}^+ by setting $z^+ = \delta^+$, then substitute this into equation 2.61 and finally obtain:

$$\delta^* = \frac{1+\Pi}{\kappa U_{\infty}^+} \delta \tag{2.62}$$

Then, since the boundary layer displacement thickness is the length scale for dimensionless solver variables, we can say that the boundary layer thickness itself (in dimensionless solver variables) is given by:

$$\bar{\delta} = \frac{\kappa U_{\infty}^+}{1 + \Pi} \tag{2.63}$$

And thus:

$$\delta^{+} = \frac{\kappa U_{\infty}^{+}}{1 + \Pi} \delta^{*+}$$

$$= \frac{\kappa Re}{1 + \Pi}$$
(2.64)

We can then substitute our δ^+ value into equation (2.59) to calculate U_{∞}^+ . Finally, we note that:

$$Re = \frac{U_{\infty} \delta^*}{\nu}$$

$$= \frac{U_{\infty}}{u_{\tau}} \frac{\delta^* u_{\tau}}{\nu}$$

$$= U_{\infty}^+ \delta^{*+}$$
(2.65)

Thus, having found a value for U_{∞}^+ , we can calculate the corresponding δ^{*+} . Since we know U_{∞}^+ , we know the range of values of U^+ we need to solve the Spalding law-of-the-wall for in order to construct our splines. Since we know δ^{*+} , we are able to determine what values of z^+ we need to evaluate the splines at in order to obtain the nodal values of the velocity and velocity derivative profiles, and we have constructed a satisfactory mean turbulent boundary layer profile.

It is interesting to note that, in this formulation, the value of δ^+ is identical to the friction Reynolds number, Re_{τ} . In the $Re=10^4$ case, which is investigated extensively in later chapters, this yields $Re_{\tau}\approx 2800$.

2.5 Spanwise forcing

We hope to investigate the effects of spanwise forcing on the development of boundary layer perturbations; in other words, we want to be able to specify a non-zero u_y at the wall. u_y is a secondary variable in our formulation; the only place that the value of u_y at the wall appears in our formulation is as \hat{u}_y in our integral condition on ω_x , equation 2.30. This means it is very straightforward to include wall forcing in our formulation.

In order to confirm that the spanwise forcing has been been incorporated correctly, we seek some appropriate analytic solution against which we can compare our numerical results. By making some simplifying assumptions, such analytic solutions can be found. Firstly, we assume that there is no streamwise dependence, so all streamwise derivatives are identically zero. Secondly, since the governing equations are linear, we can assume

that all solution variables vary only in the same spanwise and temporal modes as the spanwise excitation itself. In other words, we assume that all variables take the following form:

$$f(y,z,t) = f^*(z)e^{i(\beta y - \gamma t)}$$
(2.66)

For the sake of ease, and without loss of generality, we set $\beta > 0$. Having made these simplifications, it is now possible to immediately solve the streamwise vorticity transport equation, which simplifies to:

$$\frac{d^2\omega_x^*}{dz^2} - (\beta^2 - i\gamma Re)\omega_x^* = 0$$
(2.67)

If we then define:

$$\nu^2 = \beta^2 - i\gamma Re,\tag{2.68}$$

We can write down an analytic solution.

$$\omega_x^* = Ae^{-\nu z} \tag{2.69}$$

A an arbitrary constant. A term in $e^{\nu z}$ also appears, but if we assume that $Re(\nu) > 0$, we can immediately discard this term, since we have a zero boundary condition on all variables infinitely far away from the wall. Then, using the simplified continuity equation and the definition of streamwise vorticity, we can derive two ordinary differential equations relating the components of velocity u_y^* and u_z^* to ω_x^* :

$$\left(\frac{d^2}{dz^2} - \beta^2\right) u_y^* = -\frac{d\omega_x^*}{dz}
\left(\frac{d^2}{dz^2} - \beta^2\right) u_z^* = i\beta\omega_x^*$$
(2.70)

The homogeneous parts of both solutions are identical to within an arbitrary multiplicative constant once we take into account the zero boundary condition infinitely far away from the wall. To obtain the inhomogeneous part of the solution, we substitute in our solution

for ω_x^* and follow the usual procedure for the solution of an ordinary differential equation. By imposing the boundary condition at the wall $\hat{u}_y(y,t) = \hat{u}_y^* e^{i(\beta y - \gamma t)}$ (\hat{u}_y^* the amplitude of the spanwise oscillation), we can eliminate the arbitrary constants that arise as part of the homogenous solution, leaving A as the only arbitrary constant in the solutions. The solutions that we obtain for the two components of velocity by this procedure are as follows:

$$u_{y}^{*} = \frac{\nu A}{\nu^{2} - \beta^{2}} (e^{-\nu z} - e^{-\beta z}) + \hat{u}_{y}^{*} e^{-\beta z}$$

$$u_{z}^{*} = \frac{i\beta A}{\nu^{2} - \beta^{2}} (e^{-\nu z} - e^{-\beta z})$$
(2.71)

In order to eliminate the arbitrary constant A, we plug these two solutions for u_y^* and u_z^* into the definition of ω_x^* , which yields:

$$\omega_x^* = Ae^{-\nu z} + \beta \left(\hat{u}_y^* + \frac{(\beta - \nu)A}{\nu^2 - \beta^2} \right) e^{-\beta z}$$
 (2.72)

We need the term in $e^{-\beta z}$ to vanish in order to maintain consistency between the solutions for ω_x^* given in equations 2.69 and 2.72. Thus, we are able to determine $A = \hat{u}_y^*(\beta + \nu)$, and we have the analytic solutions against which to compare our numerical results for spanwise forcing:

$$u_{y}^{*} = \frac{\nu \hat{u}_{y}^{*}}{\nu - \beta} (e^{-\nu z} - e^{-\beta z}) + \hat{u}_{y}^{*} e^{-\beta z}$$

$$u_{z}^{*} = \frac{i\beta \hat{u}_{y}^{*}}{\nu - \beta} (e^{-\nu z} - e^{-\beta z})$$

$$\omega_{x}^{*} = \hat{u}_{y}^{*} (\beta + \nu) e^{-\nu z}$$
(2.73)

In the limit $\beta \to 0$ i.e., as we approach the case where there is spanwise uniformity, these solutions are identical to the standard Stokes oscillatory solutions. Note that these solutions are independent of the basis flow. It would also be useful to have an analytic solution for ω_y^* . However, if we examine the modified spanwise vorticity transport equation:

$$\frac{d^2\omega_y^*}{dz^2} - (\beta^2 - i\gamma Re)\omega_y^* = Re(U_B''u_z^* - i\beta U_B'u_y^*), \tag{2.74}$$

we see that ω_y^* is not independent of the basis flow. Since we do not have a closed-form analytic expression for the basis flow, but rather only a numerical one (see sections 2.4.1 and 2.4.2), we cannot obtain an analytic ω_y^* against which to compare our numerical results.

Chapter 3

Numerical methods

In this chapter, the various numerical techniques used to solve the governing equations are described. Some general points such as the discretisation of the domain and the transformation of the wall are discussed first. Following this, the details of the solvers for the vorticity transport equations and the Poisson equation are given. Lastly, there is a description of the complete algorithms for the solver.

3.1 General features

3.1.1 Domain discretisation

In the streamwise direction, we choose a uniform discretisation of J+1 nodes such that the 0th node lies on the inlet and the Jth node lies on the outlet. This uniform streamwise discretisation, as we will see later, is crucial for the implementation of a direct solver for the Poisson equation.

The discretisation of the wall-normal dimension is also uniform, albeit uniform in the transformed variable η , which is defined in equation 2.24. From the point of view of domain discretisation, l can be thought of as a parameter that controls the clustering of node points in the wall-normal direction. Any discretisation of the transformed wall

normal coordinate will give us a set of wall-normal stations, one for each node point, which we can label $\{\eta_0, \eta_1, \dots \eta_K\}$. Each of these stations in the transformed coordinate corresponds to a station in the untransformed coordinate, giving us a related set of wall-normal stations $\{z_0, z_1, \dots z_K\}$. A uniform discretisation of the η -coordinate would give a set of evenly-spaced node points such that $\Delta \eta = \eta_k - \eta_{k-1}$ is the same for every k.

Intuitively, we see that wall-normal stations of these node points in the untransformed coordinate will be clustered near the wall; indeed, we can show that the separation between wall-normal stations tends towards infinity as we move away from the wall. Let us consider two adjacent stations in the wall-normal discretisation, located at z_k and z_{k-1} in the untransformed coordinate or η_k and η_{k-1} in the transformed. $\eta_k - \eta_{k-1} = \Delta \eta$, per our uniform discretisation in the transformed variable; let us denote by Δz_k the corresponding separation in the untransformed variable, i.e., $\Delta z_k = z_k - z_{k-1}$. By equation 2.24, we can say that:

$$\Delta \eta = \frac{l}{l+z_k} - \frac{l}{l+z_{k-1}},\tag{3.1}$$

and therefore, by rearranging suitably, we can show that:

$$\Delta z_k = \frac{-\Delta \eta (l + z_k)(l + z_{k-1})}{l} \tag{3.2}$$

Thus we see that the separation in the untransformed domain indeed tends to infinity as we move infinitely far from the wall. The sign of Δz_k is negative because the numbering of the nodes is chosen for convenience when dealing with η , one of the consequences of which being that z_k is in fact closer to the wall than z_{k-1} . The parameter l controls the tightness of the node clustering near the wall: as l gets smaller, the node points in z are clustered closer to the wall.

3.1.2 Compact finite differences

The idea of compact finite differences is a development of the more familiar concept of finite differences. A finite difference is a discretised approximation for a derivative. For instance, the most common central finite difference approximation to the first derivative takes the form:

$$f'(x_k) = \frac{f(x_{k+1}) - f(x_{k-1})}{2h} + O(h^2), \tag{3.3}$$

where the subscripts count nodes in a uniform domain discretisation, with h being the separation of two adjacent nodes. It is relatively easy to confirm that, if we take a Taylor series expansion of the terms on the right-hand side of the equation above, we will get the above expression to within an error term of order h^2 . We see that this finite difference formulation gives us the approximate value of the derivative explicitly; we simply plug the known nodal values in and get out our approximation.

The corresponding compact finite difference formulation yields a higher-order approximation to the derivatives without the need for a larger difference stencil i.e., involving values from the same nodes:

$$\frac{1}{4}f'(x_{k-1}) + f'(x_k) + \frac{1}{4}f'(x_{k+1}) = \frac{3(f(x_{k+1}) - f(x_{k-1}))}{4h} + O(h^4)$$
 (3.4)

The price we pay for this is that the formulation becomes implicit, and we need to solve a system of equations to obtain the derivatives. This is obviously of little use if we only need to know the derivative at a particular point, but here, where we require the value of the derivative across the entire solution domain, it becomes more useful. The fourth-order centred schemes set out in Lele's paper [47] were used to calculate the first and second streamwise derivatives where required e.g. in the explicit terms of the vorticity transport equation. Lele's paper also discusses the advantages of central difference schemes in terms of preserving phase in wavelike solutions.

Compact finite differences were also implemented for the wall-normal derivatives; this is discussed in more detail in section 3.2.2.

3.2 Vorticity transport equation solver

3.2.1 Time stepping scheme

The main task of solving the vorticity transport equation numerically is that of creating a semi-implicit time-stepping scheme. Some different methods were attempted, including, for instance, a Runge-Kutta scheme, but the only method described here is the one that was used to produce the results presented later in the thesis.

We chose an iterative approach, where at each step some terms are treated implicitly and some explicitly. By using explicit in this context, we mean only that the terms are taken from the previous iteration; the overall scheme is still implicit. The first task was to decide which terms are to be treated implicitly. This decision is made on the basis of both physical and computational grounds. Firstly, what terms represent the most important physical mechanisms of vorticity transport? Secondly, how difficult will it be, computationally, to invert the system of equations that result from treating some terms implicitly?

The first consideration is relatively straightforward; for a boundary layer flow, the most important transport mechanism for vorticity is wall-normal diffusion. It is the terms representing this in the equations 2.14 and 2.15 that we will want to treat implicitly. In the three dimensional case, since we use spectral methods for the spanwise dimension, it becomes trivially easy to also treat spanwise diffusion implicitly.

As mentioned above, the time stepping scheme used was iterative. For the first step, the explicit terms are calculated using values from previous times, and we obtain a first approximation to the solution variables at the new time. This first approximation is then used to update the explicit terms, and we iterate this procedure until convergence, updating the explicit terms with each solution. This update includes solving the Poisson equation to update u_z using the new solution for vorticity. In practice, it was found that apart from the first few time levels, the solution would converge after only a single iteration.

Using a second-order backward difference for the time derivative, and denoting the implicit terms as I and the explicit terms as E, we obtain the following equations to be solved numerically (ω stands in for whichever component of vorticity is being solved for):

$$\frac{3\omega^{n,0}}{2\Delta t} - I^{n,0} = \frac{4\omega^{n-1} - \omega^{n-2}}{2\Delta t} + 2E^{n-1} - E^{n-2} + O(\Delta t^2)$$

$$\frac{3\omega^{n,i}}{2\Delta t} - I^{n,i} = \frac{4\omega^{n-1} - \omega^{n-2}}{2\Delta t} + E^{n,i-1} + O(\Delta t^2)$$
(3.5)

$$\frac{3\omega^{n,i}}{2\Delta t} - I^{n,i} = \frac{4\omega^{n-1} - \omega^{n-2}}{2\Delta t} + E^{n,i-1} + O(\Delta t^2)$$
(3.6)

The superscripts n and i label the time level and number of iterations at the current time level respectively. Equation 3.5 gives a simplified discretisation for the first step, the solution of which we treat as the 0th iteration for the iterative corrector step (hence the second superscript 0). The equations for both case are discretised about the time level n, which is the current time level i.e. the time level for which we are attempting to obtain a solution. The term $2E^{n-1} - E^{n-2}$ on the right-hand side of equation 3.5 serves as an Adams-Bashforth projection of the explicit terms to time level n. Equation 3.6 show a simplified version of the discretisated equation which we solve iteratively until convergence, defined by $\varepsilon < \varepsilon_c$, where ε is defined by:

$$\varepsilon = \frac{\sum \sqrt{(\omega^{n,i-1})^2 - (\omega^{n,i})^2}}{\sum |\omega^{n,i-1}|}$$
(3.7)

And ε_c is a sufficiently small tolerance. The summations in the definition of ε are over all the nodes in the spatial discretisation.

3.2.2 Spatial discretisation

Let us consider the semi-discretised formulation of a generalised VTE, after the transformation of the wall-normal coordinate.

$$\frac{3\omega^n}{2\Delta t} - \frac{1}{Re} \left(\frac{\eta^4}{l^2} \frac{\partial^2 \omega}{\partial \eta^2} + \frac{2\eta^3}{l^2} \frac{\partial \omega}{\partial \eta} \right) = \frac{4\omega^{n-1} - \omega^{n-2}}{2\Delta t} + E + O(\Delta t^2), \tag{3.8}$$

with E standing in for the explicit terms. An early version of the VTE solver had used centred finite differences for the wall-normal derivatives $(\partial \omega/\partial \eta)$ and $\partial^2 \omega/\partial \eta^2$ to give a tridiagonal system of equations for the implicit terms. This scheme was second-order accurate. However, using compact finite differences, it is possible to concoct a scheme which is fourth-order accurate but still tridiagonal, meaning that a higher order of accuracy can be obtained for no additional computational effort. To see how this is set up, let us first introduce the following notation:

$$\lambda(\omega) = \frac{\eta^4}{l^2} \frac{\partial^2 \omega}{\partial n^2} + \frac{2\eta^3}{l^2} \frac{\partial \omega}{\partial n}$$
 (3.9)

By matching coefficients in Taylor expansions about the kth wall-normal node, we can derive the following tridiagonal relation between nodal values of $\lambda(\omega)$ and ω :

$$\frac{k^3}{10(k-1)^3} \lambda_{k-1} + \lambda_k + \frac{k^3}{10(k-1)^3} \lambda_{k+1}
= \frac{6\Delta \eta^2 k^3}{5l^2} ((k-1)\omega_{k-1} - k\omega_k + (k+1)\omega_{k+1}) + O(\Delta \eta^4) \quad (3.10)$$

Note that we use ω_k to mean ω evaluated at the kth wall-normal node and λ_k to mean $\lambda(\omega)$ evaluated at the same location. The appearance of $\Delta\eta^2$ on the numerator of the right-hand side, rather than the denominator, is due to the appearance of powers of η in the wall-normal derivatives after performing the transformation. Using this relationship, the equation (3.8) can be recast as a relationship between the values of vorticity at three adjacent nodes and the values of the terms on the right-hand side of equation (3.8) at the same three adjacent nodes:

$$\frac{3}{2\Delta t} \left(\omega_k^n + \frac{k^3}{10} \left(\frac{\omega_{k-1}^n}{(k-1)^3} + \frac{\omega_{k+1}^n}{(k+1)^3} \right) \right) - \frac{6\Delta \eta^2 k^3}{5l^2 Re} \left[(k-1)\omega_{k-1} - 2k\omega_k + (k+1)\omega_{k+1} \right] \\
\approx \frac{4\omega_k^{n-1} - \omega_k^{n-2}}{2\Delta t} + E_k + \frac{k^3}{10(k-1)^3} \left(\frac{4\omega_{k-1}^{n-1} - \omega_{k-1}^{n-2}}{2\Delta t} + E_{k-1} \right) + \\
+ \frac{k^3}{10(k+1)^3} \left(\frac{4\omega_{k+1}^{n-1} - \omega_{k+1}^{n-2}}{2\Delta t} + E_{k+1} \right) \quad (3.11)$$

In this and subsequent equations describing the discretisation scheme, we use \approx to indicate that the equalities are not exact but instead second-order accurate in time and fourth-order accurate in space. As mentioned above, this yields a tridiagonal system in the same way as the more conventional centred finite difference approach, and thus, in conjunction with a numerical representation of the integral condition on vorticity, can be solved using a modification of the Thomas algorithm (for which see 3.2.4).

3.2.3 Calculation of the explicit terms

All the spatial derivative terms in the vorticity transport equations that are not to be treated implicitly are included in the explicit terms E in equations (3.5) & (3.6). In this section, we briefly discuss the treatment of the explicit terms. In the two dimensional case, the explicit term is given by the following expression:

$$E = \frac{1}{Re} \frac{\partial^2 \omega_y}{\partial x^2} - U \frac{\partial \omega_y}{\partial x} - U'' u_z$$
 (3.12)

In the linear three dimensional case, the explicit terms for the streamwise and spanwise vorticity transport equations are given, respectively, by the following equations:

$$E_x = \frac{1}{Re} \frac{\partial^2 \omega_x}{\partial x^2} - U \frac{\partial \omega_x}{\partial x} + U' \frac{\partial u_y}{\partial x}$$
 (3.13)

$$E_{y} = \frac{1}{Re} \frac{\partial^{2} \omega_{y}}{\partial x^{2}} - U \frac{\partial \omega_{y}}{\partial x} + U' \frac{\partial u_{y}}{\partial y} - U'' u_{z}$$
 (3.14)

For the nonlinear version of the governing equations, as discussed in section 2.1.2, the explicit terms are subject to some manipulation to obtain the most convenient form.

Principally this is to do with reducing the number of different secondary variables that appear.

$$E_{x;nl} = \frac{1}{Re} \frac{\partial^2 \omega_x}{\partial x^2} - (U + u_x) \frac{\partial \omega_x}{\partial x} - u_z \frac{\partial \omega_z}{\partial z} - \omega_x \frac{\partial u_z}{\partial z} + \left(U' + \omega_y + \frac{\partial u_z}{\partial x} \right) \omega_z (3.15)$$

$$E_{y;nl} = \frac{1}{Re} \frac{\partial^2 \omega_y}{\partial x^2} - (U + u_x) \frac{\partial \omega_y}{\partial x} - u_z \left(U'' + \frac{\partial \omega_y}{\partial z} \right)$$
(3.16)

The explicit terms for the secondary perturbation formulation of the governing equations (see section 2.1.3) are manipulated in a similar way. The expressions obtained are given below.

$$E_{2x} = \frac{1}{Re} \frac{\partial^2 \omega_{2x}}{\partial x^2} - U_{Sx} \frac{\partial \omega_{2x}}{\partial x} - i\beta U_{Sy} \omega_{2x} - U_{Sz} \frac{\partial \omega_{2x}}{\partial z} - u_{2z} \frac{\partial \Omega_{Sx}}{\partial z} - \Omega_{Sx} \frac{\partial u_{2z}}{\partial z} + (3.17)$$

$$\Omega_{Sz} \left(\omega_{2y} + \frac{\partial u_{2z}}{\partial x} \right) + \omega_{2x} \frac{\partial U_{2x}}{\partial x} + \left(i\beta \Omega_{Sy} - \frac{\partial \Omega_{Sx}}{\partial x} \right) u_{2x} - i\beta \Omega_{Sx} u_{2y} + \frac{\partial U_{Sx}}{\partial z} \omega_{2z}$$

$$E_{2y} = \frac{1}{Re} \frac{\partial^2 \omega_{2y}}{\partial x^2} - U_{Sx} \frac{\partial \omega_{2y}}{\partial x} - i\beta U_{Sy} \omega_{2y} - U_{Sz} \frac{\partial \omega_{2y}}{\partial z} - u_{2z} \frac{\partial \Omega_{Sy}}{\partial z} + \omega_{2x} \frac{\partial U_{Sy}}{\partial x} + \Omega_{2x} \frac{\partial U_{Sy}}{\partial x} + \Omega_{2x} \frac{\partial \Omega_{Sy}}{\partial x} + \Omega_{2x} \frac$$

The streamwise derivatives of any component of ω , whenever it appears in the explicit terms, are calculated using a compact finite difference scheme, as described in the paper by Lele [47]. Note that on the outflow boundary we apply the boundary condition $\partial^2 \omega / \partial x^2 = -\alpha^2 \omega$ for the second streamwise derivatives, which is consistent with a sinusoidal variation with wavenumber α in the x-direction. For the validation of the solvers ability to capture Tollmien-Schlichting waves (see section 4.2), we set α to be the expected wavenumber. For calculating streaks, as discussed in chapter 5, we set $\alpha = 0$; that is to say, we set the second streamwise derivatives to zero on the outlet.

3.2.4 Numerical integration

Secondary variables

Of the expressions that appear in the explicit terms, the only ones that require some sort of special treatment are those involving secondary variables (see equations 2.12 and associated discussion). Recall that these are defined as integrals of the primary variables. We must therefore find some suitable way of calculating integrally defined terms. Having incorporated compact finite differences into the spatial discretisation of the governing equations, it is sensible to see if there is a way to implement them in the integration of the secondary variables. Thus, we now look at the use compact finite differences to obtain the unknown nodal values of a variable (say f) from the known nodal values of its first wall-normal derivative, rather than vice-versa.

Naively, the natural scheme to use is the standard centred compact finite differences as described in Lele's paper [47], but it can immediately be seen that this presents a problem when working from the nodal derivatives to the nodal values of the variable itself. The fourth order classical Pade scheme, which is used elsewhere in the program to calculate first derivatives, is of the following form for some arbitrary variable f defined on a uniform discretisation of η :

$$\frac{3}{4\Delta\eta}(f_{k+1} - f_{k-1}) = f'_k + \frac{1}{4}(f'_{k-1} + f'_{k+1}) + O(\Delta\eta^4)$$
(3.19)

But we see that this formulation decouples the odd nodes from the even nodes, and since we are trying to calculate the variables from their derivatives, it is therefore unworkable. This fourth-order-accurate relationship between nodal values at three adjacent nodes is unique, and so there is no work-around that will preserve the same structure of the resulting system of difference equations. We must consider another way of dealing with the problem. Let us consider a scheme that is centred about an imaginary node located between nodes k and k+1:

$$f_k - f_{k+1} = af'_{k-1} + bf'_k + cf'_{k+1} + df'_{k+2} + O(\Delta \eta^4)$$
(3.20)

Note that equation 3.20 contains only four free coefficients (a, b, c, d), rather than the five that might be expected for a fourth-order compact finite difference scheme. This is because it can be immediately seen that the terms in f on the left-hand side must balance, since only terms in f' and higher derivatives appear on the right-hand side. Therefore we can immediately specify the relationship between these two terms, eliminating one of the coefficients. The remaining coefficients can be determined in the usual manner. After some rearrangement, we obtain:

$$\frac{f_k - f_{k+1}}{\Delta \eta} = \frac{1}{24} (f'_{k-1} - 13f'_k - 13f'_{k+1} + f'_{k+2}) + O(\Delta \eta^4)$$
 (3.21)

By a similar process we can devise non-centred compact difference equations of a comparable type for the boundary nodes:

$$\frac{f_0 - f_1}{\Delta \eta} = \frac{1}{24} (-9f_0' - 19f_1' + 5f_2' - f_3') + O(\Delta \eta^4)
\frac{f_K - f_{K-1}}{\Delta \eta} = \frac{1}{24} (9f_K' + 19f_{K-1}' - 5f_{K-2}' + f_{K-3}') + O(\Delta \eta^4)$$
(3.22)

Let us look at one instance of how this scheme is used in the solver; take, for example, the calculation of the term $\partial u_y/\partial x$ in the explicit terms of the streamwise vorticity transport equation, c.f. equations 2.14 and 3.13. Assuming that the order of differentiation can be changed, we can use the definition of the streamwise component of vorticity to obtain the following equation, taking into account the wall-normal transformation:

$$\left(\frac{\partial u_y}{\partial x}\right)' = \frac{l}{\eta^2} \left(\frac{\partial \omega_x}{\partial x} - \frac{\partial^2 u_z}{\partial x \partial y}\right) \tag{3.23}$$

Here the prime denotes differentiation with respect to the transformed wall-normal coordinate η . We have Dirichlet boundary conditions available for u_y both at the wall and infinitely far away from the wall, and it is therefore trivial to obtain Dirichlet boundary conditions for $\partial u_y/\partial x$. Thus we have a value which can be used as f_0 in equation 3.22, allowing us to calculate f_1 (that is, $\partial u_y/\partial x$ at node k=1). Then using equation 3.21,

a straightforward marching procedure can be used to calculate all the required values of $\partial u_y/\partial x$ throughout the interior of the domain. Since we have a Dirichlet condition for $\partial u_y/\partial x$ at the wall, the value of f_K from equation 3.22 is already known in this instance. If there is no such Dirichlet condition, as is the case when calculating ω_z , the second equation of 3.22 can be used to calculate f_K using f_{K-1} , the final nodal value obtained from the marching procedure.

Integral condition

This scheme can also be used to calculate the integral conditions on the components of vorticity. We will discuss a generalised version of the integral conditions on ω_x and ω_y as given in equation 2.30. We write this generalised condition as:

$$\int_0^\infty \omega dz = \int_0^\infty g dz + \text{constant}, \tag{3.24}$$

where the value of the integrand g is known at each node of the domain, and we denote its value at node k by g_k . We thus have two tasks: firstly, to calculate the integral $\int_0^\infty g dz$, and, secondly, to find a discrete representation of the constraint on ω . As we will see, solving the first problem will take us a long way towards solving the second. We begin by defining:

$$G'(\eta) = \frac{lg(\eta)}{\eta^2} \tag{3.25}$$

We use the prime to mean the same thing as in the previous section: differentiation with respect to the transformed wall-normal coordinate η . Assuming that g is such that $g/\eta^2 \to 0$ as $\eta \to 0$, we can say that:

$$G(\eta) = \int_0^{\eta} G'(\bar{\eta}) d\bar{\eta}$$

$$= \int_0^{\eta} \frac{lg(\bar{\eta})}{\eta^2} d\bar{\eta}$$

$$= \int_z^{\infty} g(\bar{z}) d\bar{z}, \qquad (3.26)$$

with $\bar{\eta}$ and \bar{z} dummy variables. Thus we see that G(1) gives us the integral condition on vorticity, once we have taken into account the additive constant that appears in equation 3.24.

Now, if we define G'_k as $G'(\eta)$ evaluated at the wall-normal node k, and G_k in a similar fashion, we can apply the scheme given by equations 3.21 and 3.22 to calculate G_K , which is equal to $\int_0^\infty g dz$. We're not interested in the values of G in the interior of the domain, so we construct the following expression:

$$G_K = (G_K - G_{K-1}) + (G_{K-1} - G_{K-2}) + \dots + (G_1 - G_0)$$
(3.27)

 G_0 is, of course, identically zero. It should be apparent that, by rearranging equations 3.21 and 3.22, we can express this as:

$$G_K = \frac{\Delta \eta}{24} (G'_K + 19G'_{K-1} - 5G'_{K-2} + G'_{K-3}) + \frac{\Delta \eta}{24} (-G'_K + 13G'_{K-1} + 13G'_{K-2} - G'_{K-3}) + \dots + \frac{\Delta \eta}{24} (G'_3 - 5G'_2 + 19G'_1 + 9G'_0)$$
 (3.28)

As mentioned above, G'_k is obtained by evaluating equation 3.25 at node k. Thus we write:

$$G_k' = \frac{lg_k}{\eta_k^2} \tag{3.29}$$

By collecting terms for each value of k, we can therefore rewrite equation 3.28 as:

$$G_K = \sum_{k=1}^K d_k g_k, (3.30)$$

where:

$$d_k = \frac{l}{k^2 \Delta \eta} \tag{3.31}$$

except for the following special cases near the boundaries of the domain.

$$d_{1} = \frac{31l}{24\Delta\eta}; \qquad d_{2} = \frac{5l}{24\Delta\eta}; \qquad d_{3} = \frac{25l}{216\Delta\eta}$$

$$d_{K} = \frac{l}{24K^{2}\Delta\eta}; \quad d_{K-1} = \frac{31l}{24(K-1)^{2}\Delta\eta}; \quad d_{K-2} = \frac{5l}{6(K-2)^{2}\Delta\eta}; \quad d_{K-3} = \frac{25l}{24(K-3)^{2}\Delta\eta}$$

$$(3.32)$$

We mentioned earlier that calculating the integral $\int_0^\infty g dz$ would help us obtain a discretisation of the integral condition on ω , and we can show now why that is. It is hopefully apparent that the coefficients d_k , which define a relationship between the nodal values of g and its integral across the domain, can just as easily be applied to ω . Thus we can write down our discrete representation of the integral condition:

$$\sum_{k=1}^{K} d_k \omega_k = G_K + \text{constant}, \tag{3.33}$$

and we have obtained a fourth-order accurate representation of the integral condition on ω_x using compact finite differences.

Now, equation 3.11 relates the values of the solution variables at any interior node k to the two adjacent nodes in the wall normal direction, and we thus rewrite it as:

$$a_k \omega_{k-1} + b_k \omega_k + c_k \omega_{k+1} = \rho_k, \tag{3.34}$$

where ρ contains all the information we already know: the explicit terms (representing convection, vortex stretching and streamwise diffusion) and the terms of the discretised time derivative from previous timesteps. We therefore have a system of K-1 equations for K unknowns. These unknowns are the values of ω at the nodes $1 \le k \le K$; the value of ω at node 0 is already known from our Dirichlet condition which specifies that all perturbation variables must go to zero infinitely far away from the wall.

Closure is achieved using a discrete representation of the integral condition on vorticity, as described above. There is one further subtlety to bear in mind, however. Since we are calculating the vorticity values at a new time step, the integral constraint must obviously apply at this timestep. However, the data used to calculate the integrand g from

equation 3.24 is taken from earlier timesteps. To resolve this problem, we use a similar procedure to the one used with the explicit terms, as expressed in equations 3.5 and 3.6. Let us introduce the notation ι to represent the entire right-hand side of equation 3.33. For the first time the VTEs are solved at a new time level n, we use an Adams-Bashforth projection from stored values of ι to approximate ι^n ; for subsequent iterations, we calculate ι afresh using data from the most recent solution at the current time level.

We have thus managed to close the system of equations. To solve this, we use a modified Thomas algorithm, as mentioned above. Let us look at the system of discretised equations that arises when solving either vorticity transport equation along a particular wall-normal line in matrix form:

$$\begin{bmatrix} d_1 & d_2 & \cdots & \cdots & d_k & \cdots & d_K \\ b_1 & c_1 & & & & & & \\ a_2 & b_2 & c_2 & & & & & \\ & \ddots & \ddots & \ddots & & & & \\ & & a_k & b_k & c_k & & & \\ & & & \ddots & \ddots & \ddots & \\ & & & a_{K-1} & b_{K-1} & c_{K-1} \end{bmatrix} \begin{bmatrix} \omega_1 \\ \omega_2 \\ \vdots \\ \omega_k \\ \vdots \\ \omega_{K} \end{bmatrix} = \begin{bmatrix} \iota \\ \rho_1 \\ \rho_2 \\ \vdots \\ \rho_k \\ \vdots \\ \rho_{K-1} \end{bmatrix}$$

$$(3.35)$$

The solution technique here is to use each equation representing a discretisation of the vorticity transport equation to eliminate a variable from the subsequent equation and from the equation representing the integral condition. We begin by defining:

$$\delta_1 = d_1$$

$$\mu_1 = b_1$$

$$\nu_1 = \rho_1$$

$$\iota_1 = \iota$$

Then, for all $2 \le k \le K - 1$, we define:

$$\mu_{k} = b_{k} - c_{k-1} \frac{a_{k}}{\mu_{k-1}}$$

$$\delta_{k} = d_{k} - c_{k-1} \frac{\delta_{k-1}}{\mu_{k-1}}$$

$$\nu_{k} = \rho_{k} - \nu_{k-1} \frac{a_{k}}{\mu_{k-1}}$$

$$\iota_{k} = \iota_{k-1} - \nu_{k-1} \frac{\delta_{k-1}}{\mu_{k-1}}$$

This leaves us with a system of two equations:

$$\delta_{K-1}\omega_{K-1} + d_K\omega_K = \iota_{K-1}$$
$$\mu_{K-1}\omega_{K-1} + c_{K-1}\omega_K = \nu_{K-1}$$

It is trivial to solve this for ω_K ; back-substitution can then be used to obtain all the values of ω along this wall-normal line. Repeating this process for all streamwise stations and all spanwise wavenumbers (where applicable) allows us to obtain a complete solution to the vorticity transport equation.

3.3 Poisson equation solver

The basic approach taken here to solve the Poisson equation is to reduce the partial differential equation to several ordinary differential equations which are then solved independently. This is done by applying compact finite differences to the streamwise derivatives, and then applying a sine transformation which, in conjunction with the use of trigonometric identities, allows each streamwise wave number to be dealt with independently. We use the following fourth order compact finite difference relationship:

$$\frac{u_{z;j-1} - 2u_{z;j} + u_{z;j+1}}{\Delta x^2} = \frac{1}{12} \frac{\partial^2}{\partial x^2} (u_{z;j-1} + 10u_{z;j} + u_{z;j+1}) + O(\Delta x^4), \tag{3.36}$$

where j is a counter for the streamwise nodes of the domain discretisation. Once again, as in section 3.2.2, we use \approx to indicate that the equalities are approximate to within

fourth-order accuracy in space (time, of course, does not appear in the Poisson equations). Substituting this into the 3D Poisson equation 2.16, we obtain a semi-discretised equation which relates the values of w and its wall-normal and spanwise derivatives at any streamwise station to their values at neighbouring stations:

$$\frac{u_{z;j-1} - 2u_{z;j} + u_{z;j+1}}{\Delta x^2} + \frac{1}{12} \left(\frac{\partial^2}{\partial z^2} - \beta^2 \right) (u_{z;j-1} + 10u_{z;j} + u_{z;j+1}) = f_j$$
 (3.37)

In the 2D Poisson equation, the term β^2 , representing the second spanwise derivative, does not appear. The term f_j on the right hand side contains an average of the terms from the right-hand side of the 2D or 3D Poisson equations 2.19 or 2.16:

$$f_{j;2D} = \frac{-1}{12} \left(\frac{\partial \omega_{y;j-1}}{\partial x} + 10 \frac{\partial \omega_{y;j}}{\partial x} + \frac{\partial \omega_{y;j+1}}{\partial x} \right)$$
(3.38)

$$f_{j;3D} = \frac{1}{12} \left[i\beta \omega_x - \frac{\partial \omega_y}{\partial x} \right]_{j-1} + \frac{5}{6} \left[i\beta \omega_x - \frac{\partial \omega_y}{\partial x} \right]_j + \frac{1}{12} \left[i\beta \omega_x - \frac{\partial \omega_y}{\partial x} \right]_{j+1}$$
(3.39)

 $f_{j;2D}$ and $f_{j;3D}$ are very similar; the only difference is the appearance of spanwise derivatives of ω_x (i.e., $i\beta\omega_x$) in the three-dimensional case. As mentioned above, we intend to decouple the streamwise locations from one another by applying a sine transformation for the streamwise variation of the wall-normal velocity w. However, if a sine transform is to be performed on a variable, it is necessary that its value goes to zero at the limits of its domain; in this case, at the nodes j=0 (the inlet) and j=J (the outlet). The inlet boundary condition already specifies that $u_{z;0}=0$, but the outlet boundary condition does not. In order to use the sine transformation we therefore introduce a new variable $\tilde{u_z}$, equal to u_z everywhere except at the streamwise node J. Thus, the equation above holds for each node $1 \le j \le J-2$, and at the node j=J-1, we have instead:

$$\frac{\tilde{u}_{z;J-2} - 2\tilde{u}_{z;J-1}}{\Delta x^2} + \frac{1}{12} \left(\frac{\partial^2}{\partial z^2} - \beta^2 \right) \left(\tilde{u}_{z;J-2} + 10\tilde{u}_{z;J-1} \right) =
\frac{1}{12} \left[\beta \omega_x - \frac{\partial \omega_y}{\partial x} \right]_{J-2} + \frac{5}{6} \left[\beta \omega_x - \frac{\partial \omega_y}{\partial x} \right]_{J-1} - \frac{u_{z;J}}{\Delta x^2} - \frac{1}{12} \left(\frac{\partial^2}{\partial z^2} - \beta^2 \right) u_{z;J} \quad (3.40)$$

This is a statement of the 3D equation; to get the equivalent statement for the 2D equation simply set $\beta = 0$. We now define a function \tilde{f} , equal to f at nodes $1 \leq j \leq J-2$, and equal to the right-hand side of equation 3.40 at node j = J-1. It can be seen that, in order to calculate the right-hand side of the difference equation at this node, we need to know $u_{z,J}$; however, we are not given a Dirichlet condition for the velocity at this location. Instead, we are given a condition relating the velocity to its second streamwise derivative, as described in section 2.2.2. Substituting this boundary condition into the Poisson equation, we are left with:

$$\left(\frac{d^2}{dz^2} - \alpha^2 - \beta^2\right) u_{z;J} = \left[i\beta\omega_x - \frac{\partial\omega_y}{\partial x}\right]_J$$
(3.41)

The β^2 and ω_x terms are dropped in the 2D case. We can apply compact finite differences in the same manner as in the vorticity transport equations to deal with the wall-normal derivative. We can then solve using the Thomas alorithm as before, since we have simple Dirichlet conditions on u_z both at the wall and at infinity. Using these calculated values for $u_{z;J}$, \tilde{f}_{J-1} can be obtained.

At this point the sine transformation alluded to earlier can be applied:

$$\tilde{u}_{z,j} = \sum_{m=0}^{J} \hat{u}_{z,m} \sin(\frac{jm\pi}{J})$$
(3.42)

Note that, since \tilde{f} is only specified for the nodes $1 \leq j \leq J-1$, we can set it to zero at the inlet and outlet, and therefore can apply the same sine transformation. Note also that this sine transformation is only applicable if our node spacing is uniform throughout the domain, as mentioned in section 3.1.1. Making these substitutions, we obtain:

$$\left(\frac{1}{\Delta x^2} + \frac{1}{12} \left(\frac{d^2}{dz^2} - \beta^2\right)\right) \sum_{m=0}^{J} \hat{u}_{z;m} \left(\sin\left(\frac{(j-1)m\pi}{J}\right) + \sin\left(\frac{(j+1)m\pi}{J}\right) + \left(\frac{-2}{\Delta x^2} + \frac{5}{6} \left(\frac{d^2}{dz^2} - \beta^2\right)\right) \sum_{m=0}^{J} \hat{u}_{z;m} \sin\left(\frac{jm\pi}{J}\right) = \sum_{m=0}^{J} \hat{f}_m \sin\left(\frac{jm\pi}{J}\right) \quad (3.43)$$

Using suitable trigonometric identities, the offset sine terms (i.e., those for which $(j \pm 1)$ appear in the argument) can be eliminated and the entire equation can be recast in terms of sine functions of one particular wave number. Because of the linear independence of sine functions of different wave numbers, the equation holds for each wave number individually. If we define a variable σ_m by:

$$\sigma_m = \cos\frac{m\pi}{J},\tag{3.44}$$

then we can write the following ordinary differential equation for each wavenumber m:

$$\left[\frac{2}{\Delta x^2}(\sigma_m - 1) + \frac{(\sigma_m + 5)}{6} \left(\frac{d^2}{dz^2} - \beta^2\right)\right] \hat{u}_{z;m} = \hat{f}_m$$
 (3.45)

Thus, our first step is to apply the sine transformation in equation (3.42) to the right-hand side of our equation in the space domain, then to solve the frequency domain ODE, equation (3.43). There are natural Dirichlet conditions on the variable u_z ; the no-slip and no-penetration condition means that the velocity at the wall is fully specified, and because we are dealing with perturbation variables, the velocity tends to zero as the wall-normal distance tends to infinity. Since the velocity at these wall-normal stations is specified at all streamwise locations, it is trivial to perform the same sine transformation and obtain Dirichlet conditions at both ends of the wall-normal domain for all streamwise wave numbers.

The wall-normal differential operator that appears is simply d^2/dz^2 , and therefore compact finite differences can be used as before. This allows us, after performing the wall-normal transformation and applying the discretisation discussed in section 3.2.2, to recast the sine-transformed Poisson equation as follows. Note that the wall-normal node counter has been rendered as superscript in this instance to prevent excessive piling-up of subscripts.

$$k^{3} \left(\frac{\sigma_{m} - 1}{5\Delta x^{2}(k-1)^{3}} + \frac{\sigma_{m} + 5}{6} \left[\frac{\Delta \eta^{2}(k-1)}{l^{2}} - \frac{\beta^{2}}{12(k-1)^{3}} \right] \right) \hat{u}_{z,m}^{k-1}$$

$$+ \left(\frac{2}{\Delta x^{2}}(\sigma_{m} - 1) - (\sigma_{m} + 5) \left[\frac{\beta^{2}}{6} + \frac{2\Delta \eta^{2}k^{4}}{5l^{2}} \right] \right) \hat{u}_{z,m}^{k}$$

$$+ k^{3} \left(\frac{\sigma_{m} - 1}{5\Delta x^{2}(k+1)^{3}} + \frac{\sigma_{m} + 5}{6} \left[\frac{\Delta \eta^{2}(k+1)}{l^{2}} - \frac{\beta^{2}}{12(k+1)^{3}} \right] \right) \hat{u}_{z,m}^{k+1}$$

$$= \hat{f}_{m}^{k} + \frac{k^{3}}{10} \left(\frac{\hat{f}_{m}^{k-1}}{(k-1)^{3}} + \frac{\hat{f}_{m}^{k+1}}{(k+1)^{3}} \right)$$
 (3.46)

Like the discretised version of equation (3.41), this gives us a system of tridiagonal equations (one for each streamwise wavenumber) which can be solved with the Thomas algorithm.

3.4 Complete program

When writing the complete program using the techniques described above, the first thing to note is that a great deal can be precomputed. For instance, the coefficients associated with the discretisations of the vorticity transport equation and Poisson equation can be calculated before the main run of the program, as well as the variables μ_k and δ_k from section 3.2.4 and their analogues from the solution of the Poisson equation.

Secondly, given that we are using a time discretisation that requires information from two previous time levels, we need to consider what we will use as initial conditions. It was thought that the most straightforward way to deal with this difficulty would be to start from a solution that is identically zero everywhere, which clearly satisfies the governing equations. We will then introduce some non-zero perturbation in t>0 by some suitable means, such as suction/blowing at the wall or body forcing. Note that formally this scheme is not well-posed, since in setting the solution to zero for the times t=0 and $t=-\Delta t$ at the first time step the statement of the problem becomes over-specified; this formal problem could have been overcome by bootstrapping the first step with a suitable

Runge-Kutta scheme, but in practice presented no real difficulties.

We now give a basic outline of the structure of the solver. Statements that appear in italics are not relevant to the 2D solver.

Initialise precomputable parameters and solution variables

BEGIN TIME LOOP

Increment time

Start of first iteration

Solve streamwise vorticity transport equation using Adams-Bashforth projections for explicit terms and integral condition

Solve spanwise vorticity transport equation using Adams-Bashforth projections for explicit terms and integral condition

Solve Poisson equation for wall-normal velocity

BEGIN ITERATION LOOP

Start of subsequent iterations

Solve streamwise vorticity transport equation using most recent values for explicit terms and integral condition

Solve spanwise vorticity transport equation using most recent values for explicit terms and integral condition

Solve Poisson equation for wall-normal velocity

Check for convergence; if converged, exit iteration loop

END ITERATION LOOP

Update stored variables

If required, output data

END TIME LOOP

Chapter 4

Solver validation

4.1 Order of accuracy

In order to verify that the numerical method is as accurate as expected, we perform grid refinement studies for simplified cases for which exact analytic solution exist. In order to do this, the Poisson solver and VTE solver were decoupled. This gives us a pair of model equations to solve which are representative of the real governing equations discussed in chapter 2. These equations are:

$$\frac{\partial f}{\partial t} = \frac{\Delta f}{Re} + \Phi \tag{4.1}$$

$$\Delta g = \Psi \tag{4.2}$$

Here the variables Φ and Ψ are chosen such that they specify the desired solutions to the model equations.

For the decoupled VTE, we used $\Phi = (\frac{\beta^2}{Re} - 1)e^{-(z+t)}\sin x$, corresponding to a solution $f = e^{-(z+t)}\sin x$, with a spanwise wavenumber $\beta = 0.15$ and Reynolds number Re = 1000. The spatial domain used was semi-infinite in the z-direction, with the transformation described in section 2.2.1 applied. In the x-direction the limits were $0 \le x \le 5$. The

problem was initiated at time t=0, with the initial condition on f being the exact solution at that time. The problem was allowed to develop until t=0.1. To verify that our numerical scheme is fourth-order accurate in space, we performed a series of simulations with a fixed timestep $\Delta t=0.005$. Each successive simulation was performed on a more fine-grained grid; the streamwise and spanwise dimensions were refined simultaneously to avoid a situation wherein the errors associated with the discretisation in one spatial dimension swamp the reduction of errors associated with the refinement of the discretisation in the other. The results of this spatial grid refinement study are presented in figure 4.1. The errors are calculated using the formula:

$$Error = \frac{\sum_{i} |f_{i} - \bar{f}_{i}|}{\sum_{i} |\bar{f}_{i}|}$$

$$(4.3)$$

Where the index i encompasses all the nodes of the discretisation, f_i is the value of the numerical solution at the node i and \bar{f}_i is the evaluation of the analytic solution at the spatial location of the node i. We see that there is the expected fourth-order reduction in error as the grid is refined. A similar procedure was followed to ensure that the time-stepping scheme preserved second-order accuracy: we use a spatial grid with fixed values for the node separation $\Delta x, \Delta \eta = 0.125$ and perform a series of calculations with progressively finer timesteps to verify the temporal accuracy. The simulation was stopped at t = 0.1 in all cases, and the error is defined as before. The results, which show the expected second-order reduction in error, are depicted in figure 4.2.

To test the accuracy of the decoupled Poisson solver, we used $\Psi = -(\beta^2 - 2)e^{-z}\sin x$ in equation 4.2, corresponding to a solution $g = ze^{-z}\sin x$. This solution was chosen because it is broadly similar to the expected forms of solution in the real problem, with the solution zero-valued both at the wall and infinitely far from the wall. For this problem, a slightly larger domain was used $(0 \le x \le 10)$. Once again, the discretisations of both spatial dimensions were refined simultaneously. The results of the refinement are shown in figure 4.3, which shows the expected fourth-order reduction in error.

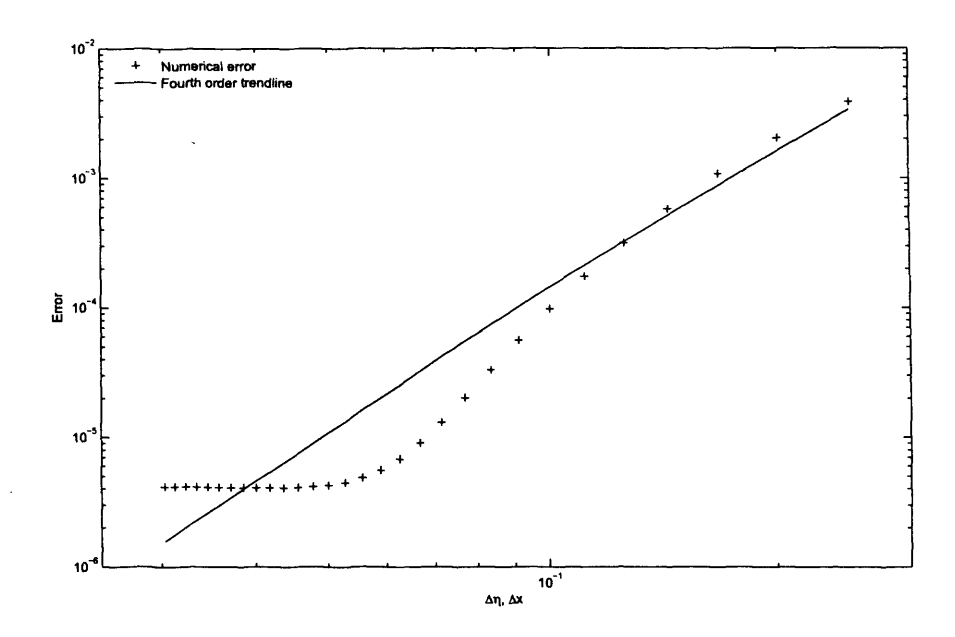


Figure 4.1: Dependence of errors on spatial grid size in decoupled VTE solver

4.2 Tollmien-Schlichting waves

Having shown that our numerical technique has the expected order of accuracy, we now seek a benchmark problem for the coupled solvers. We will test the solver's ability to predict spatially-developing Tollmien-Schlichting waves in a Blasius boundary layer. Using a form of the Orr-Sommerfeld equations, it is possible to predict the complex wavenumber of a Tollmien-Schlichting wave excited by a given frequency of perturbation, as discussed in section 2.3. This gives us a criterion by which to judge how well our solver captures this phenomenon.

Figure 4.4 shows an example of the type of solution we obtain; it has the expected form, of a spatially quasi-periodic wave with maxima at the wall and in a critical layer some distance from the wall. Some quantitative confirmation of its accuracy is also required, however; the problem is thus one of verifying that our numerical data matches the ex-

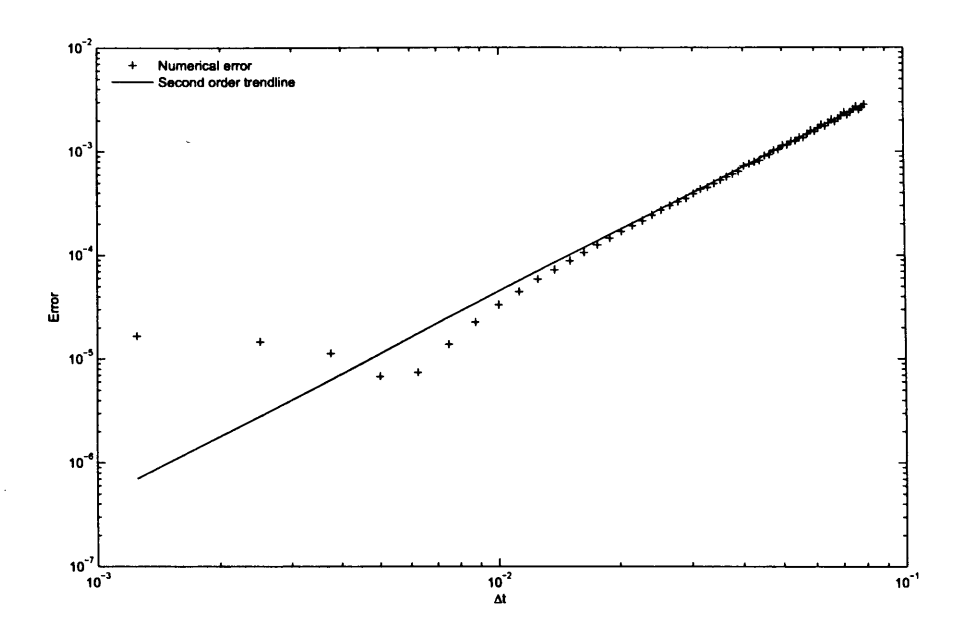


Figure 4.2: Dependence of errors on size of timestep in decoupled VTE solver

pected Tollmien-Schlichting wave. Let us assume that the numerical results, at least in some region sufficiently far downstream from the location where the temporal perturbation is introduced, have the form of a Tollmien-Schlichting wave. This means that, along any particular streamwise line at constant z, the computed values of any of the solution variables should approximate a function of the following form.

$$f(x) = Ae^{i\alpha(x-\phi)}$$

Where A is an amplitude, ϕ a phase and α a complex wavenumber. A and ϕ are not of interest. Let us examine the imaginary component of f, f_i .

$$f_i(x) = Ae^{-\alpha_i(x-\phi)}\sin[\alpha_r(x-\phi)]$$
$$= A'e^{-\alpha_i x}\sin[\alpha_r(x-\phi)]$$
(4.4)

With $A' = Ae^{\alpha_i \phi}$. We wish to determine the values α_i and α_r . Calculating a value for

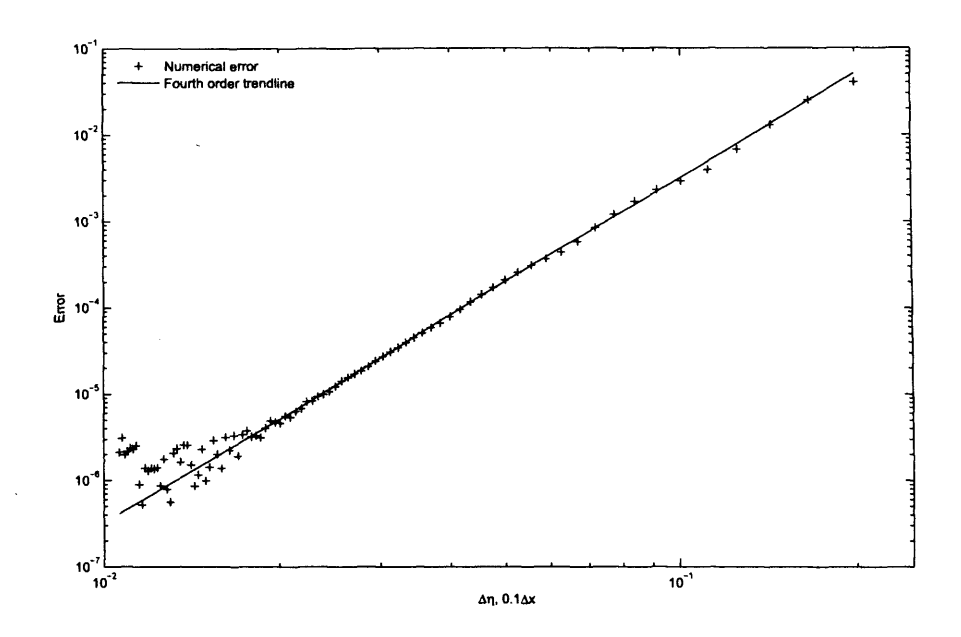


Figure 4.3: Dependence of errors on spatial grid size in decoupled Poisson solver

 α_r is in fact relatively straightforward: we simply hunt for extrema and zeroes in our data series. For finite values of x, the only zeroes that occur in f_i are those for which $\sin[\alpha_r(x-\phi)]=0$. (Note that we have assumed that α_i is finite.) Similarly, the extrema of f_i occur only where $\tan[\alpha_r(x-\phi)]=\alpha_r/\alpha_i$. The upshot of this is that if we hunt through our data for zeroes and extrema, we can use their locations to calculate α_r . Zeroes of the function $\sin(t)$ occur at intervals of π in t, and the function $\tan(t)$ is π -periodic in t. Thus, if we locate two successive zeroes at the locations x_m and x_n , we know that:

$$\alpha_r(x_m - \phi) + \pi = \alpha_r(x_n - \phi)$$

$$\alpha_r = \frac{\pi}{x_n - x_m}$$
(4.5)

This also holds if x_m and x_n represent the locations of two successive extrema. Our procedure, then, is to find the average separation of successive zeroes and successive extrema in the data set, and use this to calculate an average half-period; that is, the average value

of $x_n - x_m$ for all successive pairs (x_m, x_n) of zeroes or extrema. (This is in fact more accurately described as a quasi-half-period, since our function is not truly periodic but also exponentially growing or decaying.) Once we have obtained this average, we use it in place of $x_n - x_m$ in equation 4.5 to obtain our value of α_r .

The calculation of α_i is slightly less straightforward. If we introduce an offset variable $\xi = x - x_0$, we can recast equation (4.4) as:

$$f_i(x) = A'' e^{-\alpha_i \xi} \sin[\alpha_r (\xi + x_0 - \phi)] \tag{4.6}$$

Where $A'' = A'e^{-\alpha_i x_0}$. The phase in the trigonometric term is still problematic. However, let us assume that we choose our offset such that $f_i(\xi) = 0$ at $\xi = 0$. It must then be the case, as described above, that $\sin[\alpha_r(x_0 - \phi)] = 0$. If this is the case, then we must have $x_0 - \phi = m\pi$, $m \in \mathbb{Z}$. Thus, our phase term can be ignored. By integrating our function over successive half-periods, it is possible to show that:

$$\alpha_i = \frac{-\alpha_r}{\pi} \ln \left(\frac{-\int_{n\pi/\alpha_r}^{(n+1)\pi/\alpha_r} f(\xi) d\xi}{\int_{(n-1)\pi/\alpha_r}^{n\pi/\alpha_r} f(\xi) d\xi} \right)$$
(4.7)

Thus, by calculating a numerical approximation to the integrals in the above expression, and using the value of α_r that has been calculated using the method described above, an approximate value for α_i can be determined. This method allows us to calculate both parts of the complex wavenumber of the spatially developing wave described by our data set. We can compare this to the expected wavenumber from the Orr-Sommerfeld solver described in section 2.3 in order to test the validity of our results. Some of these results are tabulated in tables 4.2 and 4.2; recall that γ is the real-valued frequecy of the perturbation used to excite the Tollmien-Schlichting waves.

We see that the values of α_i and, particularly, α_r calculated from our numerical data agree quite well with the values predicted by the Orr-Sommerfeld solver. A particularly satisfactory result is that the sign of α_i is preserved in all instances; in other words, our

Re	γ	Expected α_r	Computed α_r	Percentage error
10 ⁴	0.03	0.11691	0.11714	0.197%
10^{5}	0.05	0.18104	0.18009	-0.525%
	0.04	0.15369	0.15377	0.052%
	0.03	0.12329	0.12352	0.187%
	0.02	0.088171	0.088496	0.369%
	0.015	0.068428	0.068094	-0.488%
	0.01	0.048404	0.048332	-0.149%
	0.005	0.023258	0.023271	0.056%
10^{6}	0.005	0.024537	0.024529	-0.033%
	0.004	0.019661	0.019565	-0.488%
	0.003	0.014732	0.014784	0.353%
	0.002	9.768×10^{-3}	9.8277×10^{-3}	0.61%

Table 4.1: Comparison between real part of expected and calculated Tollmien-Schlichting wavenumbers for $\beta=0.15$

Re	γ	Expected α_i	Computed α_i	Percentage error
10 ⁴	0.03	-8.8445×10^{-3}	-8.7833×10^{-3}	-0.692%
10^{5}	0.05	8.4486×10^{-3}	8.4711×10^{-3}	0.266%
	0.04	5.94×10^{-3}	6.2396×10^{-3}	5.044%
	0.03	3.613×10^{-3}	3.4886×10^{-3}	-3.443%
	0.02	1.4857×10^{-3}	1.4782×10^{-3}	-0.505%
	0.015	1.0289×10^{-3}	1.0316×10^{-3}	0.262%
	0.01	-1.096×10^{-5}	-2.9031×10^{-6}	-73.512%
	0.005	-2.3011×10^{-3}	-2.2949×10^{-3}	-0.269%
10^{6}	0.005	4.1833×10^{-4}	4.0853×10^{-4}	-2.343%
	0.004	2.7934×10^{-4}	3.1117×10^{-4}	11.395%
	0.003	1.4438×10^{-4}	1.4873×10^{-4}	3.013%
	0.002	7.317×10^{-5}	7.2484×10^{-5}	-0.938%

Table 4.2: Comparison between imaginary part of expected and calculated Tollmien-Schlichting wavenumbers for $\beta=0.15$

solver always correctly predicts the presence of spatial growth or decay.

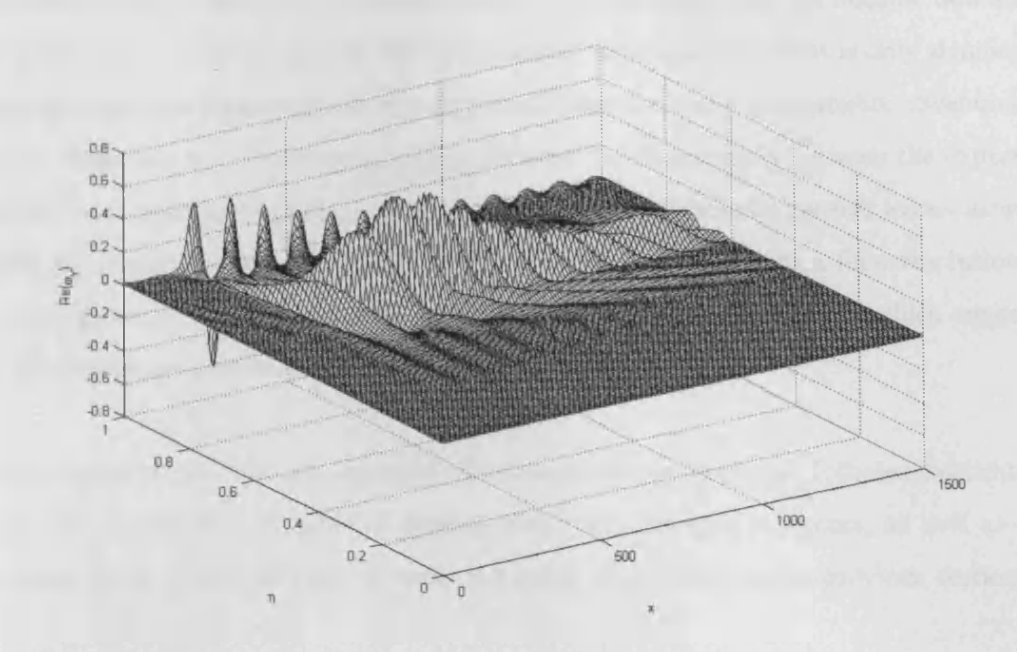


Figure 4.4: Example of a Tollmien-Schlichting solution obtained using our compact finite difference solver. Solution parameters are $Re = 10^5$, $\gamma = 0.05$; plotted variable is $Re(\omega_y)$, the real part of spanwise vorticity.

The numerical values of α_i do not match the expected values as well as the numerical values of α_r , but they are still in most cases quite satisfactory. One factor that explains the bigger discrepancies for α_i is, simply, that the absolute values of α_i are significantly smaller than those of α_r for almost every case. Thus, even a very small absolute error in α_i can cause quite a large relative error. Indeed, the case with $Re = 10^5$ and $\gamma = 0.01$, which has the largest percentage error in α_i , has an absolute error in α_i which is among the smallest of any of the cases, and only appears relatively large because the expected value of α_i is roughly an order of magnitude smaller than in any other case. A more careful examination of the data obtained from simulations performed with these parameters shows that the few wavelengths of the resultant Tollmien-Schlichting wave which lie

closest to the outlet boundary exhibit a slightly greater growth than those parts of the wavetrain closer to the interior of the domain. This suggests that the outflow boundary affects the spatial development of the waves subtly, such that the effect is only significant where the expected magnitude of αi is very small. Recalculating the complex wavenumber without these last few wavelengths of data reduces the discrepancy between the expected analytic value and the numerical value by almost a half, although this still leaves us with a quite significant difference. Performing the simulations again with a finer resolution in the streamwise direction showed no significant effect on the error in α_i , which suggests that the waves are satisfactorily resolved.

We can therefore say that our complete solver satisfactorily captures Tollmien-Schlichting waves, and is therefore capable of dealing with more realistic problems, as well as the simplified model solutions used to verify the order of accuracy in the previous section.

4.3 Spanwise forcing

We elected to investigate the case where the oscillating wall included a stationary section in the region nearest the inlet and an oscillating panel further downstream. This means there will need to be at least some part of the domain where there is streamwise variation, which will introduce three-dimensional effects that may significantly influence the numerical solution. For this reason it was decided that it would be productive to perform some preliminary numerical calculations using a simplified version of the numerical formulation with no streamwise development. These calculations, in common with those from the fully three-dimensional solver, used zero initial conditions and a ramping up of the excitation. Recall that the analytic solution for ω_x takes the (complex-valued) form:

$$\omega_x(y, z, t) = \hat{u}_y^*(\beta + \nu) \exp(i(\beta y - \gamma t) - \nu z)$$
(4.8)

Where ν is defined by $\nu^2 = \beta^2 - i\gamma Re$, $Re(\nu) > 0$ and \hat{u}_y^* is the amplitude of the wall oscillation. Some results from these calculations are presented below in figure 4.5.

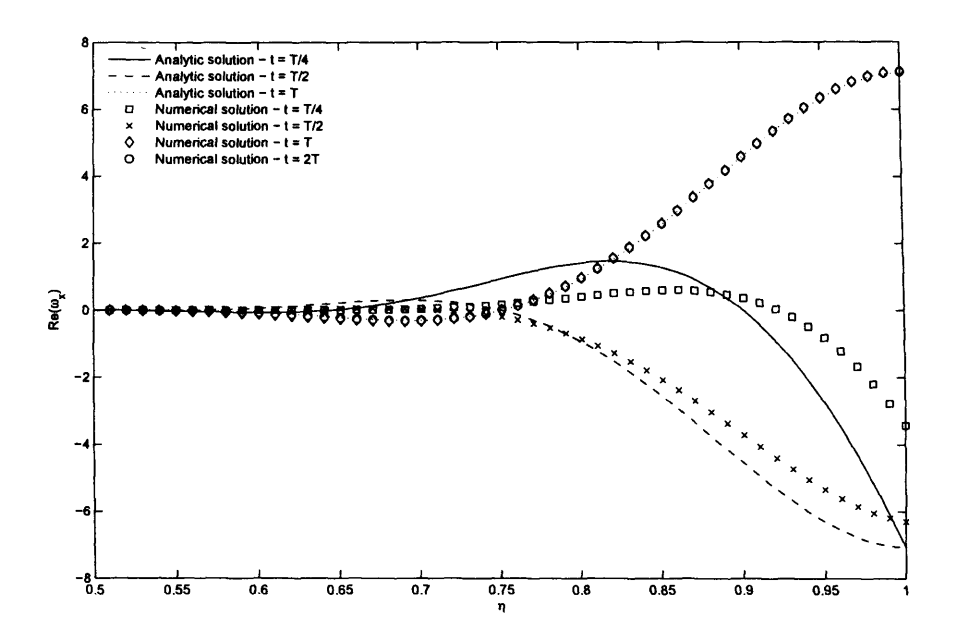


Figure 4.5: Comparison of 2D model solutions for spanwise excitation with analytic solutions. Solution parameters: Re = 10000, $\gamma = 0.01$, $\beta = 0$. T is the period of the spanwise oscillation.

It is seen that the numerical solution very quickly tends toward the analytic solution. Even by a quarter of the way through the first cycle of the spanwise oscillation, the numerical solution is already qualitatively very similar to the analytic solution, and by the end of the first full cycle the solutions are almost indistinguishable. Repeating the simulations with frequencies of an order of magnitude higher or lower gave similar agreement. This gives us reason to believe that the use of zero initial conditions the three-dimensional solver should not introduce numerical instability due to explosively-growing transients or similar problems.

Having obtained satisfactory results with a simplified two-dimensional solver, we now consider how to deal with the spanwise excitation in the three-dimensional solver, as

mentioned above. The streamwise variation of \hat{u}_y^* (recall that this is the amplitude of the wall oscillation, as defined in section 2.5) goes from zero at the inlet, to some constant non-zero value downstream. The region of transition should be sufficiently smooth to avoid numerical difficulties. It was decided that the simplest solution was to use a hyperbolic tangent function, given below.

 $\hat{u}_y(x) = \frac{\hat{u}_y^*[\tanh(S(x - L_s)) + 1]}{2}$ (4.9)

Here S is a factor controlling the steepness of the profile in the step (the larger the value of S, the steeper the slope), and L_s is the location about which the step is centred. A caricature of the solution domain is shown in figure 4.6; this depicts the plate on which the boundary layer is developing. Note that the spanwise extent of the domain is purely notional, since we are dealing with a single spanwise wavenumber rather than a bounded spanwise space; the plate is simply drawn this way for ease of visualisation. A sketch of the $\hat{u}_y(x)$ obtained from equation 4.9 is included in this caricature.

In figure 4.7, we see that the wall-normal profiles of $Re(\omega_x)$, the real part of the streamwise vorticity, from the three-dimensional solver also agree well with the analytic solutions, and in fact are almost indistinguishable from the two-dimensional solutions. Note that the data were taken from the outlet boundary. This sampling location was chosen because it was expected that the data furthest downstream would be least influenced by the three-dimensional effects. Tests showed that the solution values on the outflow were relatively insensitive to changes in the value of α in the outflow boundary condition (as expressed in equation 2.29). Note that in these cases it was not necessary to take complex-valued variables, since we used $\beta=0$, and under these circumstances the real and imaginary components decouple. However, since we had developed a solver that utilised complex variables, we saw no reason not to use the full complex wall oscillation defined by $\hat{u}_y = \hat{u}_y^* e^{i\gamma t}$, which excited a complex response.

In order to further investigate three-dimensional effects, a selection of simulations were

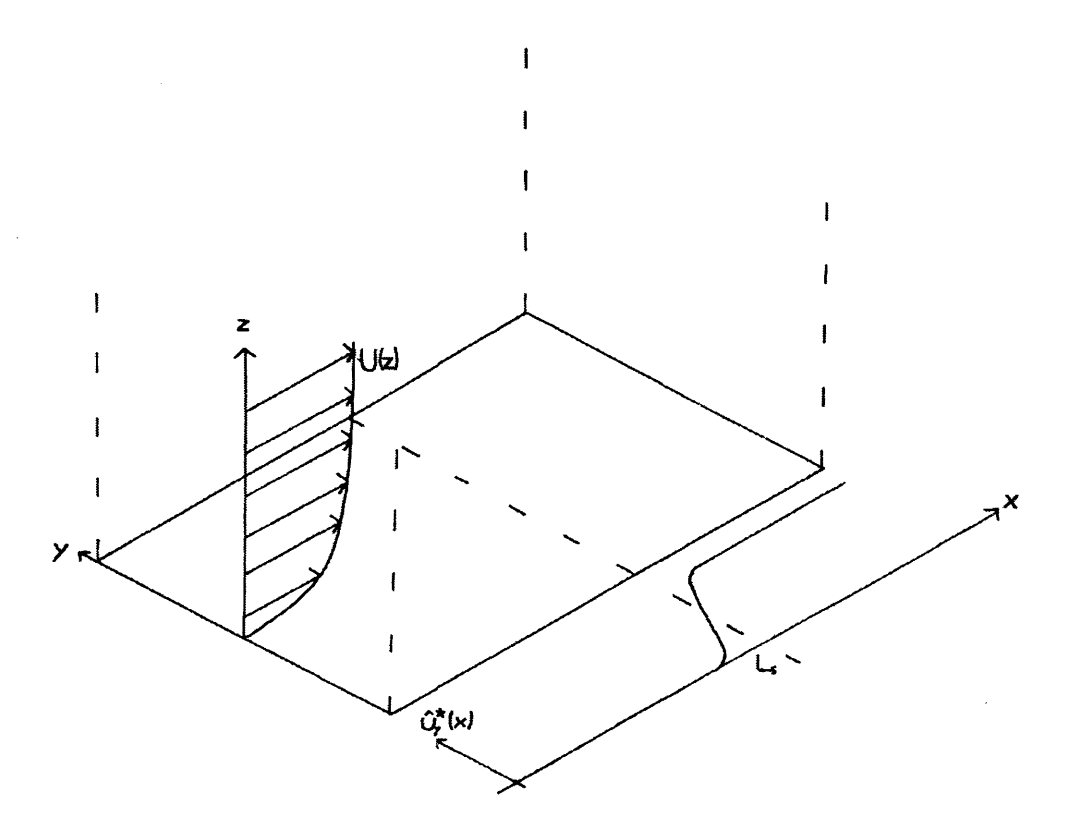


Figure 4.6: Sketch of the solution domain; the form of the streamwise variation of \hat{u}_{y}^{*} , the amplitude of the spanwise wall oscillation, is shown to the right of the flat plate which creates the boundary layer basis flow.

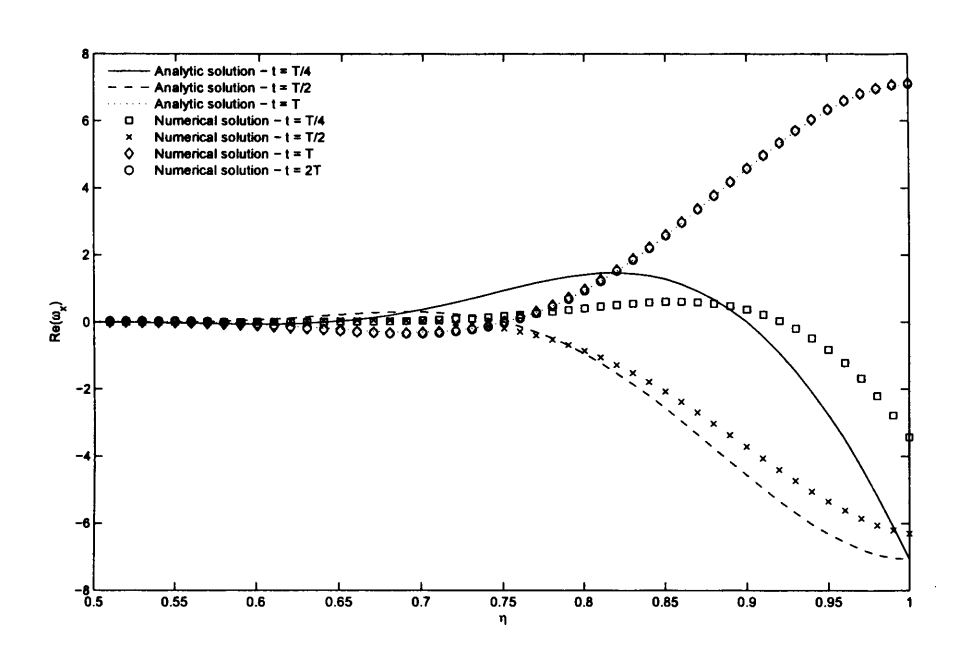


Figure 4.7: Comparison of 3D model solutions for spanwise excitation with analytic solutions. Solution parameters: Re = 10000, $\gamma = 0.01$, $\beta = 0$. T is the period of the spanwise oscillation.

performed in which Re was varied but the product γRe kept constant. Keeping the same value of γRe meant that the two-dimensional analytic solutions were identical, since both γ and Re only appear in the analytic solution through the parameter ν , and in the definition of ν (given in section 2.5 and reiterated above), they appear multiplied together. Some results of this series of simulations are presented in figure 4.8, which presents values of $Re(\omega_x)$ along the wall. The streamwise location along the wall is expressed as $x-L_s$: in other words, the distance downstream of the step location. We see that, for larger Reynolds numbers, the three-dimensional effects due to the step extend further downstream, but that by the outflow boundary $Re(\omega_x)$ at the wall has settled down to a value near the two-dimensional solution. Looking again at 4.7, though, we can see that this discrepancy in the wall values is small compared to the variation of the profiles in the wall-normal dimension.

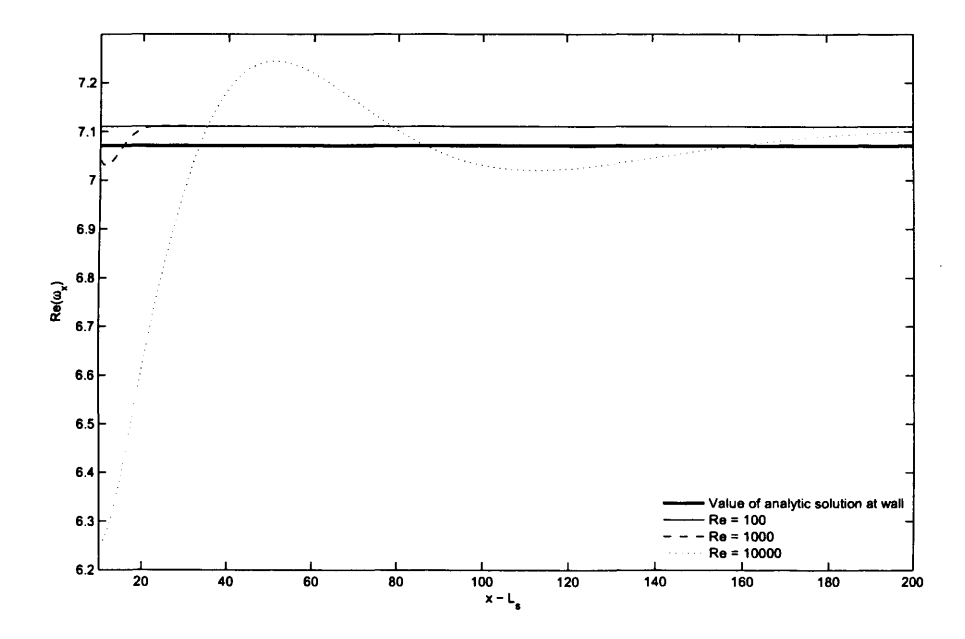


Figure 4.8: $Re(\omega_x)$ at the wall for different Reynolds numbers, compared to value of $Re(\omega_x)$ at the wall for 2D analytic solution. $\gamma Re = 100$. Data taken from the time after two complete oscillations have elapsed.

Chapter 5

Turbulent streaks

Before investigating the influence of spanwise wall forcing on streak development, we need to perform some simulations of the streaks alone without any wall motion to determine if our reduced-order model of streaks, with our implementation of compact finite differences, gives realistic results. The problem we now face is how to generate streaks in a practical and physically meaningful way. The approach we decided to implement was based on that of Fasel, who used a spatially localised force to generate Klebanoff modes in laminar boundary layers [27]; these are in some respects quite similar to streaks in turbulent boundary layers. Fasel used a disturbance which simulated a body force that could be practically implemented in an experiment; since he employed, as we do, a velocity-vorticity formulation of the governing equations, this means the force appears as a cross-product i.e., as the spatial derivatives of a force rather than the force itself. Fasel's method has been adapted by Lockerby et al and Carpenter et al [11,48] to generate streaks in a turbulent boundary layer, and we will employ the same approach. This involves introducing a forcing of the following form:

$$F = A(t)\exp[-k_x(x - x_f)^2 - k_z(z - z_f)^2]$$
(5.1)

This is in the form of a Gaussian, with A(t) the amplitude as a function of time, x_f and z_f the spatial coordinates around which the forcing is centred, and k_x and k_z pa-

rameters which describe how quickly the Gaussian profiles decay in the streamwise and wall-normal directions respectively. The most significant difference between this and the forcing strategy of Fasel is that this term acts as a vorticity source which does not correspond to a physically realisable forcing. F is introduced as an additional term in the secondary perturbation form of the streamwise VTE, equation 2.22, which is dealt with numerically by simply adding it to the explicit terms of equation 3.18. We also need to remember that, although we are only imposing a forcing term on the streamwise vorticity, due to the solendoidality of ω , this entails an induced wall-normal vorticity as well. Brief consideration of the solenoidality condition reveals that the wall-normal vorticity is of the form of two stripes of positive and negative vorticity between the point of application of F and the wall.

Unlike their laminar counterparts, turbulent wall-bounded flows are linearly stable: there is no equivalent to the growing Tollmien-Schlichting waves that embody the classical route to transition [64]. Of course, if there were any such linear instabilities, we would already have an answer to how turbulence sustains itself and there would be no need to investigate streaks. Despite this lack of linear instability, it is still possible for a perturbation to a turbulent boundary layer to grow significantly in a short period of time; it must, however, eventually decay as $t \to \infty$. The mechanisms by which this happens are explained in some detail by Henningson $et\ al$. and by Trefethen $et\ al$. [29,76], but we will briefly discuss them here. Let us obtain a linearised perturbation form of the momentum transport equations, derived from equation 2.1 in the same way equation 2.7 is derived from equation 2.3.

$$\frac{\partial \mathbf{u}}{\partial t} + (\mathbf{U}_B \cdot \nabla)\mathbf{u} = -\nabla p + \frac{\Delta \mathbf{u}}{Re}$$
 (5.2)

We can recast this using operator notation:

$$\frac{\partial \mathbf{u}}{\partial t} = \mathbf{L}(\mathbf{u}) \tag{5.3}$$

The linear stability of the turbulent boundary layer means that all the eigenvalues of the

operator L have negative real parts. However, L in this problem is non-normal, meaning that its eigenfunctions do not form an orthogonal set. The upshot of this is that, although each individual mode decays, their superposition may not necessarily do so. In cases, such as the generation of streaks, where initial growth is observed, we can divide the overall history of the perturbation into a strong algebraic transient growth phase followed by an exponential viscous decay.

As described in chapter 3, our numerical scheme takes advantage of the linear formulation of the governing equations by simulating only a single spanwise wavenumber in any given solver run. The scheme thus imposes a spanwise wavelength, which we denote by λ , on the streak. This may not match the corresponding length scale for the streaks that evolve in real turbulent boundary layers. In order to overcome this restriction, we perform a search across a range of values for λ and z_f to find the streak whose magnitude is the greatest for some appropriate measure. We then make the further assumption that the disturbances present in real turbulent boundary layers which we have modelled by equation 5.1 occur with roughly equal probability across the range of (λ, z_f) pairs investigated. Then, we can say that the greatest-magnitude streak is selected by the basis flow since, given our assumed equally-probable set of disturbances at different (λ, z_f) pairs, one particular pair will produce the strongest streaks, and therefore the streaks that would be observed in a real turbulent boundary layer. We call these the optimum streaks. We hope to find optimum streaks whose development is a function of the basis turbulent boundary layer only i.e., unaffected by the fine details of the initial forcing.

However, we are still somewhat putting the cart before the horse. How do we measure the magnitude of the induced streaks? The criterion by which streak magnitude ought to be measured remains a point of contention. Some sources have used a criterion based on the total amount of energy contained in the streak after some time has elapsed as compared to the energy of the initial perturbation; see for instance the work of Butler and Farrell [9]. This time limitation is imposed in order to take account of random tur-

bulent motions; it is assumed that nominally possible streak-like events that occur over a time longer than the turbulent time scale (called the 'eddy turnover time') are disrupted by these random motions and thus do not occur in real turbulent boundary layers. Other sources simply take the maximum value in the streaky velocity field during the algebraic growth period as the streak magnitude [48]. This is the criterion we use here. Different criteria may turn up different results; thus, when we talk about finding an optimum streak it should be borne in mind that this optimum is only with respect to the magnitude criterion employed, and is not a universal optimum. A possible alternative is to examine the time history of the maximum velocity value, and take the initial slope during the growth phase as a measure of the streak strength. Intuitively this is a more direct measure of the algebraic growth than taking the maximum value, which is determined by a balance between initial transient growth and eventual viscous dissipation. However, for the most important practical cases it was found that the maximum velocity value in early streak development was swamped by the non-physical velocities associated with the forcing term given in equation 5.1.

Several simulations were run in order to find the optimum streaks; streak strength was determined using the simple maximum criterion. Note that in addition to the variation of wall-normal forcing location z_f^+ and spanwise wavelength λ^+ , we can vary other parameters that define the forcing: notably, k_x and k_z . In common with the results of Carpenter et al [11], we find that the streak response is relatively insensitive to variations in k_z , but can be changed significantly by altering the value of k_x . Furthermore, the variation of the forcing in time can also be changed, and was found to alter the generation of streaks quite profoundly. This is explored in more detail in section 5.2; for the results presented in other sections, we use the same approach as Lockerby et al [48] and use a forcing that is switched on for times $t^+ < 15$ and switched off at all other times. This follows the experimental work of Gad-el-Hak et al., who found that this timing when used with localised suction produced the best streaks on a towed flat plate. The switching is abrupt, so we refer to the time profile of this forcing scheme as Heaviside-like. All results presented are

for a displacement Reynolds number of 10⁴ unless noted otherwise.

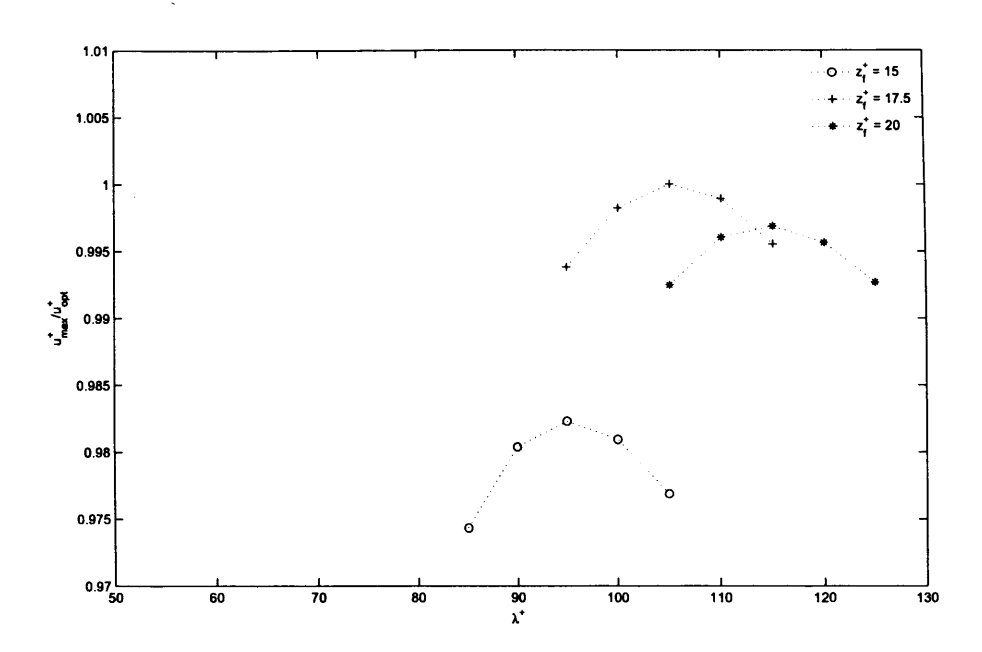


Figure 5.1: Relative streak magnitude for Gaussian perturbation in ω_x at various heights and spanwise wavelengths, with k_x chosen such that the streamwise half-width of the Gaussian profile is $x_{hw}^+ = 300$

5.1 Influence of k_x

The parameter k_x controls how quickly the streak-generating forcing 5.1 decays in the x(i.e. streamwise) direction. We specify k_x here not by its numerical value, but by the
corresponding streamwise half-width, x_{hw} . This half-width is defined as the distance one
must travel along the x-direction from the peak of the Gaussian to a point where the
forcing is 1% of its peak value. It is easily seen from equation 5.1 that the relationship
between k_x and x_{hw} is:



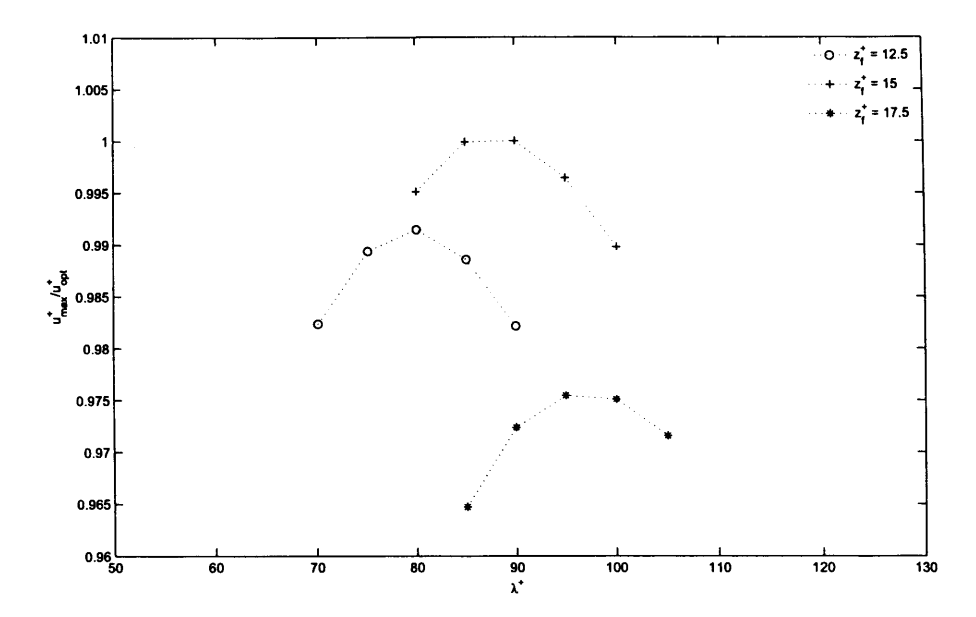


Figure 5.2: Relative streak magnitude for Gaussian perturbation in ω_x at various heights and spanwise wavelengths, with k_x chosen such that the streamwise half-width of the Gaussian profile is $x_{hw}^+ = 150$

We hope to find that, with careful selection of k_x and other parameters, it is possible to use the forcing profile 5.1 to generically model the disturbances in real turbulent boundary layers. By this, we mean that we hope to find that there exists, among the set of all possible perturbations in such boundary layers, a class of perturbations including both those modelled by 5.1 and those that are found in real turbulent boundary layers. Furthermore, we hope that this class is such that any two members of it generate essentially identical streak responses. Were this the case, we could be assured that the precise details of the disturbance do not need attention, and a relatively straightforward disturbance model like 5.1 is satisfactory. If we assume that the most common perturbations in real boundary

layers are small-scale, both temporally and spatially, the sensible approach is to investigate the changes in streak response as we alter the parameters of 5.1 to make the forcing profile more pointlike.

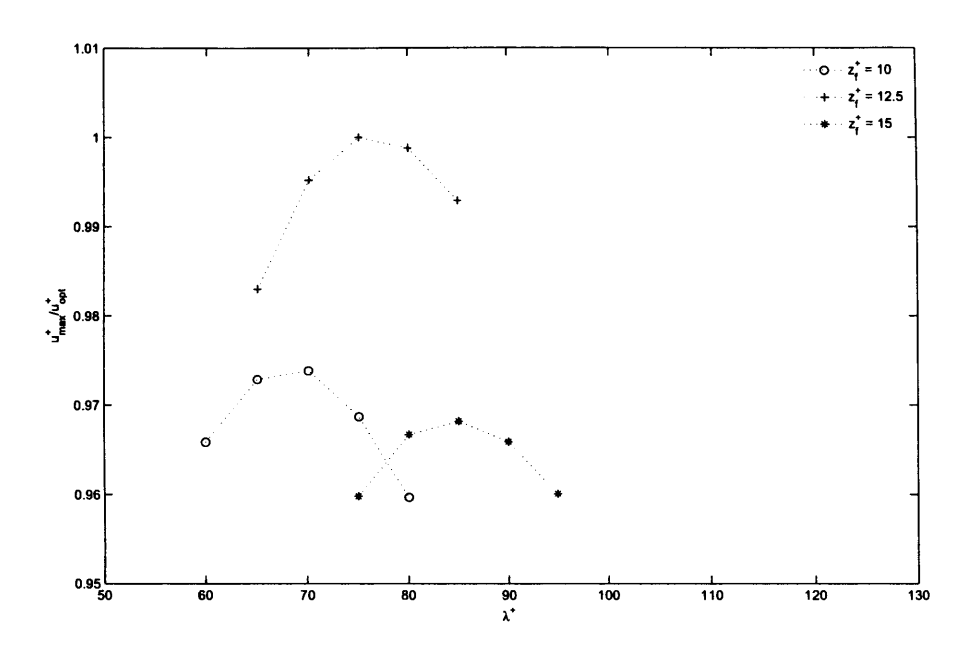


Figure 5.3: Relative streak magnitude for Gaussian perturbation in ω_x at various heights and spanwise wavelengths, with k_x chosen such that the streamwise half-width of the Gaussian profile is $x_{hw}^+ = 30$

Figures 5.1 to 5.4 present the maximum streak magnitudes for a selection of (λ^+, z_f^+) pairs, normalised by the maximum magnitude of the optimum streak. Each graph corresponds to a different k_x value; they are shown in order of x_{hw}^+ , from broadest to narrowest. It is clearly seen that, as the streamwise half-width of the forcing profile decreases, the tendency is for the optimum streak to occur at lower values of both z_f^+ and λ^+ . A comparison of figures 5.3 and 5.4 shows that by the time the x_{hw}^+ is reduced to around 30, further narrowing of the forcing profile no longer has any significant affect. Results from simula-

tions performed with a half-width of 7.5 confirm this, but are not shown here since they are indistinguishable from the results with a half-width of 15. The final optimum streak obtained is at $z_f^+ = 12.5$, $\lambda^+ = 75$. The spanwise spacing is somewhat lower than the commonly-given value of 100 wall units, but is well within the experimentally observed values of $\lambda^+ = 120 \pm 52$ reported by Zacksenhouse [82]. It is also in close agreement with the optimum streak found by Cossu *et al.* in their numerical investigation using an energy-based criterion, $\lambda^+ = 81.5 \pm 1$ [19]. Consider also that we are picking out the most strongly amplified streak, and thus the one that will be observed most often; it is thus more suitable to compare this to the median observed streak spacing rather than the mean, and this is the value given by Cantwell, in a review of several sets of experimental data, as 80 wall units [10].

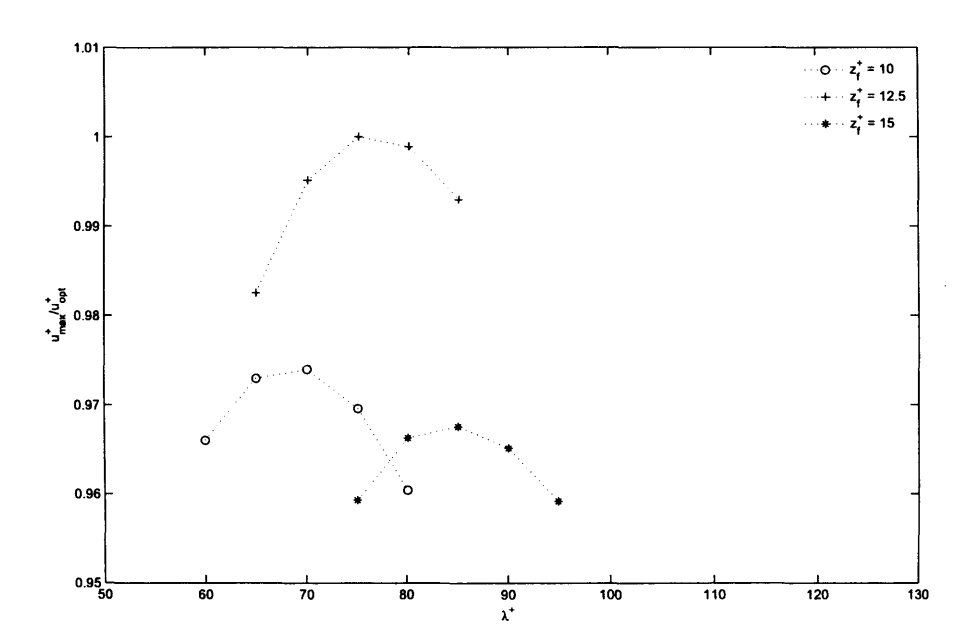


Figure 5.4: Relative streak magnitude for Gaussian perturbation in ω_x at various heights and spanwise wavelengths, with k_x chosen such that the streamwise half-width of the Gaussian profile is $x_{hw}^+ = 15$

As mentioned above, the results from figures 5.1 to 5.4 are normalised. This normalisation is performed for each value of k_x ; in other words, comparing the results from one graph to another doesn't tell us anything about the relative magnitude of the streaks for different values of k_x . In order to compare optimum streaks for different k_x values, it is useful to look at their histories i.e. how the maximum streak strength varies in time. This information is presented in figure 5.5.

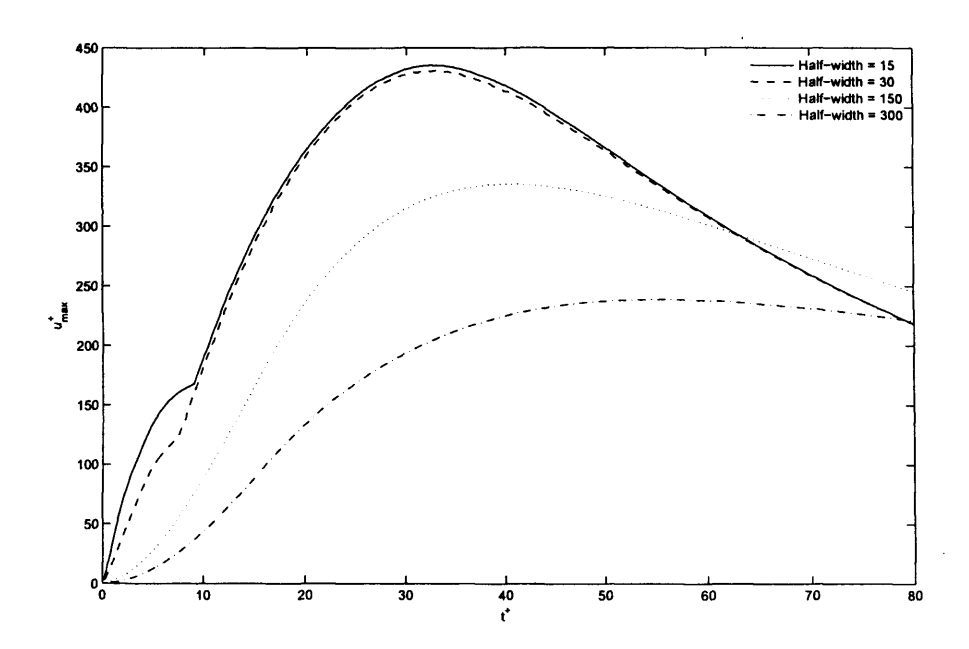


Figure 5.5: Time histories of the optimum streaks for a range of values of k_x .

Before discussing these results, though, we'll digress briefly to point out some details of how the forcing amplitude is scaled when changing the value of k_x , and why. If we integrate the forcing profile along the streamwise direction, we see that for smaller values of k_x (that is, a broader half-width) there will be a greater amount of force imparted in the creation of the streak. (Remember that although we speak of imparting a force through the forcing term of equation 5.1, it is more accurate to call F an imposed vorticity

source.) Using the fact that the integral of a one-dimensional Gaussian centred around an arbitrary point x_0 can be expressed as:

$$\int_{-\infty}^{\infty} A \exp\left(\frac{x - x_0}{c}\right)^2 dx = Ac\sqrt{\pi}$$
 (5.5)

It is possible to see that, by making sure that the magnitude of the forcing varies in direct proportion with $\sqrt{k_x}$, the same amount of force will be imparted for all values of k_x .

An examination of figure 5.5 tells us first that the narrower forcing profiles give us stronger streaks for the same normalised forcing magnitude. We also see that the maximum is reached earlier for narrower profiles. The streaks reach their maximum strength at the point where the exponential viscous decay begins to outweigh the algebraic inviscid growth. A later maximum therefore suggests either that the growth in the algebraic phase is stronger or more prolonged, or that the exponential decay is weaker. The gradients after the maximum are shallower in the $x_{hw} = 150$ and $x_{hw} = 300$ cases than in the $x_{hw} = 15$ and $x_{hw} = 30$ cases, indicating that there is weaker exponential decay in the broader forcing cases. The growth of these cases is also significantly shallower, which indicates that the algebraic growth is also weaker; it may also be more prolonged, and this, in combination with the weaker decay, is a possible explanation for the later maxima of the large x_{hw} .

As mentioned above, the optimum streak found for the $x_{hw}^+ = 15$ case is indistinguishable from the $x_{hw}^+ = 7.5$ case. Calculating the streak development for narrower forcing profiles has similar results, in that no significant change in the streak development is observed. This suggests that we have found, as was posited earlier, a value of x_{hw} below which all streak forcings produce identical results. We can tentatively say, then, that for $x_{hw}^+ \leq 15$ the fine details of the forcing are unimportant and we can use this as a satisfactory model of real disturbances. However, see section 5.2 below on the influence of changing the time variation of the forcing profile for more discussion of this point.

Figures 5.6 to 5.8 show the development of this optimum streak over a relatively long

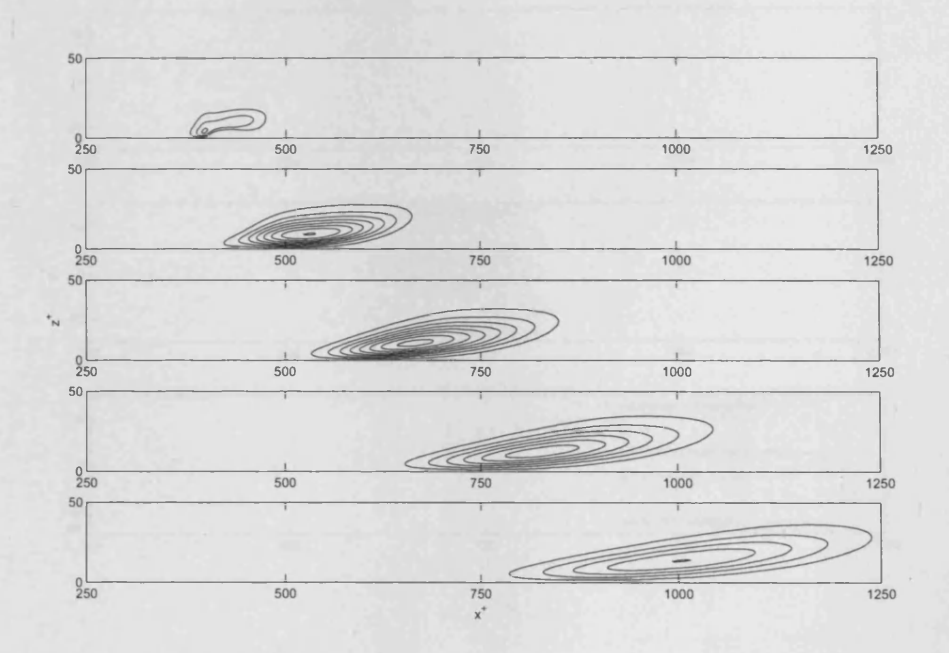


Figure 5.6: Contour plots of u_x^+ for the optimum streak with $x_{hw}^+ = 15$. Profiles are shown at times $t^+ = 8, 24, 40, 56, 72$ from top to bottom. Contours are at intervals of $u^+ = 50$.

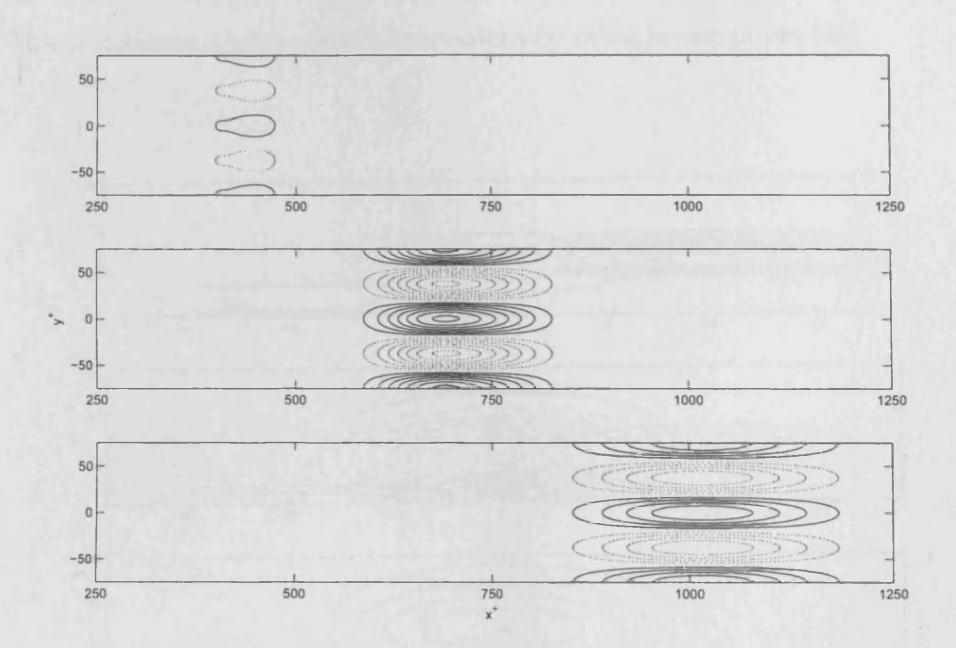


Figure 5.7: Contour plots of u_x^+ for the optimum streak with $x_{hw}^+ = 15$. Plans are shown at times $t^+ = 8, 40, 72$ from top to bottom. Contours are at intervals of $u^+ = 50$, with positive values represented by solid lines and negative values by dotted lines. Data taken from a wall-normal location $z^+ = 15$

period, illustrating the streak during both the growth and the decay. It is apparent from figures 5.6 and 5.7 that the streak very quickly attains a streamwise length scale of around 200 and lengthens to around 400 over the course of its development. This is large in comparison with the spanwise scale (specified by the choice of wavenumber, $\lambda^+ = 75$) and the wall-normal scale, and the streak remains within 50 wall units of the wall for all times. Note also the tilted appearance of the streak, with the leading edge lifting away from the wall. This is consistent with earlier observations by other investigators [48].

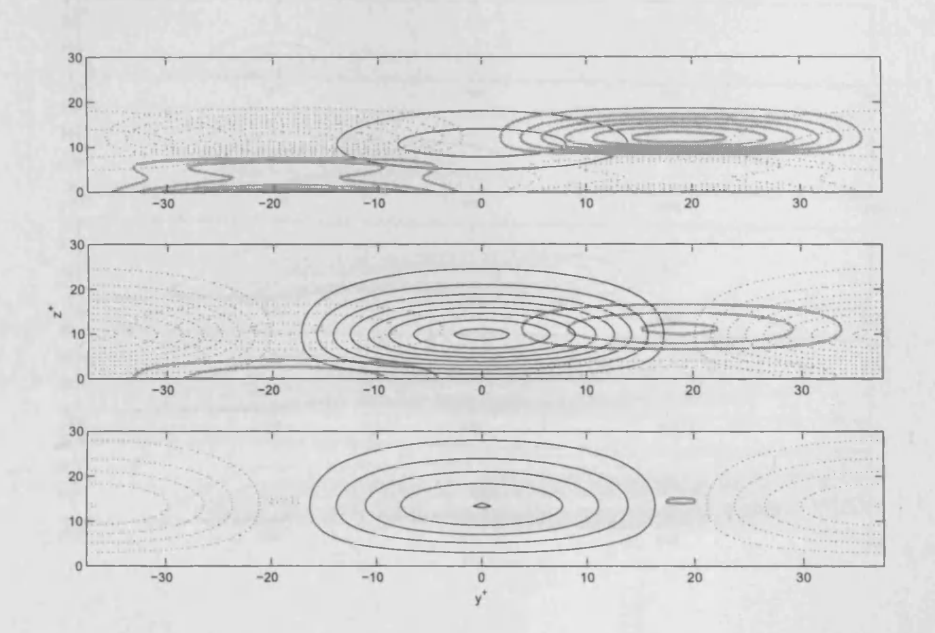


Figure 5.8: Contour plots of u_x^+ and ω_x^+ for the optimum streak with $x_{hw}^+ = 15$. Profiles are shown at times $t^+ = 8, 40, 72$ from top to bottom. Thin black lines are u_x^+ , thick grey lines are ω_x^+ . Contours are at intervals of $u_x^+ = 50$ and $\omega_x^+ = 5$. with positive values represented by solid lines and negative values by dotted lines. Data are taken from different streamwise locations for each frame; from top to bottom, data are shown at $x^+ = 450,650,1000$.

Another interesting feature is visible in figure 5.8, which shows the perturbation streamwise vorticity as well as the perturbation streamwise velocity. We see that the vorticity

decays much faster than the velocity, and in fact decays during the growth phase of the streak. It is important to bear in mind that the vorticity shown in this figure does not represent the quasi-streamwise vortices, which occur above the streaks in real turbulent boundary layers (as discussed in section 1.2); indeed, these vortices are not truly present in our calculations. This is one of the abstractions that our model incorporates, in an attempt to isolate the streaks from other turbulent boundary layer structures and phenomena.

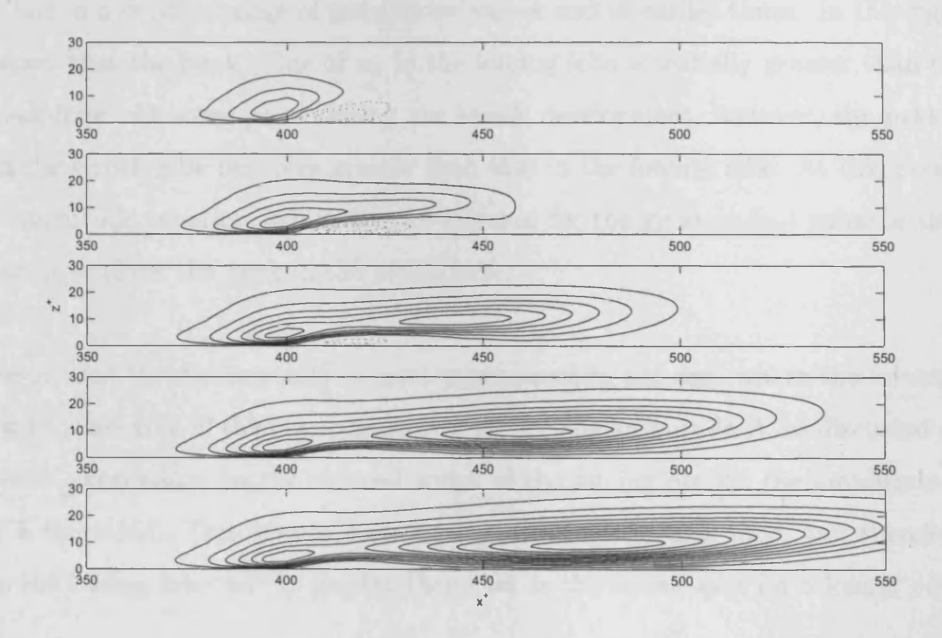


Figure 5.9: Contour plots of u_x^+ for the optimum streak with streamwise forcing half-width of 15 in wall units. Profiles are shown at times $t^+ = 3, 6, 9, 12, 15$ from top to bottom. Contours are at intervals of $u^+ = 25$, with positive contours solid and negative contours dotted. The zero contour is unmarked.

Returning briefly to figure 5.5, we note the kink that can be seen in the half-width 15 and 30 cases during the growth phase, around $t^+ \approx 8$. This initially seems quite mysterious, but there is a relatively simple explanation, which is well illustrated in figures 5.6 and 5.9.

The explanation for the streak magnitude discontinuities in figure 5.5 is illustrated in the first frame of figure 5.6, where the streak has a two-lobed structure. The longer lobe which is further downstream is the streak itself at an early stage of development; the more compact lobe further upstream is an artefact of the forcing and thus not indicative of any real streak physics, since we are using the forcing as a low-order approximation to the non-linear streak formation process (cf. the work of Landahl [46]). A more detailed examination of this two-lobed structure is presented in figure 5.9, where we see the same streak, but in a smaller range of streamwise values and at earlier times. In this figure, it is apparent that the peak value of u_x in the forcing lobe is initially greater than that in the streak lobe. At some point during the streak development, however, the peak value of u_x in the streak lobe becomes greater than that in the forcing lobe. At this point, our streak magnitude criterion, which simply searches for the greatest $|u_x|$ value in the flow field, starts to track the peak in the streak lobe.

The reason that the discontinuity is more pronounced in the case where the forcing half-width is 15 is because of the normalisation of the forcing amplitude A, as discussed above. In order to compensate for the reduced width of the forcing profile, the amplitude of the forcing is increased. This creates a stronger peak in the forcing lobe, and therefore the peak in the forcing lobe will be greater than that in the streak lobe for a longer period of time.

This also suggests an explanation for why no such discontinuity appears in the cases where x_{hw} is much larger. In these cases, the normalisation of the forcing amplitude to a lower value means that the peak value of velocity in the streak becomes much greater than the peak value in the forcing lobe almost immediately. Additional evidence for this explanation is seen in the profiles of the optimum streak for the case where the forcing half-width is 300, as depicted in figure 5.10. No forcing peak equivalent to that observed in the first part of figure 5.6 is visible. In fact, profiles at the same early times as those depicted in figure 5.9 (not included here) also show no forcing lobe, indicating that the

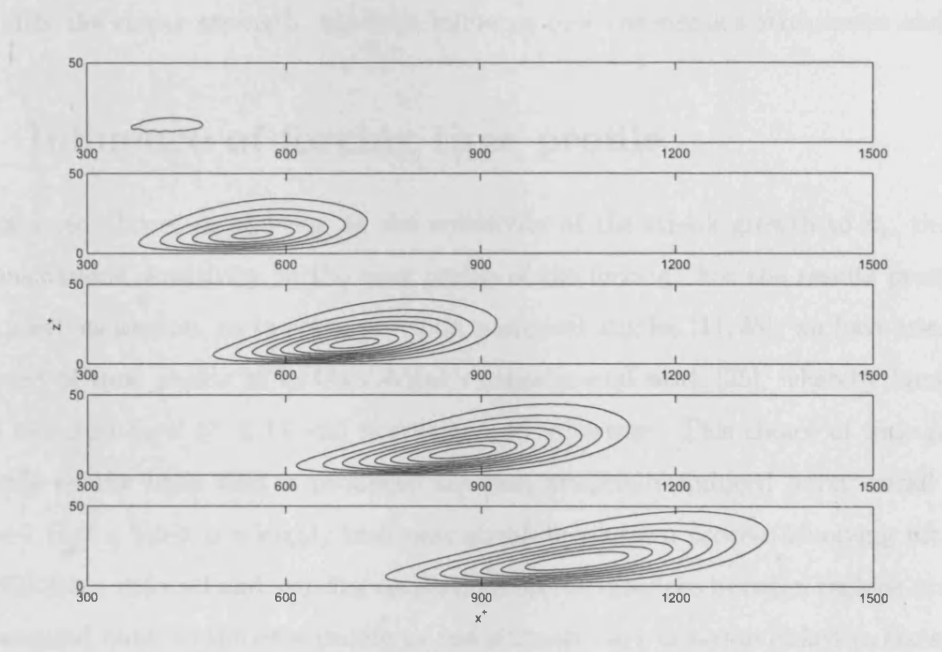


Figure 5.10: Contour plots of u_x^+ for the optimum streak with streamwise forcing half-width of 300 in wall units. Profiles are shown at times $t^+ = 8, 24, 40, 56, 72$ from top to bottom. Contours are at intervals of $u^+ = 25$.



streak is the dominant feature throughout. Note too that, although the streamwise length scale of the streak in figure 5.10 is somewhat longer than that in figure 5.6, the length scale of the streak during the growth phase (around 250 wall units) is much shorter than the length scale of the forcing (600, twice the half-width) and certainly has not increased by the same factor that the forcing length scale has. This suggests that there is a natural streak length scale determined by the basis flow, and the nature of the forcing, although it can alter the streak strength, has little influence over the streak's streamwise scale.

5.2 Influence of forcing time profile

As mentioned above, in addition to the sensitivity of the streak growth to k_x , there is also considerable sensitivity to the time profile of the forcing. For the results presented in the previous section, as in some previous numerical studies [11,48], we have used the same kind of time profile as in Gad-el-Hak's experimental work [25], whereby forcing is simply switched on if $t^+ < 15$ and is switched off otherwise. This choice of time profile was made on the basis that it produced the best artificially induced burst; recall from chapter 1 that a burst is a highly nonlinear streak breakdown process involving liftup of the streak from the wall and growing oscillations on the interface between regions of high-and low-speed fluid, so the time profile we use is chosen on a criterion linked to the streak strength, albeit indirectly.

As discussed above, our results indicated that there exists an x_{hw} limit below which the details of the forcing are unimportant, with the exception that at very small spatial scales viscous dissipation comes to dominate the dynamics. Thus, we say that this is a limit of sensitivity to spatial scales associated with the basis flow, since if the streak development is not affected by the details of the forcing below this limit, it must be determined by the basis flow only. We wish to find if there is, similarly, a limit of sensitivity to temporal scales for the forcing.

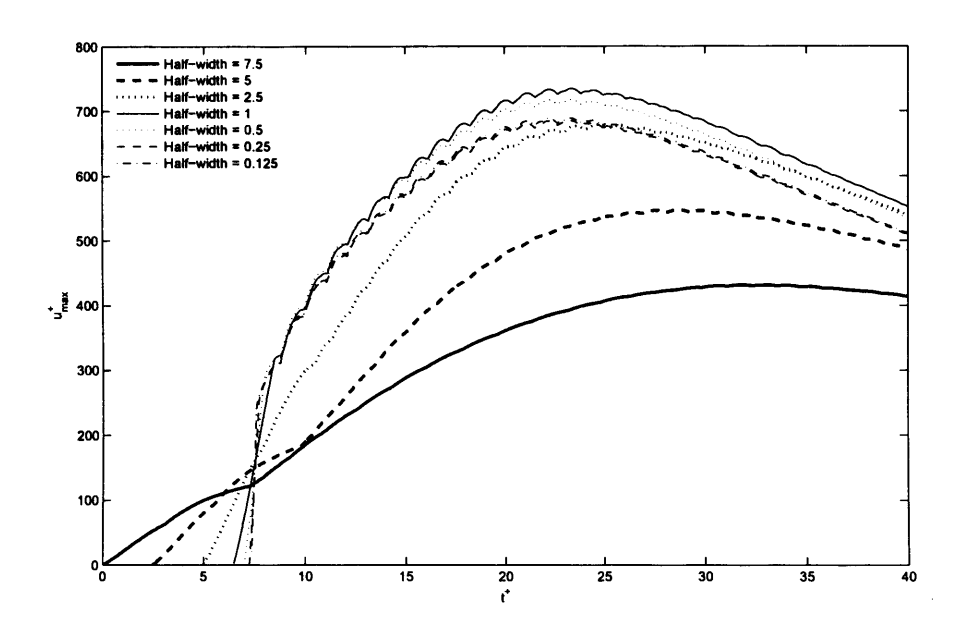


Figure 5.11: Development of streak magnitude in time for the streak with $z_f^+ = 12.5$, $\lambda^+ = 75$ and k_x based on a streamwise half-width of 15 wall units. Different plots show different values of t_{hw} .

Initially, we performed this investigation by simply shortening the length of time for which the forcing was switched on. The Heaviside-like nature of the forcing profile in time was retained. As in the investigation of the streak development's dependence on the spatial variation of the forcing, the technique used was to make the time profile more pointlike. Specifically, if we imagine the initial time forcing profile as an approximation to a delta function centred around $t^+ = 7.5$, then we can make the forcing more like a delta function by reducing the time interval between this centre and the switching on or off. Thus, just as with the variation of k_x to determine the spatial dependency of the streaks on the forcing, the temporal dependency of the streaks on the forcing can be parametrised entirely by a half-width, t_{hw} . For the original time forcing profile, this half width is 7.5 in wall units. Note that as the half-width is reduced, we need to introduce a correction to the amplitude of the forcing to account for its reduced duration, as was done when investigating the influence of k_x . The amplitude correction is simpler here; recalling that t_{hw} of our original profile can be expressed as $t_o^+ = 7.5$, the factor by which we need to correct the amplitude is simply $t_{hw}^+/7.5$.

The results of this investigation are shown in figure 5.11. We see that there is not a clear convergence; at first as the time half-width is reduced the streak reaches a greater maximum earlier in time, but that this trend is reversed for half-widths below 1. A possible explanation for this behaviour is that the use of a Heaviside-like forcing profile means that we have created essentially infinite gradients in time at the switch-on and switch-off. This is not something that the discretisation scheme can handle gracefully, and it becomes more significant as the duration of the forcing decreases since the switching necessarily occurs over the duration of a single time-step. A more satisfactory method of making the time forcing profile more like delta-like is to choose a function with a smoother profile. The smoothed time profile used is similar to the Heaviside-like forcing profile in that it is centred around a time $t_f^+ = 7.5$ and in that only a single parameter (t_{hw} , the time half-width) is needed to distinguish the different forcing profiles from one another. There is, again, an adjustment made to the amplitude of the forcing in order to compensate for

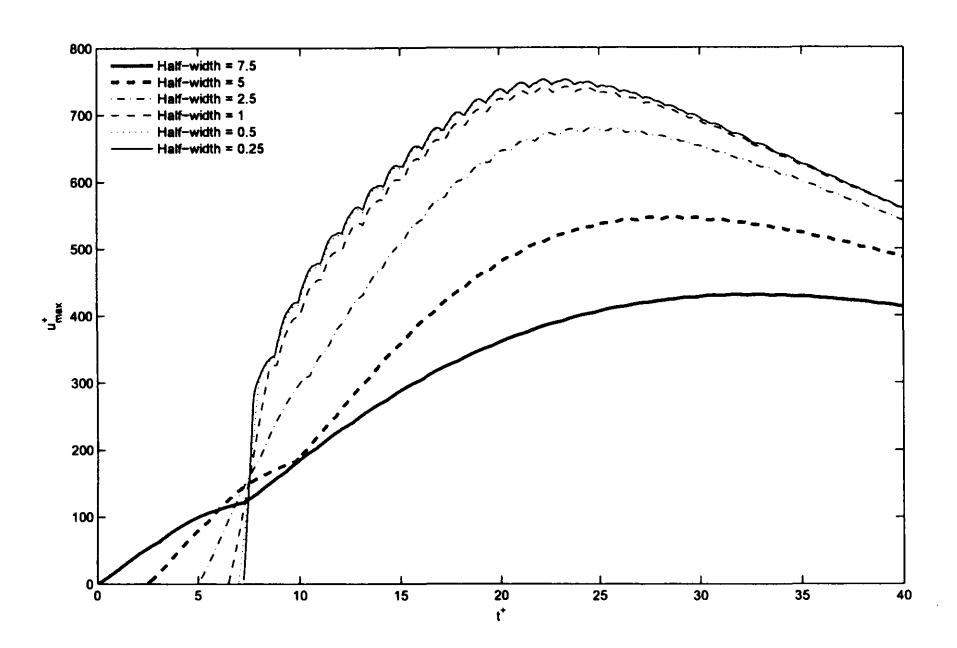


Figure 5.12: Development of streak magnitude in time for the streak with $z_f^+ = 12.5$, $\lambda^+ = 75$ and k_x based on a streamwise half-width of 15 wall units. Different plots show different values of t_{hw} .

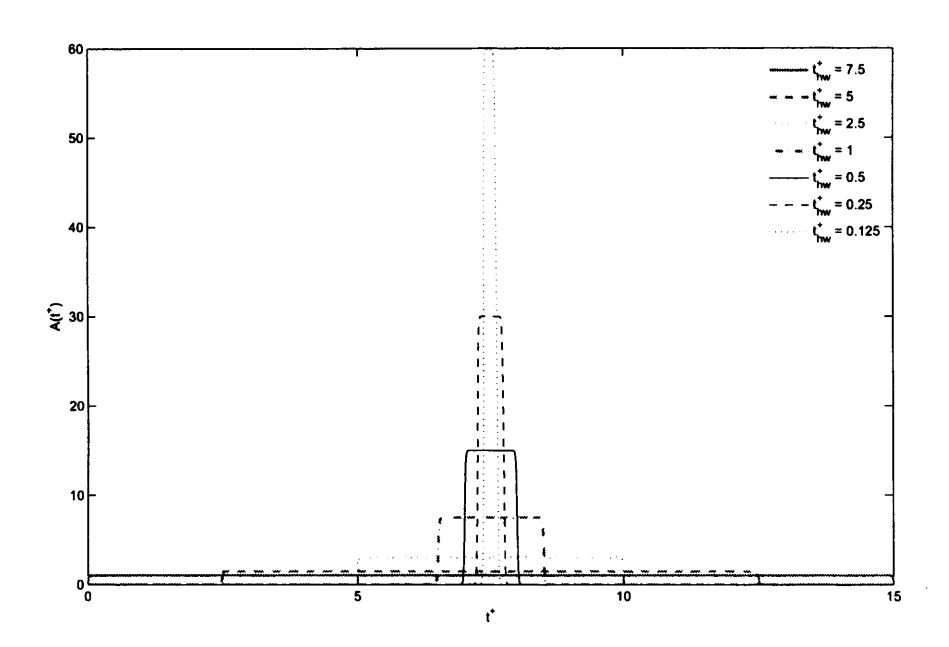


Figure 5.13: Selection of smoothed time profiles A(t) of streak forcing (equation 5.1) for different values of t_{hw}^+ . Magnitude is expressed as multiples of maximum magnitude in $t_{hw}^+ = 7.5$ case.

changes in its duration. The switching on and off was made smoother by defining A(t) from equation 5.1 as an appropriately chosen sum of tanh functions, of the form:

$$A(t) = \frac{1}{2} \left[\tanh(\sigma_t [t^+ - (t_f^+ - t_{hw}^+)]) + \tanh(\sigma_t [(t_f^+ - t_{hw}^+) - t^+]) \right]$$
 (5.6)

Where σ_t is a factor that controls the smoothness of the switch-on and -off. It is chosen such that the switching is fast enough to maintain a plateau-like form with the smallest t_{hw} , but still sufficiently resolved when using a reasonable timestep. A selection of these time profiles is depicted in figure 5.13, and the results from using them are presented in figure 5.12. We see that these results are similar to the case with the abrupt switching (see figure 5.11), but that here there is convergence, with the streak development effectively converging for time half-widths of $t_{hw}^+ = 0.5$ and below. However, there is a complication. Having discovered what seems to be a natural time scale of the basis flow, in that the details of the forcing on time scales smaller than $t^+ \approx 1$ don't affect the gross development of the streak, we find that the relative streak strengths have changed i.e. we have a new optimum streak. The new optimum is illustrated in figure 5.14 and shown to be at $z_f^+ = 10$, $\lambda^+ = 45$. This is no longer in the range of streak spacings observed experimentally by Zacksenhouse [82]; bear in mind, as mentioned earlier, that this is an optimum with respect to the particular streak magnitude criterion we have employed, .

Furthermore, the new apparent optimum streak is found to be once more sensitive to changes in k_x . Although the results presented in section 5.1 seemed to indicate that the overall course of streak development is not affected by the spatial details of the forcing if $x_{hw}^+ < 15$, we now find that after reducing the duration of the streak forcing to what seems to be its natural scale, further reductions of x_{hw} result once again in significant changes to the streak development. This is illustrated in figure 5.15, where we see that even with $x_{hw}^+ < 2$, the streak development is still changing as the streamwise half-width is reduced. The computational cost of simulating streaks initiated by a forcing of smaller streamwise length becomes prohibitive as the size of the elements required to adequately resolve the profile becomes smaller, so no further simulations were performed. It seems,

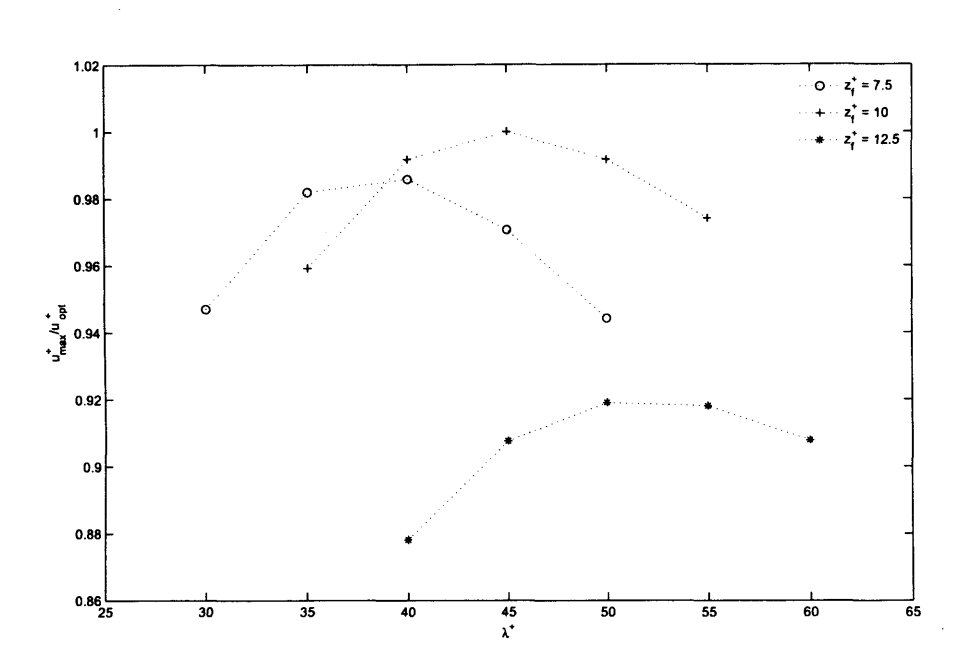


Figure 5.14: Relative streak magnitude for Gaussian perturbation in ω_x at various heights and spanwise wavelengths, with k_x chosen such that the streamwise half-width of the Gaussian profile is $x^+=15$. A smoothed forcing time profile is employed, with $t_{hw}=0.5$

however, that the natural length and time scales for the forcing surmised earlier to be inherent to the basis flow are not so straightforward.

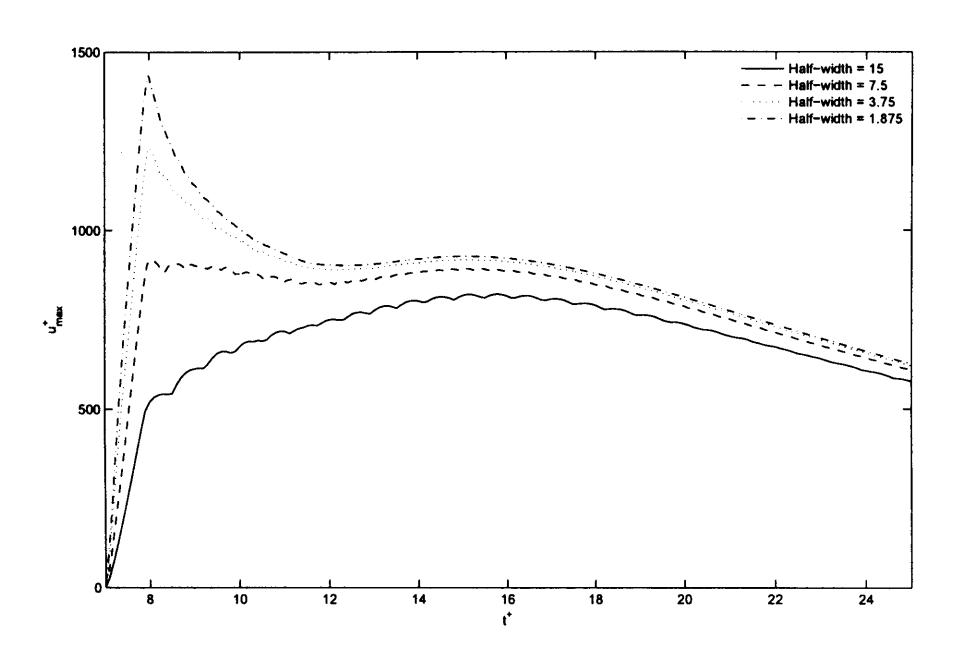


Figure 5.15: Development of streak magnitude in time for the streak with $z_f^+ = 10$, $\lambda^+ = 45$. Different graphs show the response for different forcing durations, as characterised by spatial half-width, x_{hw}^+ . All time profiles use a smoothed switching, with $t_{hw}^+ = 0.5$.

Our first investigation of the influence of k_x on the streak indicated that for half-widths below $x_{hw}^+ = 15$, the streak that developed in response to the introduction of the forcing did not substantially change if x_{hw}^+ was altered. We therefore regarded $x_{hw}^+ = 15$ as a cutoff point, below which the basis flow was insensitive to finer details of the forcing (although it seems likely that for very small x_{hw}^+ , the viscous diffusion associated with large spatial gradients might begin to make itself more strongly felt). A similar analysis seemed to apply to the temporal half-width, with $t_{hw}^+ = 0.5$ being the sensitivity cutoff, as illustrated in figure 5.14. Recall, however, that we found the $x_{hw}^+ = 15$ cutoff with a

fixed time profile, characterised by $t_{hw}^+ = 7.5$; the results described above show that if we change t_{hw}^+ , the x_{hw}^+ -value of the sensitivity cutoff changes. We now find something similar for the time profile: if x_{hw}^+ , previously held constant, is changed, the sensitivity cutoff value of t_{hw}^+ also changes; this is shown in figure 5.16, where we show the effects of changing t_{hw}^+ with $x_{hw}^+ = 1.875$, and we see that the streak response alters for different t_{hw}^+ values below the previously surmised sensitivity cutoff of $t_{hw}^+ = 0.5$.

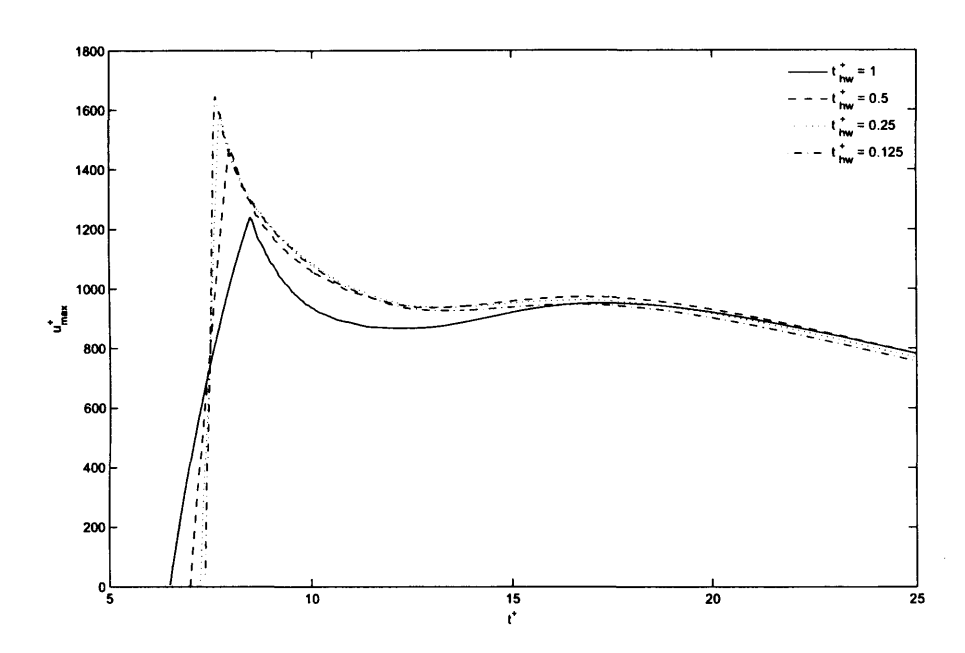


Figure 5.16: Development of streak magnitude in time for the streak with $z_f^+ = 10$, $\lambda^+ = 45$ and k_x based on a streamwise half-width of 1.875 wall units. Different plots show different values of t_{hw} .

Although these results are not conclusive, they are strongly suggestive: they seem to show that the sensitivity cutoff values of x_{hw}^+ and t_{hw}^+ are not inherent in the basis flow. Only if we fix t_{hw}^+ is there a cutoff value for x_{hw}^+ , and vice versa. It appears, then, that the basis flow doesn't specify the sensitivity cutoff values per se, but rather the relationship be-

tween them. It is difficult to see how the details of this relationship might be determined more precisely.

The conclusion we can draw from this is that the use of a pointlike forcing to generate streaks in problems such as these does not in and of itself adequately model the processes that generate streaks in real boundary layers. Making use of empirical data to specify some parameters of the forcing, as has been done heretofore, seems necessary to ensure that our streak generation process resembles the real process in its relevant aspects.

5.3 Influence of Reynolds number

In common with previously published results (see, for instance, Carpenter *et al.* [11]), we find that the Reynolds number has little effect on the optimum spanwise spacing of the streaks. Recall that the results presented above were obtained with a Reynolds number of 10000; figures 5.17 and 5.18 show the relative streak magnitudes in the vicinity of the optimum streak when the Reynolds number is decreased or increased by a factor of 10.

The optimum streak from the cases shown doesn't change with Reynolds number, and a finer-grained search for the optimum streak did not find a change in the optimum spanwise spacing either. The work of Cossu *et al.*, who used an energy criterion to measure streak magnitude, also indicated that the influence of the Reynolds number on the λ_{opt}^+ is negligible, or at least very small [19].

We also find, as expected, that the streak magnitude scales on inner units, which change as the Reynolds number is altered. Consider that the streak forcing, as given in equation 5.1, has units of vorticity per time. Thus, for the amplitude of the forcing in the different Reynolds number cases to be equivalent, we need the amplitude of the forcing, multiplied by the square of an appropriate inner time scale, to be the same across the board. An appropriate scale is given by the ratio $\delta^{*+}/U_{\infty}^{+}$. Thus, we expect the streak histories at

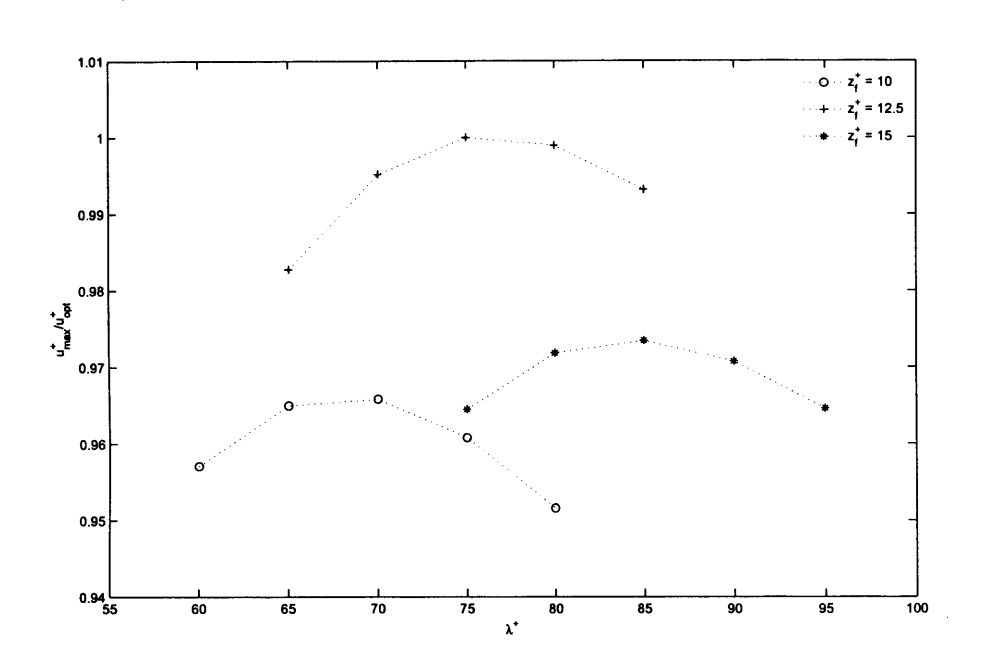


Figure 5.17: Streak magnitude for Gaussian perturbation in ω_x at various heights and spanwise wavelengths, with k_x chosen such that the streamwise half-width of the Gaussian profile is $x^+=15$. $Re=10^3$

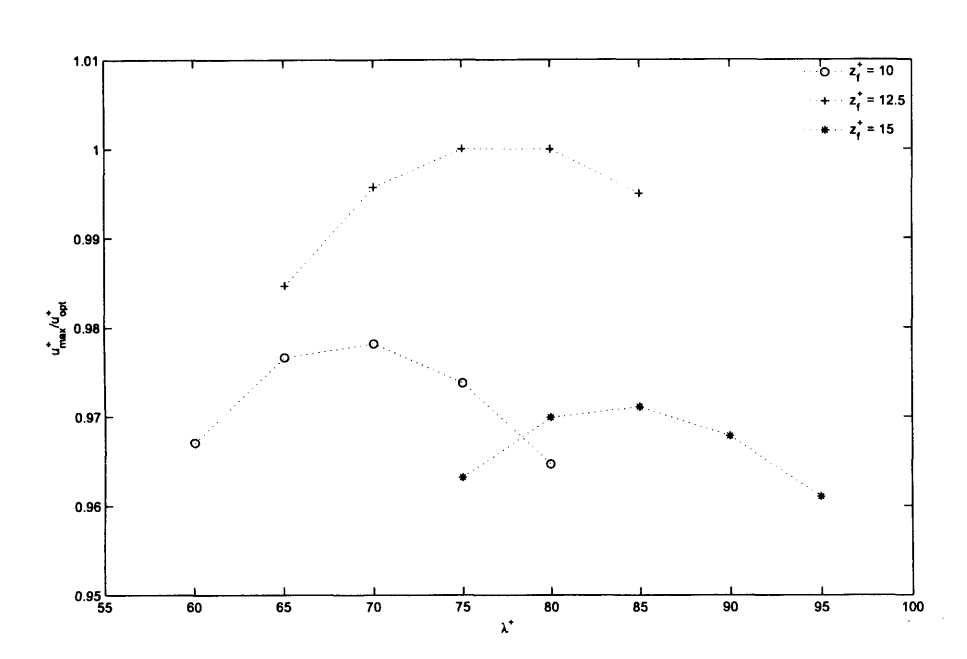


Figure 5.18: Streak magnitude for Gaussian perturbation in ω_x at various heights and spanwise wavelengths, with k_x chosen such that the streamwise half-width of the Gaussian profile is $x^+ = 15$. $Re = 10^5$

different Reynolds numbers to collapse (at least approximately) on to a single line when normalised by this quantity. This is borne out in figure 5.19. On the main graph the collapse appears exact, but the inset shows that there are minor differences in the details of the streak development; thus we have not simply performed the same simulation three times with different linear scalings, but have demonstrated that our solver genuinely demonstrates the streak inner scaling also observed in other investigations.

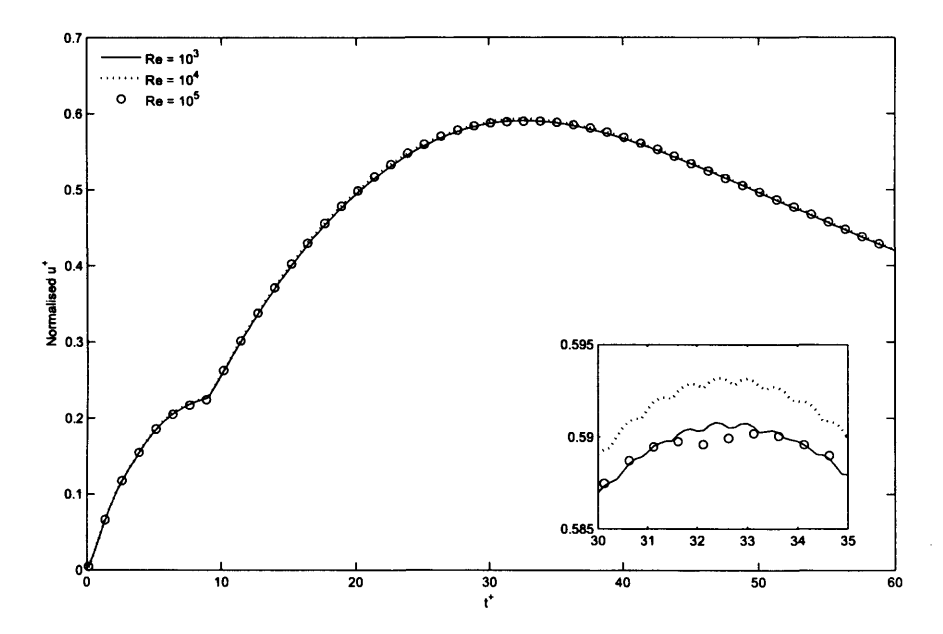


Figure 5.19: Development of streak magnitude in time for the streak with $z_f^+ = 12.5$ and $\lambda^+ = 75$. Different plots show different values of Re. Streak magnitudes are normalised as described above. Inset shows a detail of the peak values.

Chapter 6

Spanwise forcing

6.1 Implementation and initial case

In addition to using our solver to investigate the streaks themselves, we are also interested in seeing how spanwise forcing influences the development of the optimum streak. Since we found that in our formulation, the simplified forcing used to generate the streaks appears not to have a straightforward natural scale, as discussed in section 5.2, we are forced to make a choice of parameters for the streak-generating force, and thus also, albeit indirectly, a choice of optimum streak characteristics. We will choose parameters that bring in some empirical data, by implementing the same time profile that was used initially i.e., the simple Heaviside-like forcing suggested by the work of Gad-el-Hak et al. [25]. For the spatial extent of the forcing, we use $x_{hw}^+ = 15$, which was found to give us the optimum streak of figure 5.4, with $\lambda^+ = 75$ the spanwise spacing.

In order to investigate the effects of wall forcing on the streaks, we will use the secondary perturbation formulation described in section 2.1.3. This, in essence, involves solving the governing equations twice: once to calculate the effects of introducing wall forcing and to create a new secondary basis, and then again to model the streak development on this new basis. Note that, since we are still dealing with streaks, which have

been observed to scale on wall units, we shall continue to use wall units throughout this chapter, unless specifically noted. On a similar note, we shall continue to focus on the flow with $Re_{\delta^*} = 10^4$.

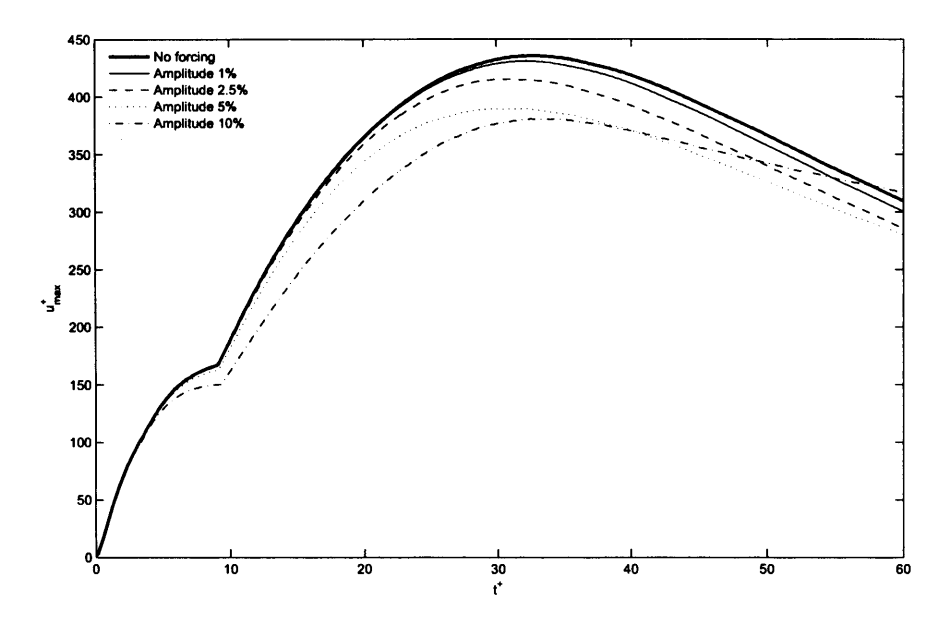


Figure 6.1: Development of streak magnitude in time for the optimum streak for a range of spanwise wall oscillation magnitudes. $T^+=250$. $\phi=0$ in all cases

The first results we present use a simple, sinusoidal-in-time wall oscillation, the same type that produces a Stokes layer. Our solver's ability to accurately capture a Stokes layer is discussed in section 4.3. We investigate in the first section the effects of altering the amplitude of the oscillation and the phase of the streak forcing with respect to the wall oscillation. The oscillatory velocity of the wall is specified by our choice of \hat{u}_y in equation 2.30. Recall that in our formulation, velocities are normalised by the freestream velocity, so we express the oscillation amplitude as a percentage of this value. For example, if we choose \hat{u}_y such that it is a sinusoidal oscillation with maximum value 0.01, we call this an amplitude of 1%. This corresponds to a peak wall velocity of 0.27 in wall units. The phase is of relevance because, for many of the calculations we have performed, the time

over which the streak develops is short with respect to the oscillatory period. The phase angle ϕ is defined in terms of the wall frequency, and expresses how much of the oscillation has elapsed between the nominal start of the cycle (arbitrarily designated as the point in time where the wall velocity reaches a positive-valued maximum) and the switching-on of the streak forcing. Values of ϕ separated by exactly π were found to produce identical results (unsurprisingly, since this produces the same oscillation in the opposite direction) so we investigate only phase angles in the range $0 \le \phi < \pi$. Figure 6.2 shows representative examples of the Stokes layers at a selection of phase angles: these profiles are obtained with an oscillatory amplitude of 1%, and may simply be scaled linearly to get the corresponding profiles for different amplitude. The spanwise forcing is not uniform in the streamwise direction; instead, the wall near the inlet is stationary and the wall begins oscillating at the streamwise location $x = L_s$. This is sketched in figure 4.6, and the exact formulation of the streamwise variation is given by equation 4.9.

Our canonical case uses a frequency (note that it is expressed in wall units) of $\gamma^+ = \pi/125$, giving a period of $T^+ = 250$. Since our formulation uses zero initial conditions, we thought it sensible to adopt the following procedure for our simulations. The amplitude is ramped up smoothly from zero to its desired value over the first half-period of the wall oscillation, and the streak forcing is then switched on at the start of the next oscillation, or slightly later if we wish to introduce a phase difference. A test run confirmed that there was no appreciable difference between the secondary basis flow at the end of the first oscillation (that is, the one including the half-period ramp-up) and the end of the second, thus assuring us that any transience associated with the ramp-up was negligible by the time of the earliest streak forcing switch-on. This means we avoid unphysical transients that might distort the effect of the wall oscillation on the streak development. Similar studies performed by other investigators have also found that the temporal transients associated with switching-on a transverse wall oscillation last no more than a single period even if the switching is sudden; see for instance the study of Quadrio and Ricco, which focusses specifically on such transience [60].

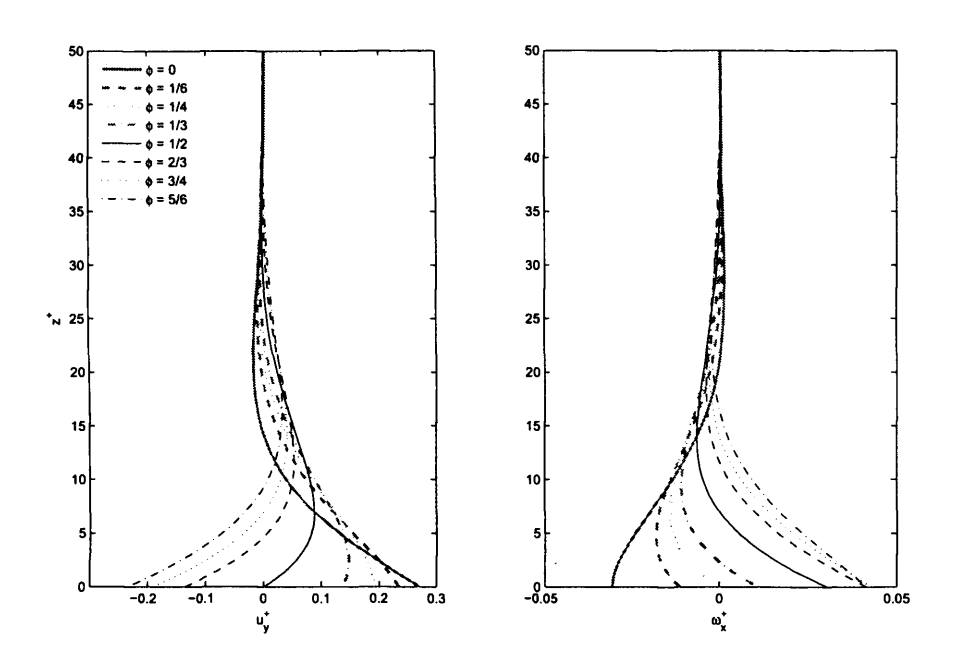


Figure 6.2: Illustrative examples of the u_y^+ and ω_x^+ wall-normal distributions for a Stokes layer with a wall oscillation amplitude of 1%. Different plots show different phase angles; the phase angles shown are the same as those used to define different start times for the streak forcing in figure 6.3. The plots presented here therefore represent idealised (streamwise uniform) versions of the secondary basis flow at the instant the streak forcing is turned on for the various cases shown in the first frame of figure 6.3.

Interestingly, in performing the calculations for the secondary basis flow driven by the wall oscillation, we can see that, due to the imposition of spanwise uniformity (i.e., setting $\beta = 0$) and the parallelisation of the primary basis flow, the streamwise VTE is decoupled from the spanwise VTE and the Poisson equation for u_z . We can see this if we substitute $\beta = 0$ into the equations 2.14 to 2.16, which gives the equations:

$$\begin{split} \frac{\partial \omega_x}{\partial t} + U_B \frac{\partial \omega_x}{\partial x} &= U_B' \omega_z + \frac{\Delta \omega_x}{Re} \\ \frac{\partial \omega_y}{\partial t} + U_B \frac{\partial \omega_y}{\partial x} + U_B'' u_z &= \frac{\Delta \omega_y}{Re} \\ \Delta u_z &= -\frac{\partial \omega_y}{\partial x} \end{split}$$

We see that the only term in the streamwise VTE not involving ω_x is $U_B'\omega_z$, and spanwise uniformity means that ω_z is calculated from an integral relation involving only ω_x , as can be seen from the definition of the secondary variables (that is, those variables not calculated explicitly in our formulation, rather than those pertaining to the secondary perturbations) given in equation 2.12. Both the spanwise VTE and the Poisson equation for u_z involve only the variables ω_y and u_z , and thus, while they are coupled to one another, they are not influenced by ω_x . Furthermore, since the spanwise oscillation of the wall only forces the flow through the integral condition on ω_x , this means that when calculating our secondary basis, only the streamwise VTE needs to be solved; ω_y and u_z will remain identically zero at all times, and therefore do not need to be calculated.

Also worth noting is that, under the same circumstances of spanwise uniformity and parallelised basis flow, and with spanwise oscillation of the wall the only mode of excitation, the solution to the nonlinear equations 2.20 and 2.21 is identical to the solution from the linear equations. While the streamwise VTE is not formally decoupled from the spanwise VTE and the Poisson equation in this case, it is possible to see that, if we start with zero initial conditions, ω_y and u_z will once more remain identically zero for all

times. The key to this is firstly that the sum $\omega_x(\partial u_y/\partial x) + \omega_z(\partial u_y/\partial z)$ which appears on the right-hand side of equation 2.21 cancels exactly, since under spanwise uniformity $\omega_x = -\partial u_y/\partial z$ and $\omega_z = \partial u_y/\partial x$, and secondly that the secondary variable u_x is defined entirely by ω_y and u_z (per equation 2.12) and thus will remain identically zero if ω_y and u_z do.

Thus, the streamwise oscillation of the wall does not, in the absence of other forcing, influence the spanwise vorticity or wall-normal velocity, and all the nonlinear terms in the streamwise vorticity equation 2.20 are identically zero. The most important consequence of this is that we have shown our treatment of the secondary basis flow, for the cases we have investigated, to be fully equivalent to the nonlinear treatment.

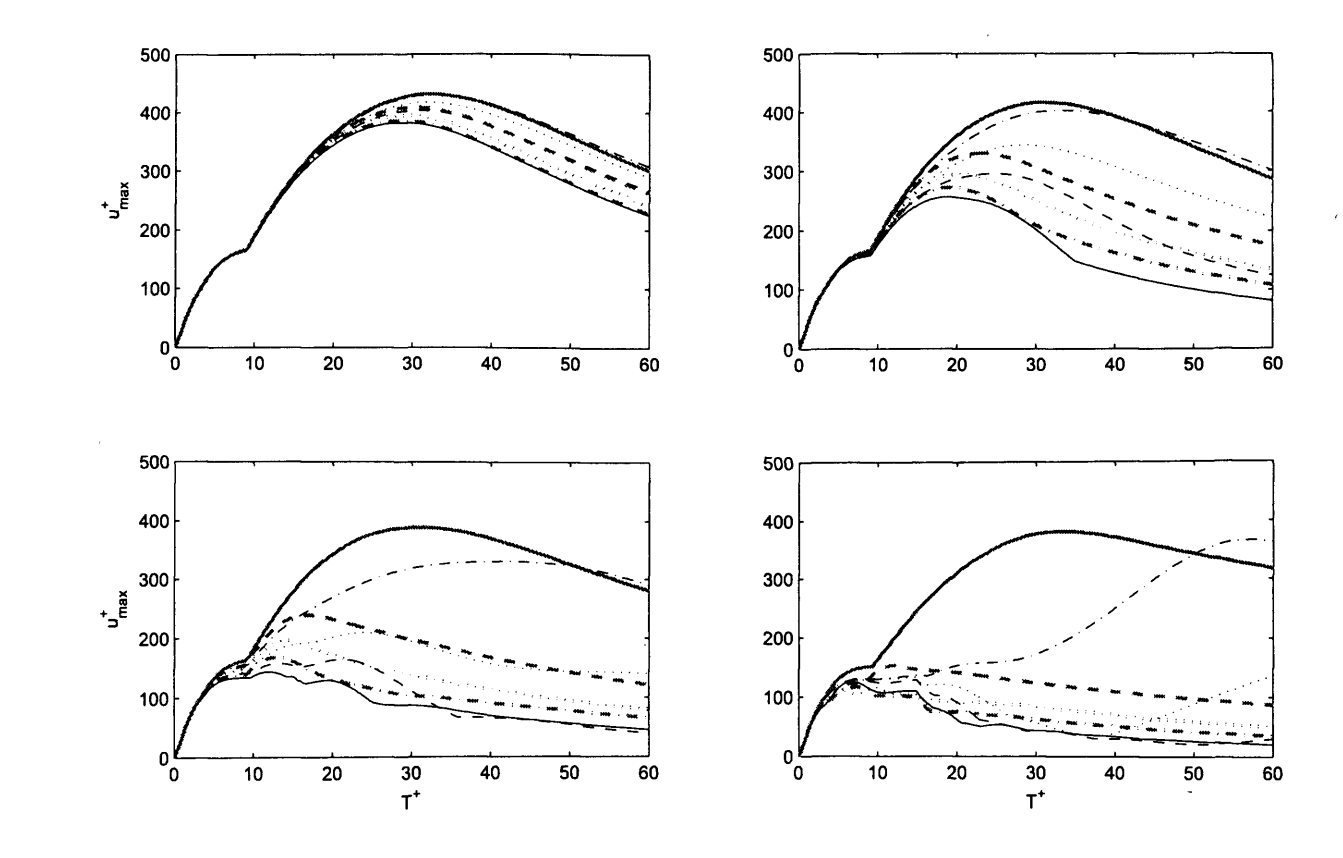


Figure 6.3: Development of streak magnitude in time for the streak with $\lambda^+=75$ for a variety of wall oscillations with $T^+=250$. Different frames show different forcing amplitudes. Clockwise from top left: amplitude 1%, amplitude 2.5%, amplitude 10%, amplitude 5%. Within each frame, different plots show different phases ϕ : solid grey $\phi=0$, dashed grey $\phi=\pi/6$, dotted grey $\phi=\pi/4$, dash-dotted grey $\phi=\pi/3$, solid black $\phi=\pi/2$, dashed black $\phi=2\pi/3$, dotted black $\phi=3\pi/4$, dash-dotted black $\phi=5\pi/6$.

Figure 6.1 shows the effects of spanwise wall oscillation amplitude on the development of streak magnitude in the canonical case with the phase difference ϕ set to zero. Figure 6.3 shows the effects of varying this phase difference for a range of amplitudes. The time for each simulation has been zeroed to the instant the forcing is switched on. We see that, particularly for larger forcing amplitudes, the effect of changing the phase angle is sometimes very dramatic, significantly more so than the effect of changing the amplitude in the $\phi = 0$ case seen in figure 6.1. For this case, we observe a reduction of maximum streak strength as the amplitude of the wall motion increases, but the development of the streak strength in time is qualitatively similar to the unforced case. Changing ϕ in the $A = 0.01U_{\infty}$ case similarly changes the maximum magnitude and time at which the maximum is attained, but the time development remains largely similar in form to the unforced cases. Changing ϕ in the $A=0.1U_{\infty}$ case, however, can drastically alter the course of streak development, as seen in the fourth frame of figure 6.3. The effect of changing phase angle with an oscillation amplitude that is intermediate between these two values is somewhere between the gradual adjustment as seen in the $A=0.01U_{\infty}$ case and the sharp changes seen in the $A = 0.1 U_{\infty}$ case, as is illustrated in the second and third frames of the same figure.

The massive change in the history of the streak magnitude as a result of a relatively small change in phase angle, such as that illustrated in figure 6.3 if ϕ is changed from 0 to $\pi/6$ in the 10% amplitude case, seems unusual. However, if we alter the phase in smaller increments (as seen in figure 6.4), we see that there is in some sense a smooth change to this drastically reduced streak magnitude, which gives us confidence in the validity of our results.

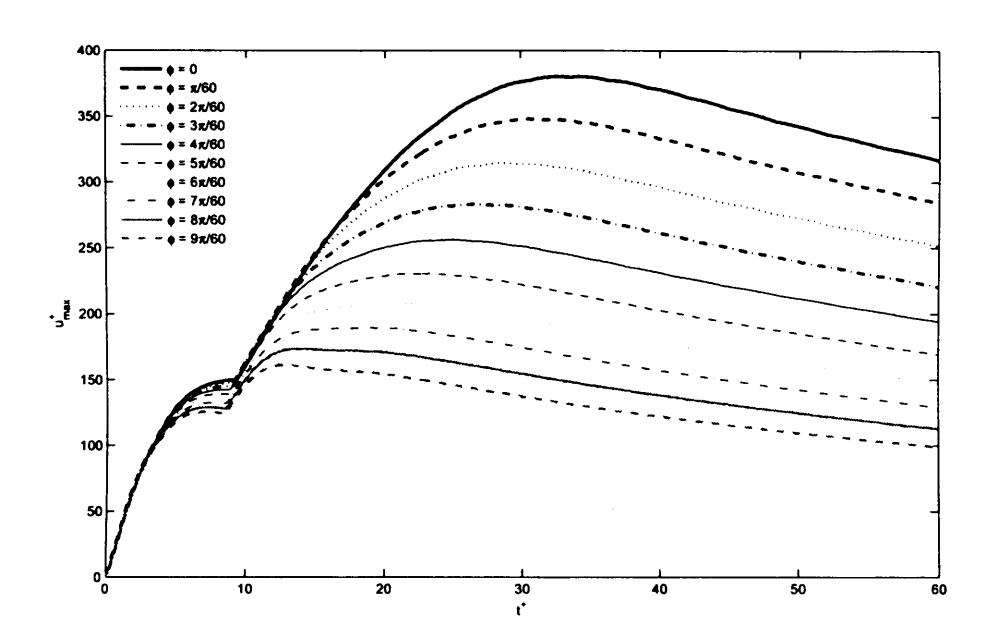


Figure 6.4: Development of streak magnitude in time for the optimum streak, with a spanwise wall oscillation magnitude of 10% of freestream velocity. $T^+=250$. ϕ gives the phase of the wall oscillation at which the streak forcing is turned on. t^+ is zeroed to the switching on of the streak forcing in each case.

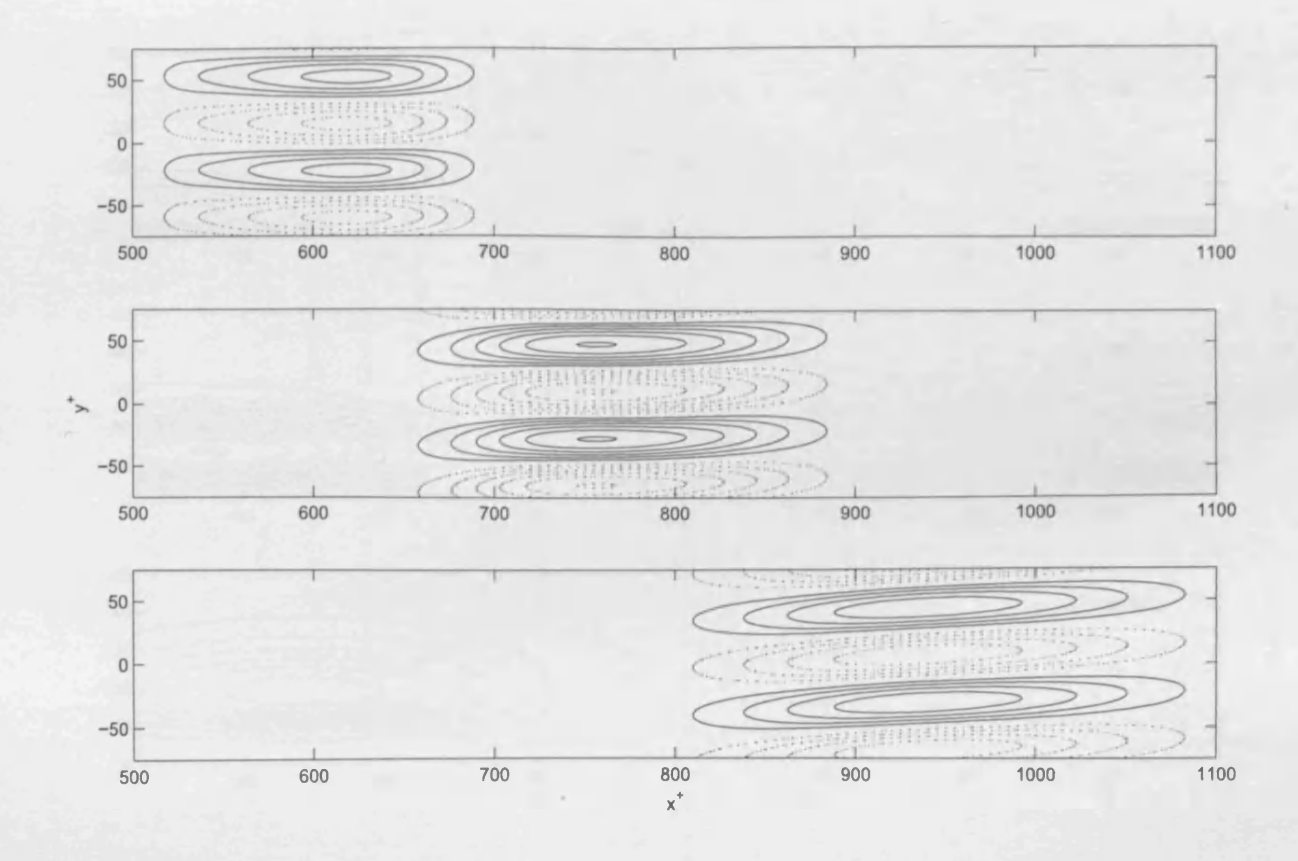


Figure 6.5: Contours of $Re(u_x^+)$ for optimum streak based on a half-width of 15 wall units, subject to a spanwise wall oscillation with magnitude 1% of freestream velocity and period $T^+ = 250$. $\phi = \pi/2$. Values are taken from a wall-normal location $z^+ = 15$. Contours are at intervals of 50, with positive contours solid and negative contours dashed. The zero contour is omitted. Values shown for times $t^+ = 18, 36, 54$ from top to bottom.

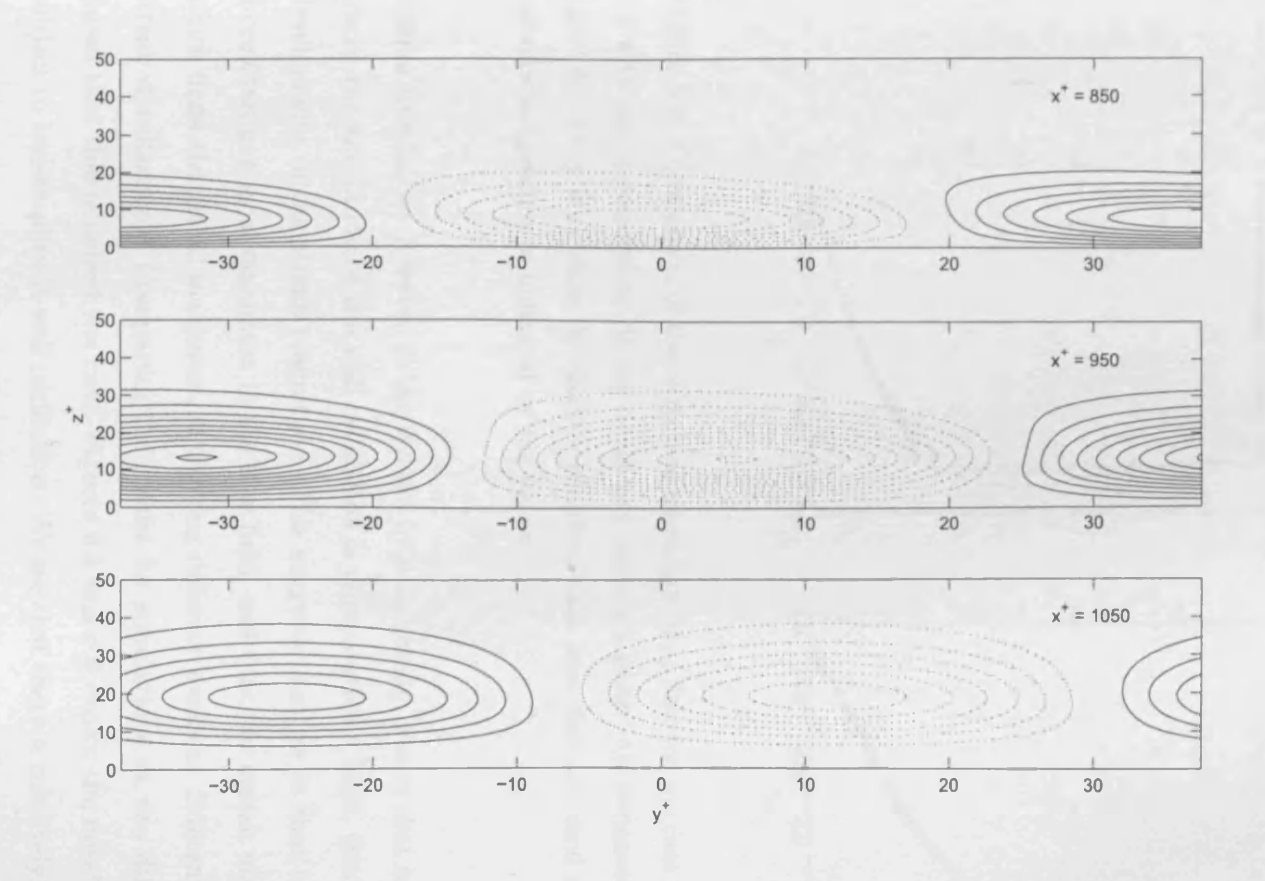


Figure 6.6: Contours of $Re(u_x^+)$ for optimum streak based on a half-width of 15 wall units, subject to a spanwise wall oscillation with magnitude 1% of freestream velocity and period $T^+ = 250$. $\phi = \pi/2$. Values are from time $t^+ = 54$ after switching-on of forcing, corresponding to the third frame of figure 6.5. Contours are at intervals of 25, with positive contours solid and negative contours dashed. The zero contour is omitted. Values shown for streamwise locations $x^+ = 850,950,1050$ from top to bottom.

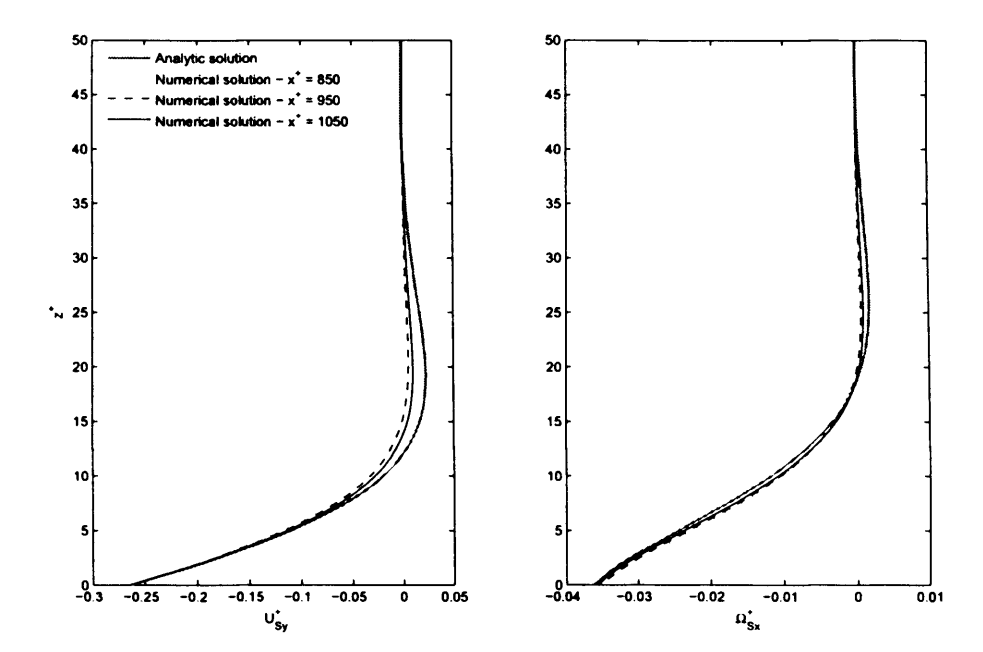


Figure 6.7: Comparison of the numerical secondary basis flow for the case illustrated in figure 6.6 with the corresponding Stokes oscillatory boundary layer. All parameters are as stated in figure 6.6. Grey lines show the analytic solution, black lines the numerical solution at different streamwise locations as indicated by the legend.

Similar to what we observed in the streaks with no forcing, we see that in some of the cases where the amplitude of the wall oscillation is comparatively high, there are kinks in the development of the streak magnitude. This suggests that, as in that case, there may be more than one local maximum in the flow field, and that our streak magnitude criterion, which finds the global maximum, is tracking different peaks at different times during the streak development. Comparing the results for simulations at two different amplitudes shows that this is indeed the case. Figures 6.5 and 6.6 depict the development of streaks subject to low-amplitude wall oscillation. We see that there is relatively little distortion of the streaks compared to the unforced case; they still appear fairly straight (although not perfectly aligned with the mean flow, as they are in the unforced case illustrated in figure

5.7) in a plan view and similar to the unforced streak in elevation. Also worth noting is the direction of tilt in the plane parallel to the wall (as shown in figure 6.6, where the first frame shows a cross-section of the streaks near the trailing edge and subsequent frames show cross-sections from further downstream): we see that the sense of the tilt is such that the trailing edge of the streak is more displaced in the instantaneous direction of the cross-flow wall motion. This is the expected result, since the trailing edge is closer to the wall and therefore should be more effected by its spanwise motion. Figure 6.7 confirms that the secondary basis flow on which the streaks are developing matches quite well with the Stokes oscillatory boundary layer.

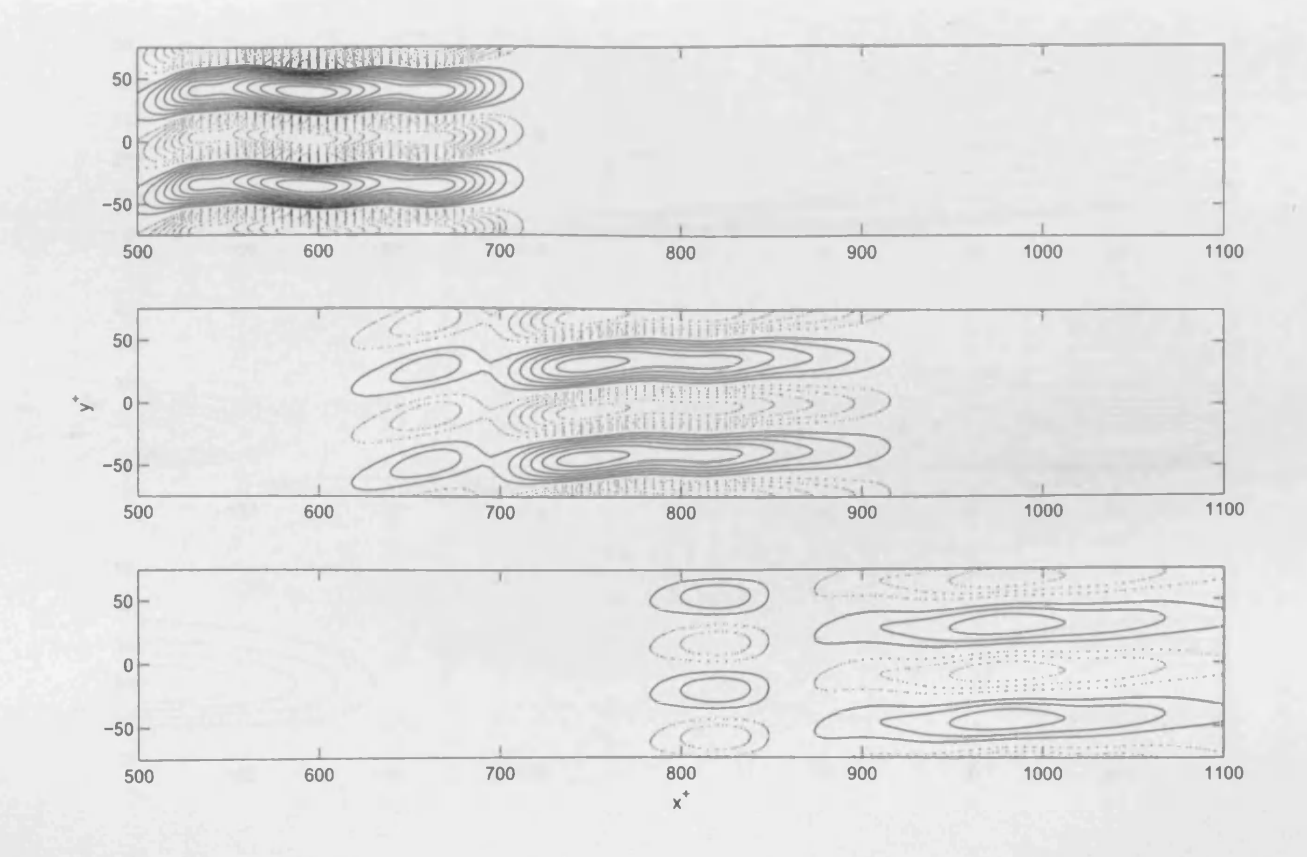


Figure 6.8: Contours of $Re(u_x^+)$ for optimum streak based on a half-width of 15 wall units, subject to a spanwise wall oscillation with magnitude 1% of freestream velocity and period $T^+ = 250$. $\phi = 2\pi/3$. Values are taken from a wall-normal location $z^+ = 15$. Contours are at intervals of 5, with positive contours solid and negative contours dashed. The zero contour is omitted. Values shown for times $t^+ = 18, 36, 54$ from top to bottom.

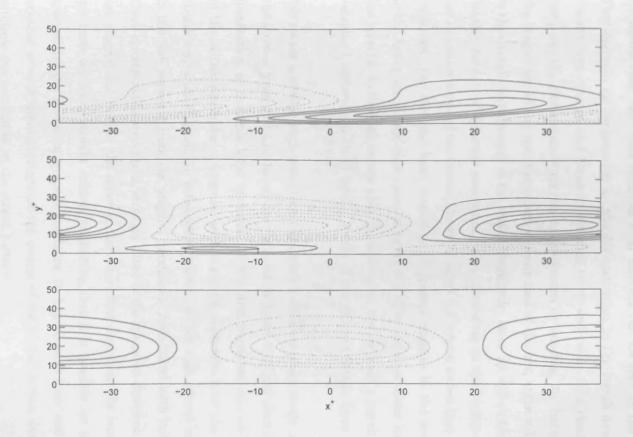


Figure 6.9: Contours of $Re(u_x^+)$ for optimum streak based on a half-width of 15 wall units, subject to a spanwise wall oscillation with magnitude 1% of freestream velocity and period $T^+ = 250$. $\phi = 2\pi/3$. Values are from time $t^+ = 36$ after switching-on of forcing, corresponding to the second frame of figure 6.5. Contours are at intervals of 5, with positive contours solid and negative contours dashed. The zero contour is omitted. Values shown for streamwise locations $x^+ = 700,800,900$ from top to bottom.

Comparing figure 6.8 with figure 6.6, we can see that the distortion of the streaks when subject to a large-amplitude wall oscillation is significantly greater than in the lower-amplitude case, and that multiple local extrema can be seen in the latter two frames. This suggests an explanation for the discontinuities in the streak development: if different extrema emerge and decay at different times and rates, then clearly one that was at one point the global maximum can be superseded by another. In this situation, as soon as the magnitude of the new extremum exceeds that of the old, there will be a discontinuity in the overall development of the streak magnitude, since we will suddenly be tracking the development of a different maximum. Also interesting in the higher-amplitude case are the elevation views of the streak, shown in figure 6.9, where we see that the larger spanwise velocities near the wall have caused much greater changes in the streak structure than in the lower amplitude case (seen in figure 6.5. The stronger shear has greatly distorted the streaks, to such an extent that the low-speed streaks have a patch of high-speed fluid entrained underneath them by the action of the induced Stokes layer, and vice versa.

We revisit a similar high-amplitude case, with a different phase angle, later in the chapter; the streaks from this simulation are depicted in figure 6.15 and perhaps provide a better illustration of multiple local maxima. In the first frame we can see that the structure of the streak resembles a tadpole, with a strong maximum near the leading end of the streak and a trailing tail. In subsequent frames, we see that a local maximum has arisen in the tail, separate from the original maximum. Associated with both of these maxima there are streaklike structures, strongly tilted in the spanwise direction. These two streaks are aligned one behind the other in the mean flow direction. At later times we can see yet more auxiliary streaks arising, suggesting that it is possible for the maximum being tracked by the streak magnitude condition to hop around from one local maximum to another several times throughout the course of the overall streak development, creating multiple discontinuities in the streak history.

It is not clear, however, exactly what mechanism causes the formation of these auxiliary

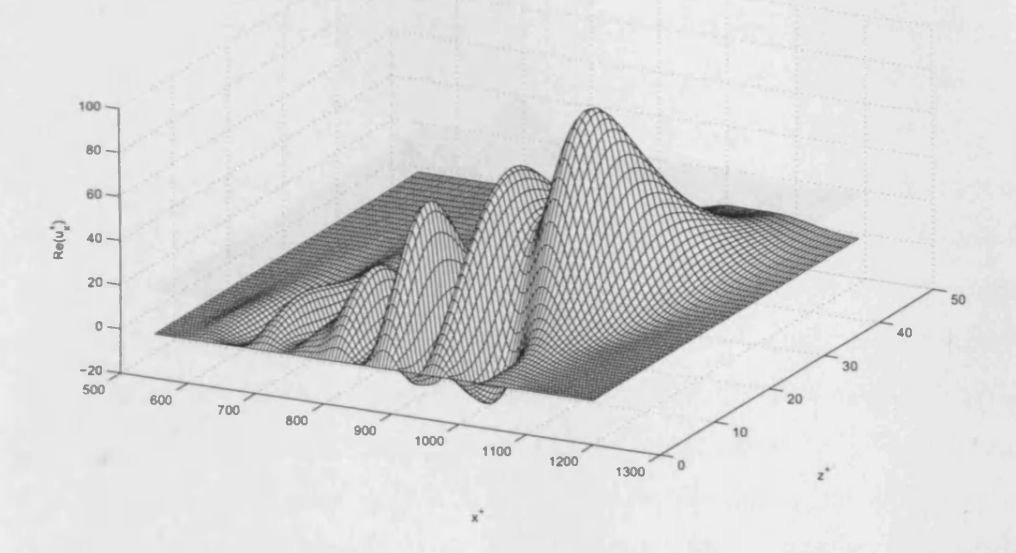


Figure 6.10: Surface plot of $Re(u_x^+)$ for optimum streak created by a forcing with a streamwise profile half-width of 15 wall units, subject to a wall oscillation of magnitude 10% of freestream velocity with $T^+=250$. Data taken from $t^+=54$. The phase lag between the wall oscillation and the switching-on of the streak forcing is $\phi=\pi/6$

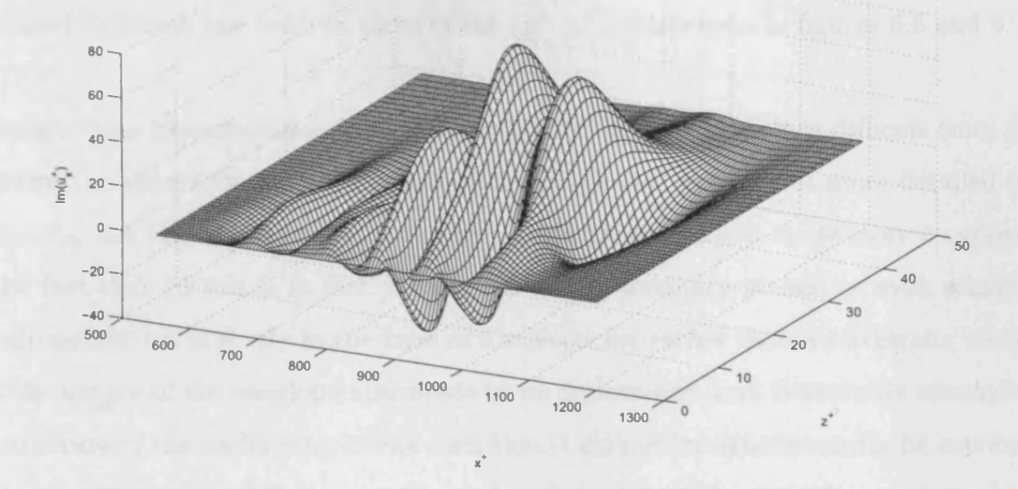


Figure 6.11: Surface plot of $Im(u_x^+)$ for optimum streak created by a forcing with a streamwise profile half-width of 15 wall units, subject to a wall oscillation of magnitude 10% of freestream velocity with $T^+=250$. Data taken from $t^+=54$. The phase lag between the wall oscillation and the switching-on of the streak forcing is $\phi=\pi/6$

streaks, or even whether it is accurate to talk about a single main streak with auxiliary structures. It may instead be that the appearance of several streaks is caused by the superimposition of a wavelike solution on a streak solution that more closely resembles that of the unforced case. In other words, the new basis flow created by the introduction of spanwise wall oscillation to the mean turbulent boundary layer profile might be more prone to unstable wavelike perturbations. An example of this type of solution is illustrated in figures 6.10 and 6.11, which show the real and imaginary parts of the streamwise perturbation velocity u_x^+ at time $t^+ = 54$ subject to a strong spanwise wall oscillation. These surface plots show the variation in the (x^+, z^+) -plane; data from similar simulations were used to create the contour plots of the (x^+, y^+) -plane seen in figures 6.8 and 6.15.

Although these perturbations seem to have a wavelike structure, it is difficult from these diagrams (or indeed from a more thorough investigation) to pick out more detailed characteristics: the amplitude and wavenumber, for instance. This is made more complicated by the fact that (if this is in fact a wave and not an auxiliary streak, or even something else altogether!) it is firstly in the form of a wavepacket rather than a wavetrain, meaning that the nature of the envelope also needs to be determined, and is secondly entangled in the structure of the underlying streak such that it cannot straightforwardly be extricated. For further discussion of the generation and growth of wavelike disturbances in spanwise-forced boundary layers, see section 6.3.

The linear formulation of the governing equations for the secondary perturbations means that there is unavoidably a degree of arbitrariness in the magnitude of the perturbations. However, the cases presented in this chapter are all based on the optimum streak of chapter 5 (except for the results presented in figure 6.37; see the end of section 6.4 for discussion of these), and all use a streak forcing with characteristic half-widths $x_{hw}^+ = 15$, $t_{hw}^+ = 7.5$. The scaling of the forcing amplitude with the parameter k_x (related to x_{hw} through equation 5.4) is discussed in section 5.1; none of the other parameters altered in our investigations influence this amplitude. Thus, since the streaks in all the results of this chapter were

generated using a forcing of the same k_x and therefore the same amplitude, the absolute magnitude of the flow variables as depicted in, for example, figures 6.5 and 6.8 can be meaningfully compared with one another and with the corresponding results from the optimum streak not subject to any wall oscillation, as depicted in figures 5.6, 5.7 and 5.8.

6.2 Frozen oscillation

Examining figure 6.3, it can be seen that the histories of the streak development for the cases $\phi = 2\pi/3, 3\pi/4$ and to a lesser extent $5\pi/6$ show an interesting behaviour: they appear, at late times when all other cases are decaying normally, to show the streaks entering a delayed growth phase. Figure 6.12 shows the development of the streaks with these phase angles over a longer time period, and compares it with the wall oscillation. Note that, unlike the previous graphs showing the streak magnitude histories, this graph does not zero time to the point at which the streak forcing is switched on. The data are shown in this way to see if, across the different phase offsets between the wall cycle and the streak forcing, there is commonality to the way the streaks develop at particular points in the wall oscillation cycle. Something of this sort is in fact what we see, with the delayed growth of the streaks in all cases beginning at around $t^+ = 380$. There is also a small blip of growth at a much later time of around $t^+ = 520$, just after half the oscillatory cycle has elapsed.

This suggests that there are particular parts of the wall oscillation cycle which are more conducive to promoting or preventing streak growth than others. In order to test this hypothesis, we ran a series of simulations similar to those performed already, making the modification that, as soon as the forcing that generates the streaks is switched on, we stop updating the basis flow. In other words, the secondary basis is frozen at the instant of switching on the force. In figures 6.13 and 6.14 we plot some of the results from these simulations.

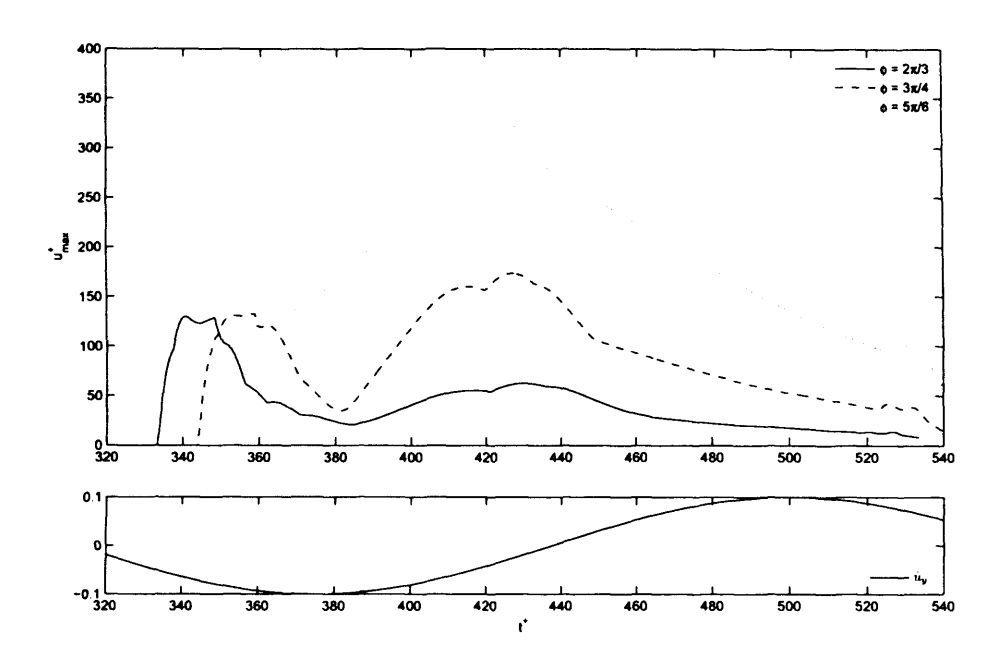


Figure 6.12: Development of streak magnitude in time for the optimum streak, with a spanwise wall oscillation magnitude of 10% of freestream velocity. $T^+ = 250$. Below the plot of the time development of the streak magnitude is a plot of the wall oscillation.

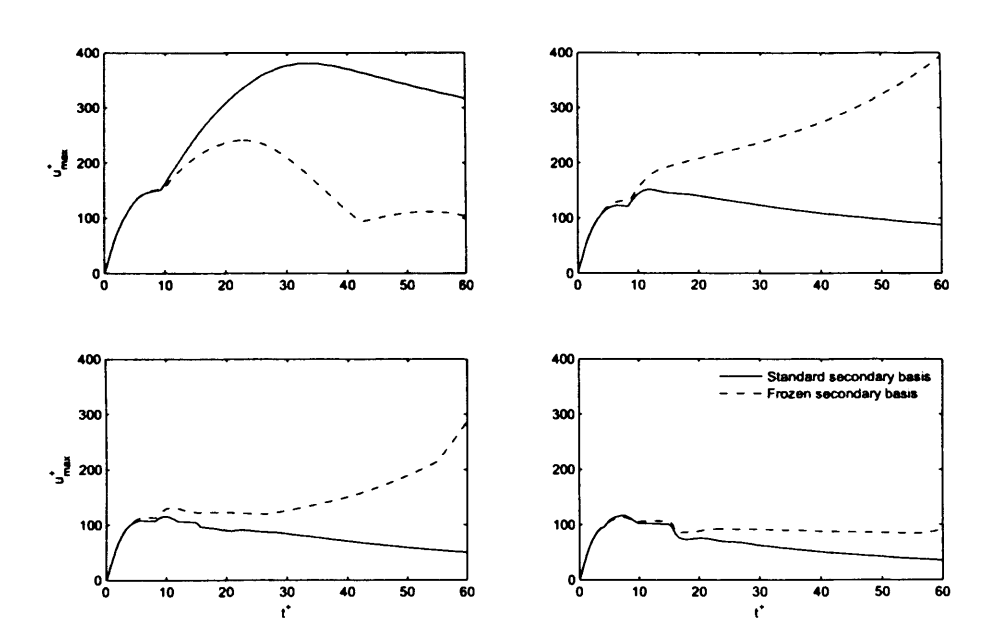


Figure 6.13: Development of streak magnitude in time for the optimum streak, with a spanwise wall oscillation magnitude of 10% of freestream velocity. $T^+=250$. Solid lines are as in the amplitude 10% frame of figure 6.3, dashed lines are the streak magnitude with the spanwise oscillation frozen at the moment streak forcing begins. Each graph depicts a different phase between the oscillation and beginning of streak forcing. Clockwise from top left: $\phi=0, \phi=\pi/6, \phi=\pi/3, \phi=\pi/4$.

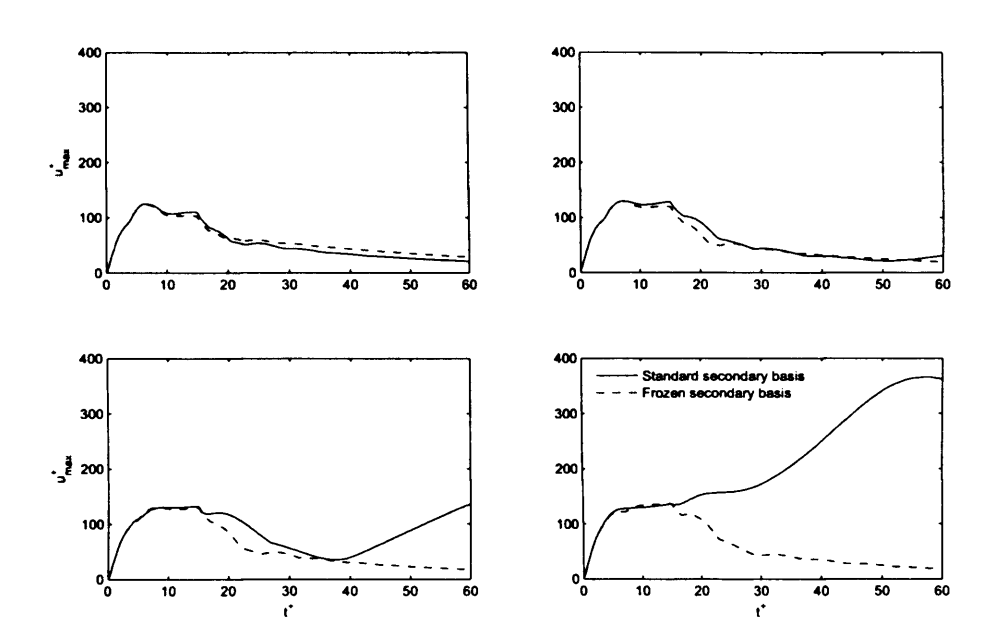


Figure 6.14: Development of streak magnitude in time for the optimum streak, with a spanwise wall oscillation magnitude of 10% of freestream velocity. $T^+=250$. Solid lines are as in the amplitude 10% frame of figure 6.3, dashed lines are the streak magnitude with the spanwise oscillation frozen at the moment streak forcing begins. Each graph depicts a different phase between the oscillation and beginning of streak forcing. Clockwise from top left: $\phi=\pi/2, \phi=2\pi/3, \phi=5\pi/6, \phi=3\pi/4$.

The results from these cases show that freezing the basis can either encourage or inhibit streak formation compared to the case where the oscillation continues, depending on the phase angle at which the streak forcing was switched on. Streaks develop to significantly greater magnitudes than in the physical case if the oscillation is frozen at $\phi = \pi/6$ or $\phi = \pi/4$, but their magnitude is greatly reduced in the $\phi = 3\pi/4$ and $\phi = 5\pi/6$ cases. If we can determine more precisely what qualities of the secondary basis flow at these phase angles cause the streak development to be altered in this way, it may be possible to tailor the wall oscillation profile to our requirements (i.e. promotion or amelioration of streaks), rather than only using the sinusoidal oscillation examined heretofore.

Also of interest is figure 6.16, which depicts the streaks in plan view for the case where the wall oscillation has been frozen at $\phi = \pi/4$. If we compare this to figure 6.15, we see that the effect of freezing the wall oscillation is to increase the spanwise tilt of the streaks. This is not unexpected, since the speed of the wall decreases if we are starting from a low value of ϕ . There are also fewer minima and maxima apparent. This could be simply due to the increase in the contour interval meaning the lower-magnitude extrema are no longer seen in the visualisation, or it could be due to the apparent increase in the streamwise spacing of the extrema. If we assume the presence of wavelike perturbations in these solutions, this corresponds to a larger wavenumber and therefore the appearance of fewer extrema within a wavepacket of the same streamwise extent.

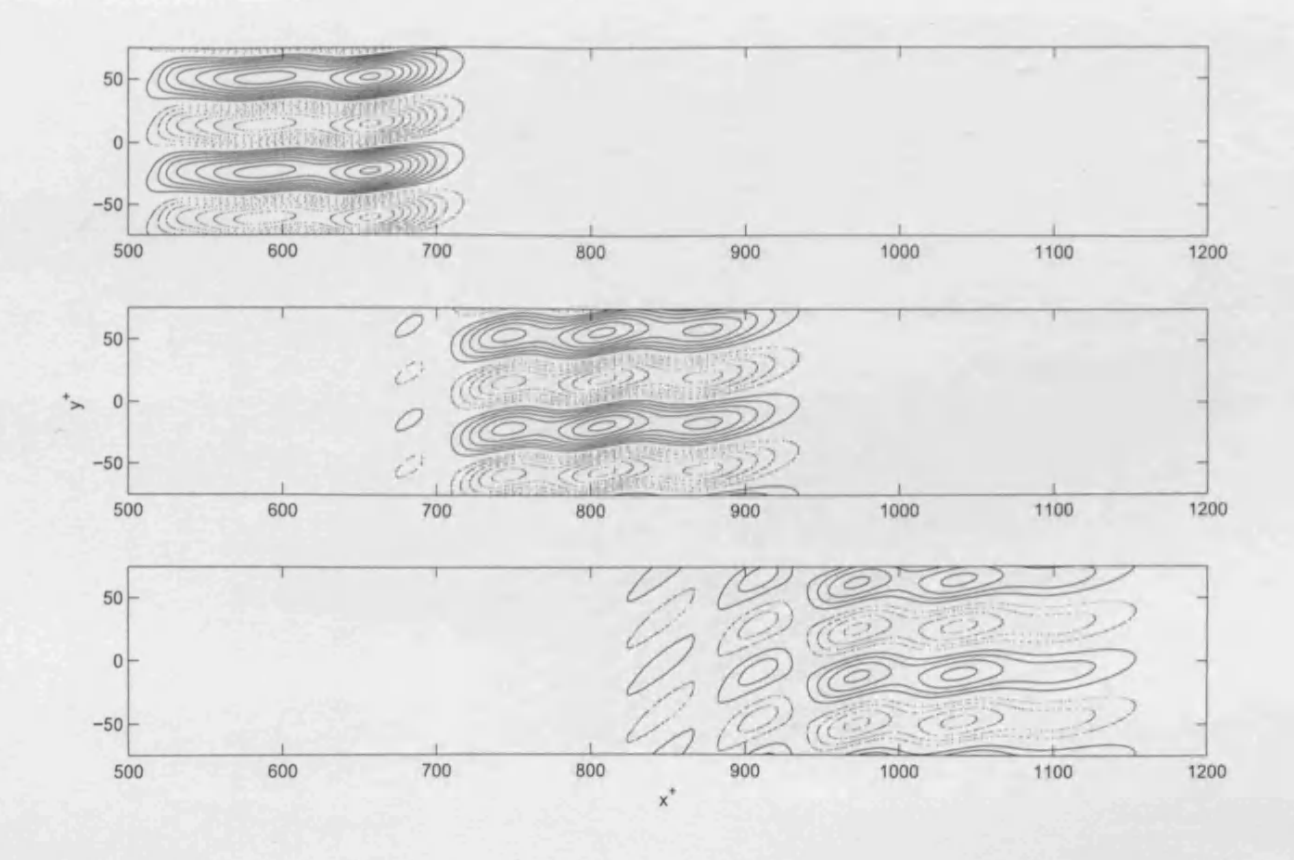


Figure 6.15: Contours of $Re(u_x^+)$ for optimum streak based on a half-width of 15 wall units, subject to a spanwise wall oscillation with magnitude 10% of freestream velocity and period $T^+ = 250$. $\phi = \pi/4$. Values are taken from a wall-normal location $z^+ = 15$. Contours are at intervals of 25, with positive contours solid and negative contours dashed. The zero contour is omitted. Values shown for times $t^+ = 18, 36, 54$ from top to bottom.

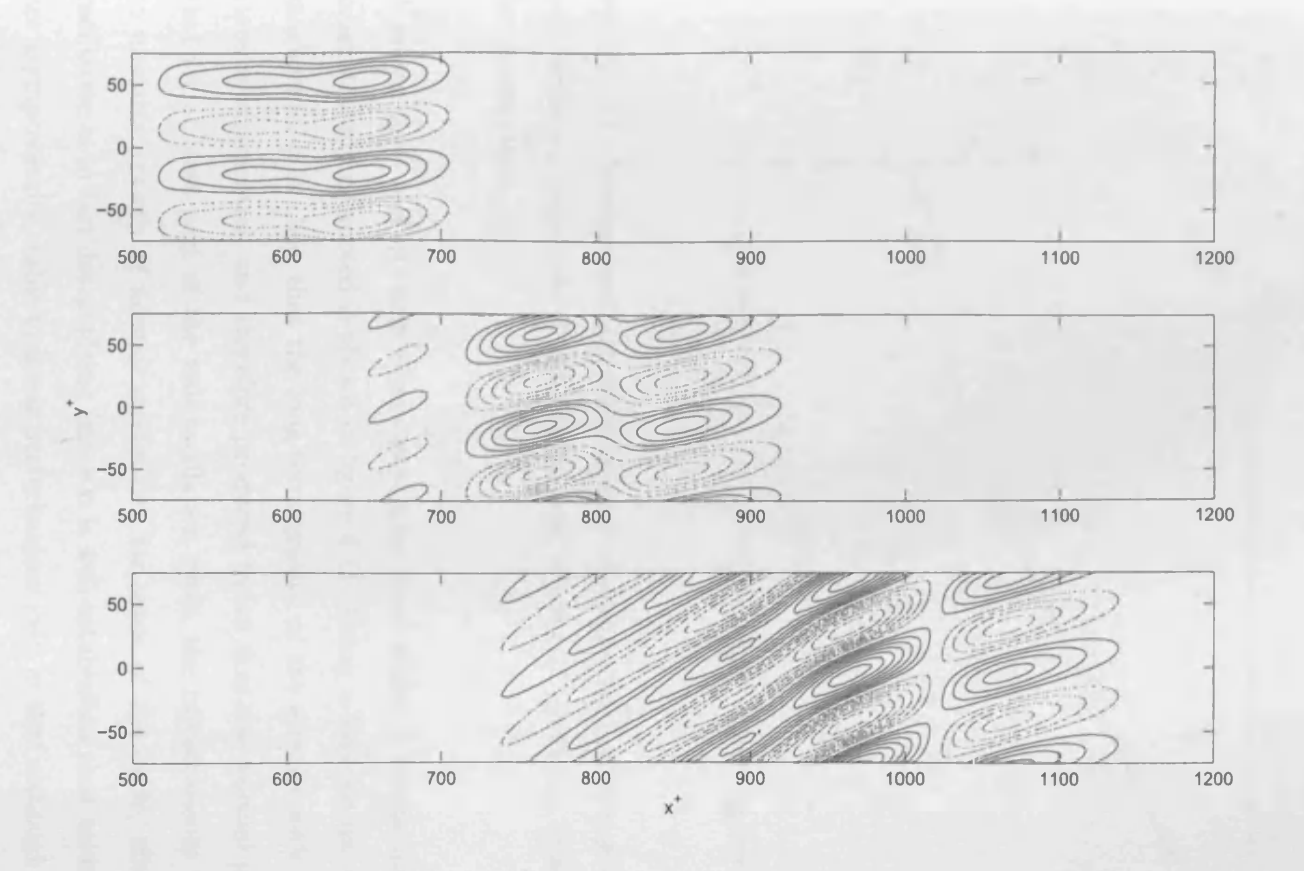


Figure 6.16: Contours of $Re(u_x^+)$ for optimum streak based on a half-width of 15 wall units, subject to a spanwise wall oscillation of magnitude 10% of freestream velocity with $T^+=250$ which is frozen at the instant the streak forcing is switched on. Values are from a wall-normal location $z^+=15$. Contours are at intervals of 50, with positive contours solid and negative contours dashed. The zero contour is omitted. $\phi = \pi/4$. Values shown for times $t^+=18,36,54$ from top to bottom.

6.3 Exponential growth of normal modes

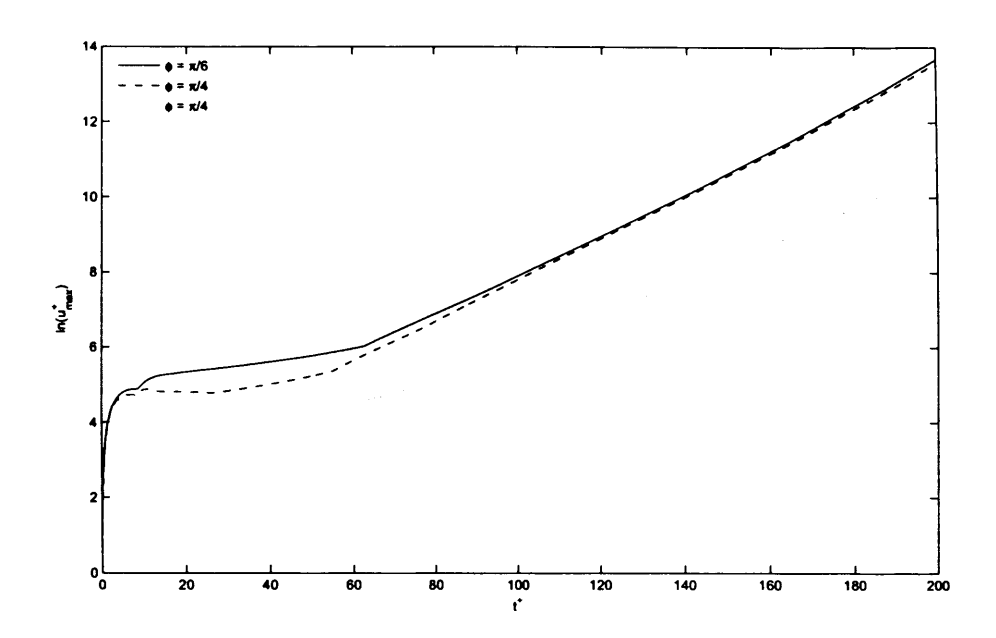


Figure 6.17: Development of streak magnitude in time for the optimum streak, with a spanwise wall oscillation magnitude of 10% of freestream velocity. $T^+ = 250$. A logarithmic scale is used for the velocities.

A longer term plot of those frozen oscillation cases where it seems that streak growth is most strongly promoted is shown in figure 6.17. Using a logarithmic scale for the streak magnitude, it is clear that the long-term growth of the streaks with frozen wall oscillations is exponential, and therefore produced by an unstable normal mode. This implies that for at least part of the wall oscillation cycle, the instantaneous basis flow is prone to unstable growth of normal modes i.e., for some of the cycle, the effect of the wall oscillation is in fact destabilising (since it is well-established that mean turbulent profiles are asymptotically stable to linear perturbations [64], in that although short-term growth of perturbations is possible, all perturbations will tend towards zero in finite time). Despite this, wall oscillation overall tends to reduce streak magnitude. This suggests that

a modified wall oscillation, which passes rapidly through those parts of the cycle which are instantaneously unstable and spends more time in those parts of the cycle which are instantaneously stable, might be more effective in inhibiting streak development than the naively chosen sinusoidal oscillation. For more discussion of this point, see section 6.5.

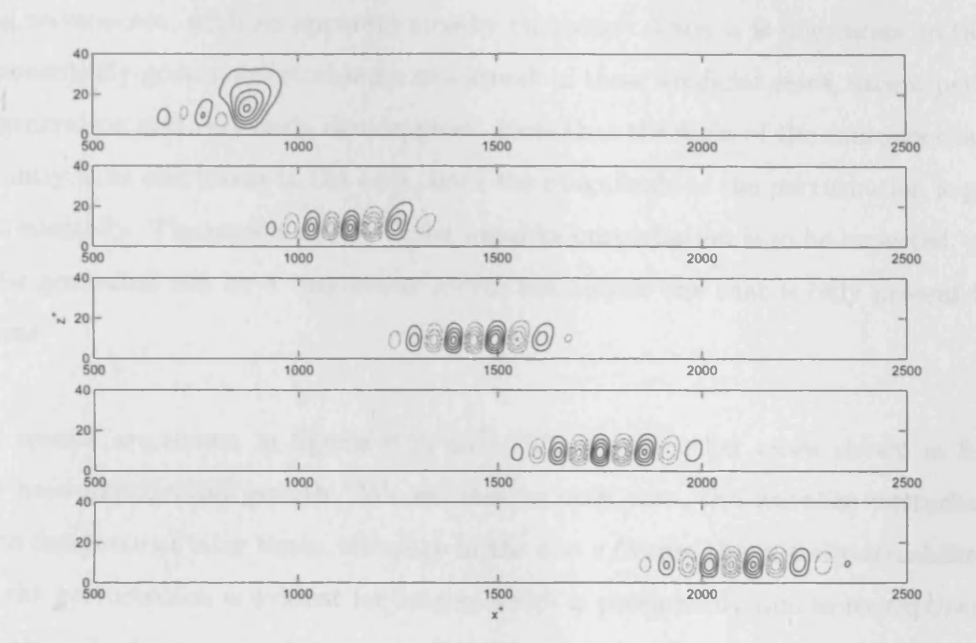


Figure 6.18: Profiles of $Re(u_x^+)$ for optimum streak based on a half-width of 15 wall units, subject to a spanwise wall oscillation of magnitude 10% of freestream velocity with $T^+=250$ which is frozen at the instant the streak forcing is switched on. $\phi=\pi/6$. Values shown for times $t^+=40,80,120,160,200$ from top to bottom. Contour intervals are different in each plot. From top to bottom, the intervals are $50,200,1500,1.5\times10^4,2\times10^5$. In each case, positive contours are solid and negative contours dotted. The zero contour is omitted.

Further evidence of the presence of unstable normal modes in some of the frozen oscillation flows is presented in figure 6.18, which shows the development of the perturbation over relatively long times in the case where the wall oscillation is frozen at a phase angle of $\phi = \pi/6$. At early times, we see that the perturbation displays both oscillatory and streaklike characteristics. The oscillatory nature is obvious, in that there are extrema of alternating signs along the streamwise direction. The streaklike nature is more apparent if one pictures an envelope around the perturbations; this shows the same lifting of the leading edge away from the wall as shown by streaks elsewhere e.g. figure 5.6. However, for later times the perturbation is in the form of a spatially convecting and temporally growing wavepacket, with no apparent streaky character. Thus it is inaccurate to talk of the exponentially growing perturbation as a streak in these artificial cases, except perhaps for its generation and very early development. Note that the scale of the contours changes significantly from one frame to the next, since the magnitude of the perturbation is growing exponentially. The packet nature of the wavelike perturbation is to be expected, given that it is generated not by a continuous source but rather one that is only present for a fixed time.

Similar results are shown in figures 6.19 and 6.20, for the other cases shown in figure 6.17 to have exponential growth. We see that in each case, the wavelike perturbation comes to dominate at later times, although in the $\phi = \pi/3$ case the initially streaklike nature of the perturbation is evident for longer, which is presumably due to its exponential growth phase beginning at a later time. We note also that the streamwise wavenumber of the wavelike perturbation appears to be different in the various cases, judging by the streamwise spacing of the extrema, so the wavenumber of the unstable mode must be fairly sensitive to the form of the frozen basis state.

Looking back at figure 6.12, we see that the times that are most prone to streak growth during the cycle are those shortly after the velocity of the wall oscillation has reached a maximum or minimum but before it has returned to zero. The simulations of frozen oscillations, in this light, produce the expected results, since freezing the oscillations at a time within this period of sensitivity $(0 < \phi < \pi/2)$ produces a secondary basis able to support exponentially growing perturbations. This is in contrast to the work of Blennerhassett et al. [5,6], which examined the behaviour of linear perturbations in one-

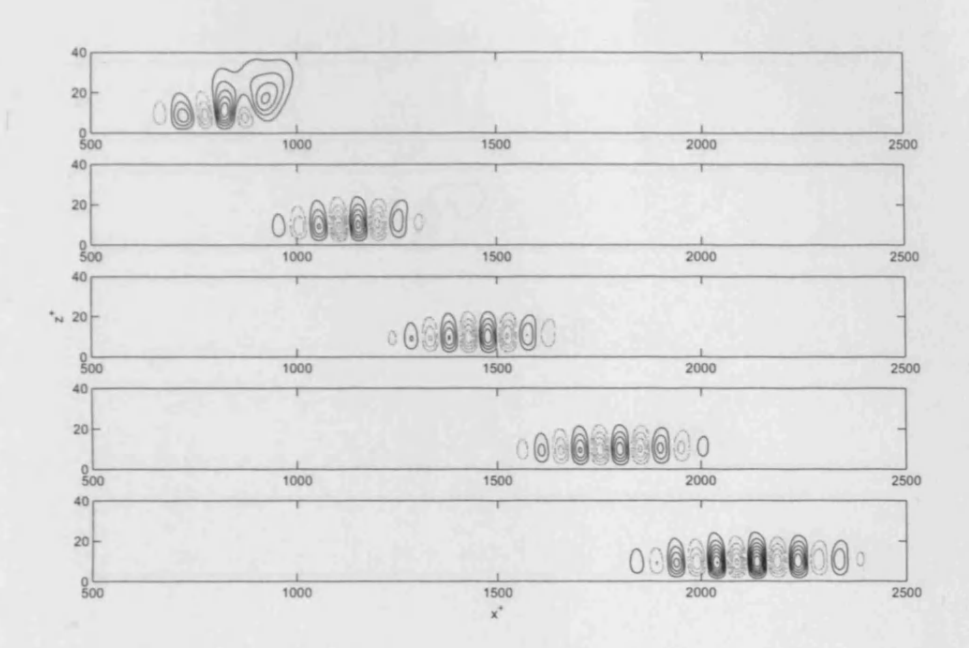


Figure 6.19: Profiles of $Re(u_x^+)$ for optimum streak based on a half-width of 15 wall units, subject to a spanwise wall oscillation of magnitude 10% of freestream velocity with $T^+=250$ which is frozen at the instant the streak forcing is switched on. $\phi=\pi/4$. Values shown for times $t^+=40,80,120,160,200$ from top to bottom. Contour intervals are different in each plot. From top to bottom, the intervals are $20,150,1500,1.5\times10^4,1.5\times10^5$. In each case, positive contours are solid and negative contours dotted. The zero contour is omitted.

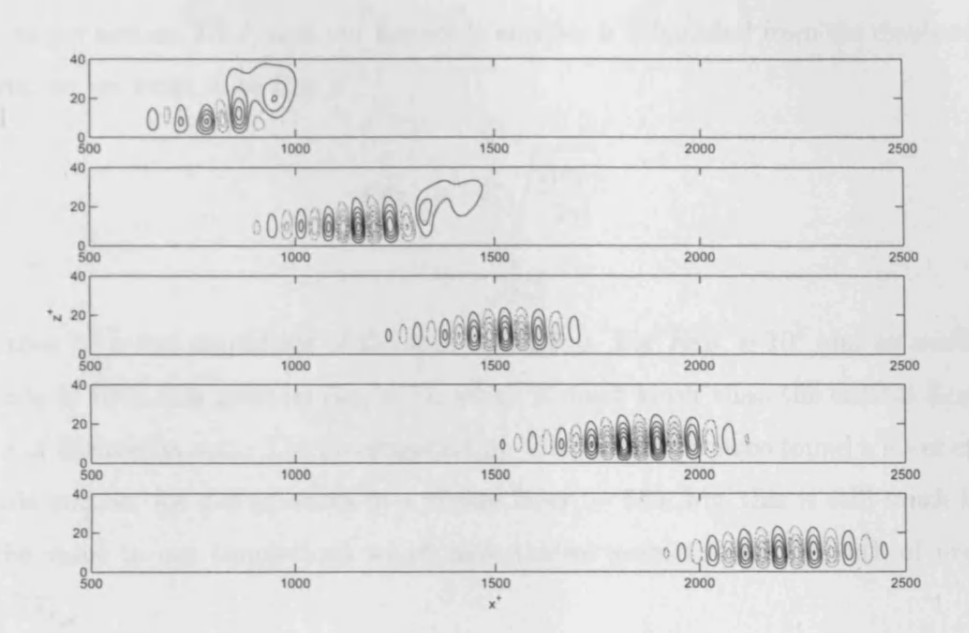


Figure 6.20: Profiles of $Re(u_x^+)$ for optimum streak based on a half-width of 15 wall units, subject to a spanwise wall oscillation of magnitude 10% of freestream velocity with $T^+=250$ which is frozen at the instant the streak forcing is switched on. $\phi=\pi/3$. Values shown for times $t^+=40,80,120,160,200$ from top to bottom. Contour intervals are different in each plot. From top to bottom, the intervals are 10, 20, 1000, 1000, 5000. In each case, positive contours are solid and negative contours dotted. The zero contour is omitted.

and two-dimensional Stokes layers and found that the disturbance growth was strongest when the oscillation velocity was close to zero. They also found that disturbances would only grow above a critical Reynolds number of approximately 700. The Reynolds number in this instance is calculated using the characteristics of the Stokes layer; if we denote this as Re_S , it can be calculated in this instance from the Reynolds number in our formulation (recall, as per section 2.4.2, that our Reynolds number is calculated from the displacement thickness, so we write it as Re_{δ^*}):

$$Re_{S} = \hat{u}_{y}^{\star} \sqrt{\frac{Re_{\delta^{\star}}}{2\gamma}}$$

$$= \frac{\hat{u}_{y}^{\star +}}{\sqrt{2\gamma^{+}}}$$
(6.1)

Recall that \hat{u}_y^* is the amplitude of the wall oscillation. For $Re_{\delta^*} = 10^4$ and an oscillation amplitude of 10%, this gives us $Re_S \approx 12$, which is much lower than the critical Reynolds number of Blennerhassett. The investigation by Vittori and Verzicco found a lower critical Reynolds number for disturbances to a Stokes layer, ~ 550 , but this is still much higher than the value in our simulations which nevertheless seem to show growth of unstable modes [77].

Bear in mind, however, that we are looking at a quite different type of perturbation, one propagating not along the direction of the Stokes oscillation but in the direction transverse to it. It is reasonable to assume that the presence of a nonzero mean flow will profoundly influence the stability characteristics of the Stokes layer, but in this case it may be misleading to think of the problem in this manner. Instead, it may be more meaningful to think of the disturbances as existing and developing in a modified turbulent boundary layer.

6.4 Effect of changing T^+

Another topic of interest is the influence of T^+ , the period of the wall oscillation, on the effectiveness of our control scheme. Figures 6.21 and 6.22 present the same information for $T^+=125$ as is shown in figures 6.1 and 6.3 for $T^+=250$ i.e., for a doubling of frequency. We see that the reduction of the streak magnitude is greater in each case. Although this may not be immediately clear from a visual comparison of figures 6.3 and 6.22, it is confirmed by the results presented in figure 6.23, which presents the maximum streak magnitudes at a range of phase angles for both $T^+=125$ and $T^+=250$. This leads us to surmise that the effect of increasing the period from the canonical $T^+=250$ might simply be to reduce the ability of the wall forcing to affect the streak development. Figures 6.24 and 6.25, which show data from the $T^+=500$ case, indicate that this may be too simplistic a view.

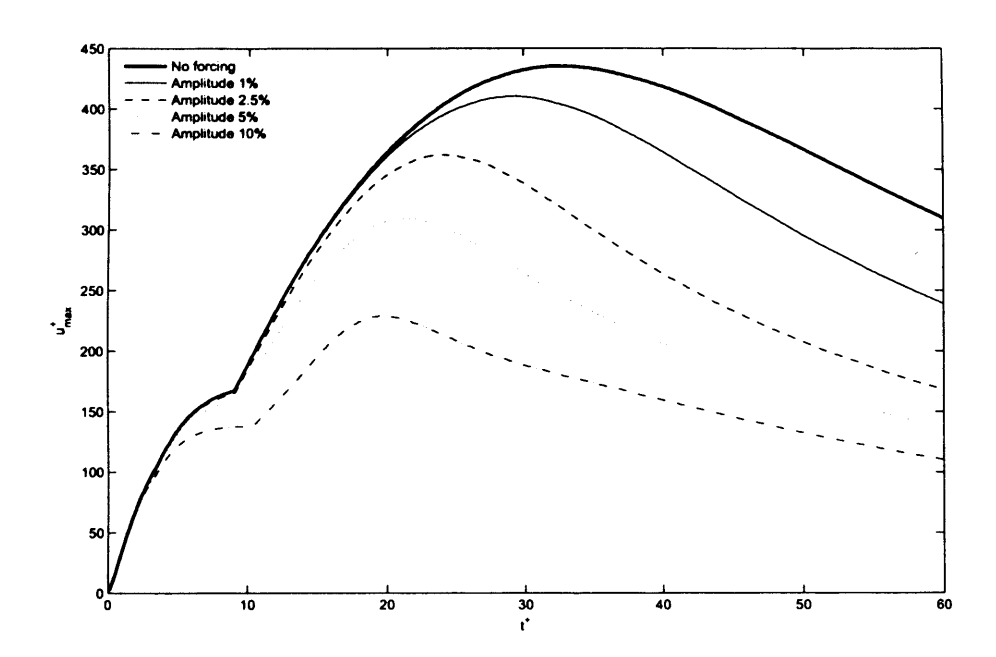


Figure 6.21: Development of streak magnitude in time for the optimum streak for a range of spanwise wall oscillation magnitudes. $T^+=125$. $\phi=0$ in all cases

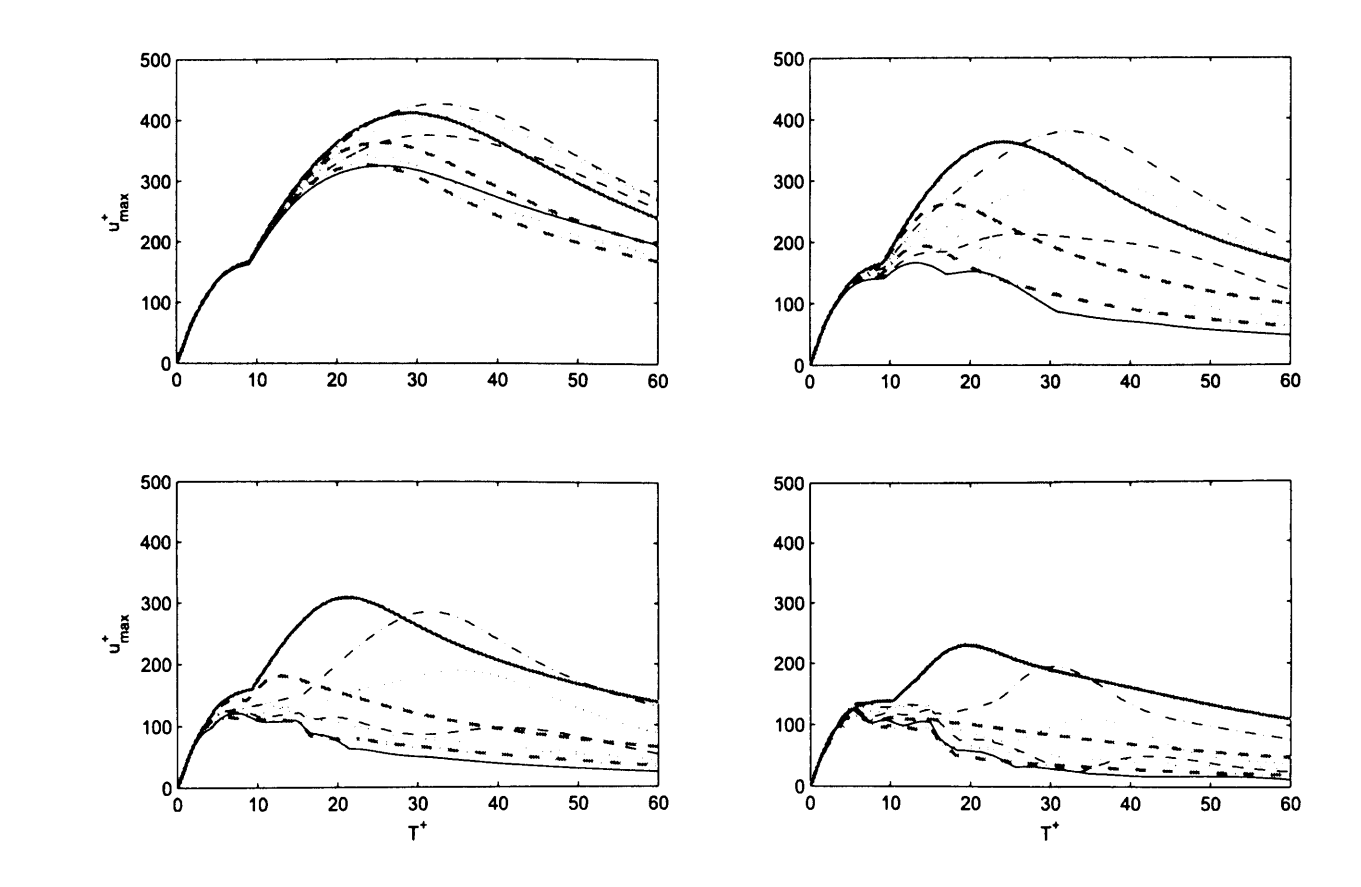


Figure 6.22: Development of streak magnitude in time for the streak with $\lambda^+=75$ for a variety of wall oscillations with $T^+=125$. Different frames show different forcing amplitudes. Clockwise from top left: amplitude 1%, amplitude 2.5%, amplitude 10%, amplitude 5%. Within each frame, different plots show different phases ϕ : solid grey $\phi=0$, dashed grey $\phi=\pi/6$, dotted grey $\phi=\pi/4$, dash-dotted grey $\phi=\pi/3$, solid black $\phi=\pi/2$, dashed black $\phi=2\pi/3$, dotted black $\phi=3\pi/4$, dash-dotted black $\phi=5\pi/6$.

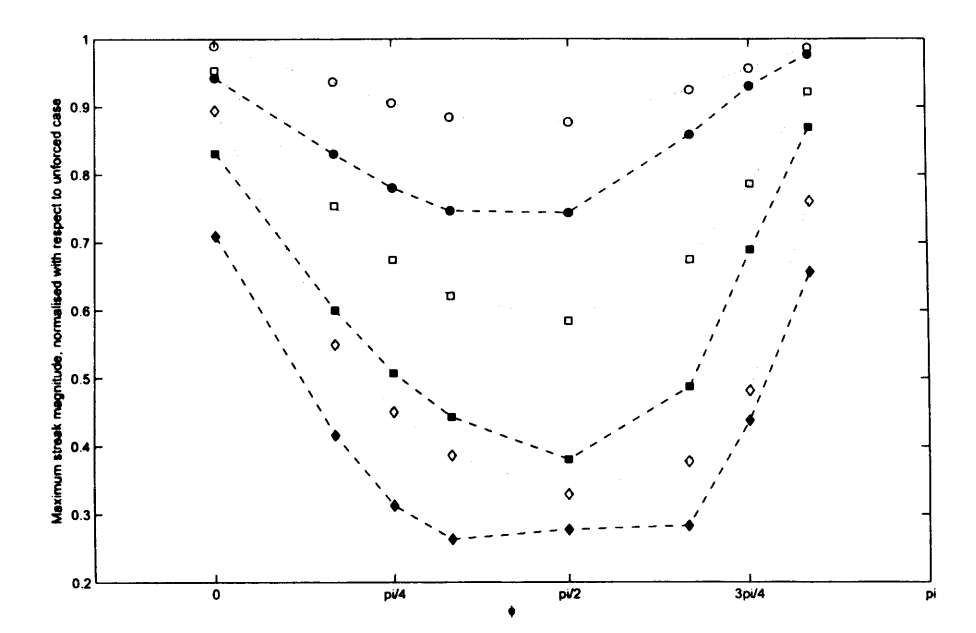


Figure 6.23: Ratios of maximum streak magnitude attained in cases with wall normal forcing to the unforced case. Empty symbols with dotted lines show the $T^+=250$ case, filled symbols with dashed lines the $T^+=125$ case. Circles, forcing amplitude 1%; squares, forcing amplitude 2.5%; diamonds, forcing amplitude 5%.

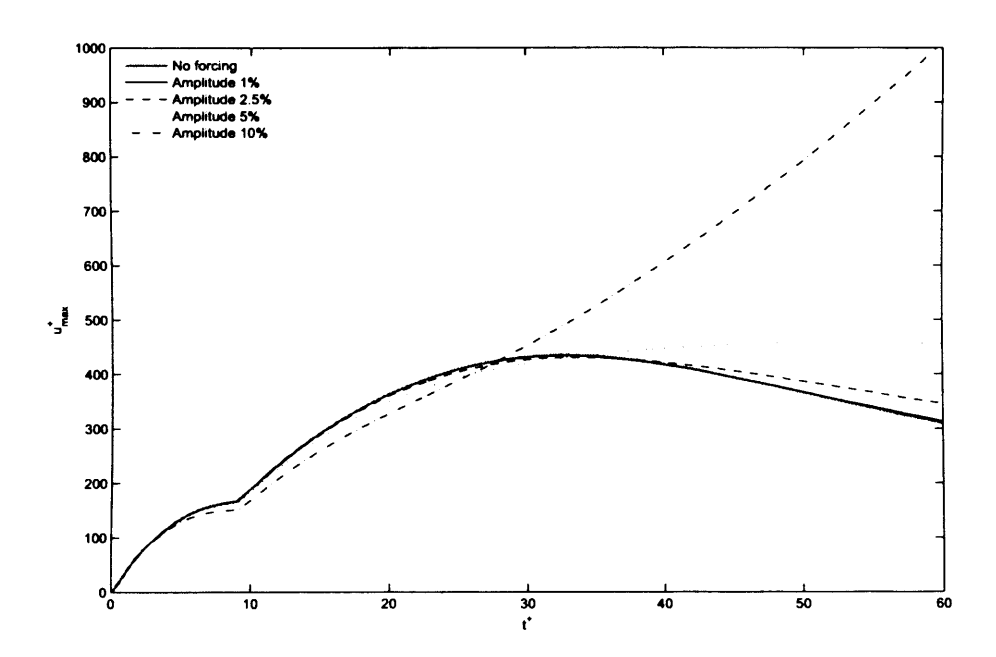


Figure 6.24: Development of streak magnitude in time for the optimum streak for a range of spanwise wall oscillation magnitudes. $T^+=500.$ $\phi=0$ in all cases

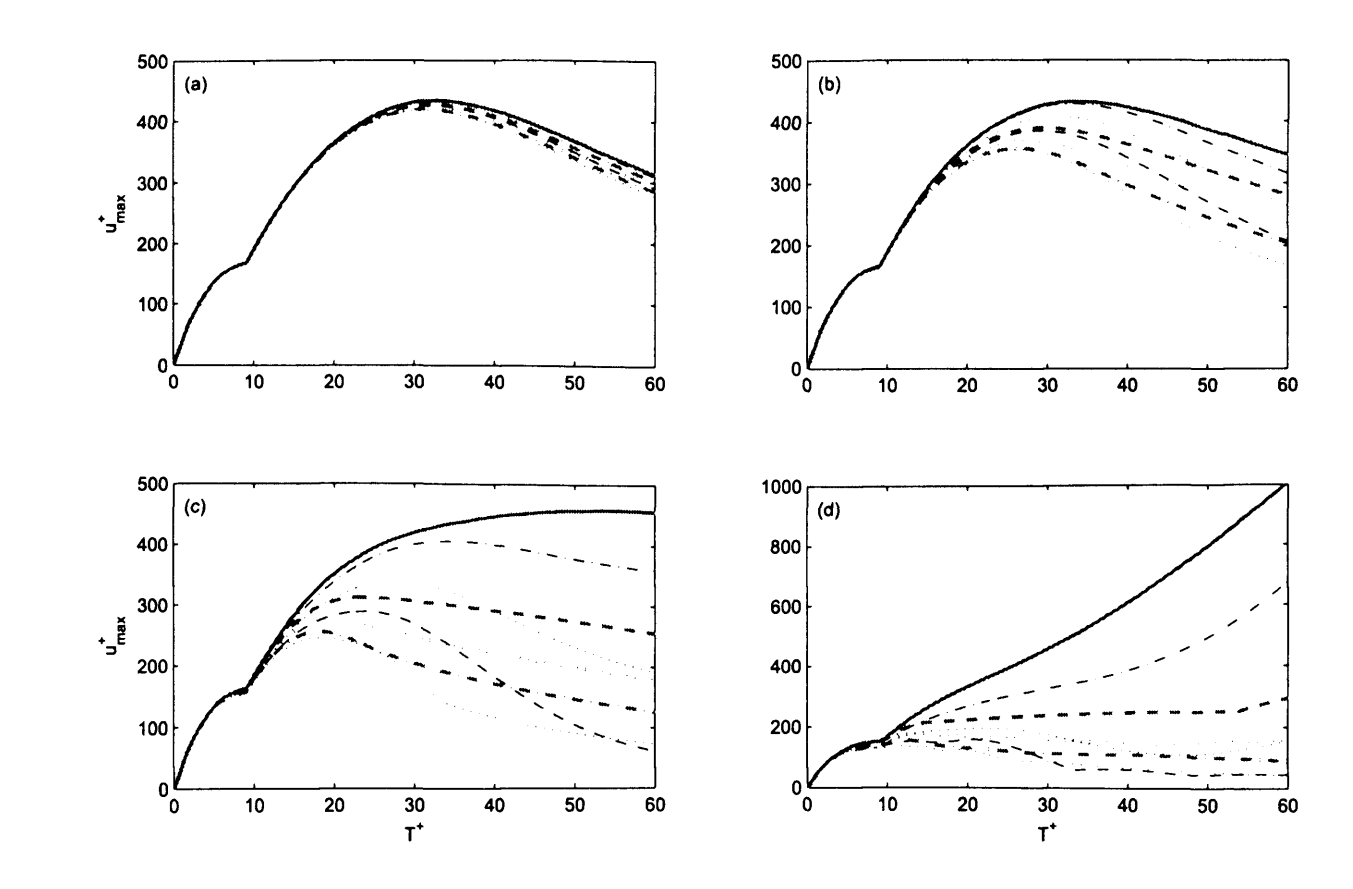


Figure 6.25: Development of streak magnitude in time for the streak with $\lambda^+ = 75$ for a variety of wall oscillations with $T^+ = 500$. Different frames show different forcing amplitudes: (a) amplitude 1%, (b) amplitude 2.5%, (c) amplitude 5%, (d) amplitude 10%. Within each frame, different plots show different phases ϕ : solid grey $\phi = 0$, dashed grey $\phi = \pi/6$, dotted grey $\phi = \pi/4$, dash-dotted grey $\phi = \pi/3$, solid black $\phi = \pi/2$, dashed black $\phi = 2\pi/3$, dotted black $\phi = 3\pi/4$, dash-dotted black $\phi = 5\pi/6$.

The most interesting phenomenon observed in the results presented in these figures is that high-amplitude wall oscillations, for certain phase angles, significantly amplify the streak growth. This is most apparent for the amplitude 10% cases with $\phi = 0$, $\pi/6$ and $5\pi/6$ i.e. those cases where the wall velocity is at or near an extremum when the streak forcing is switched on (these calculations do not freeze the wall oscillation). The longer term development of these streaks is illustrated in figure 6.26, which employs a logarithmic scale for u_{max}^+ . The strongest streak, with phase angle $\phi = 5\pi/6$, displays some concavity during its growth when plotted on a logarithmic scale, indicating that the growth is extremely rapid. The maximum attained by this streak is ~ 50 times greater than that attained by the unmodified streak.

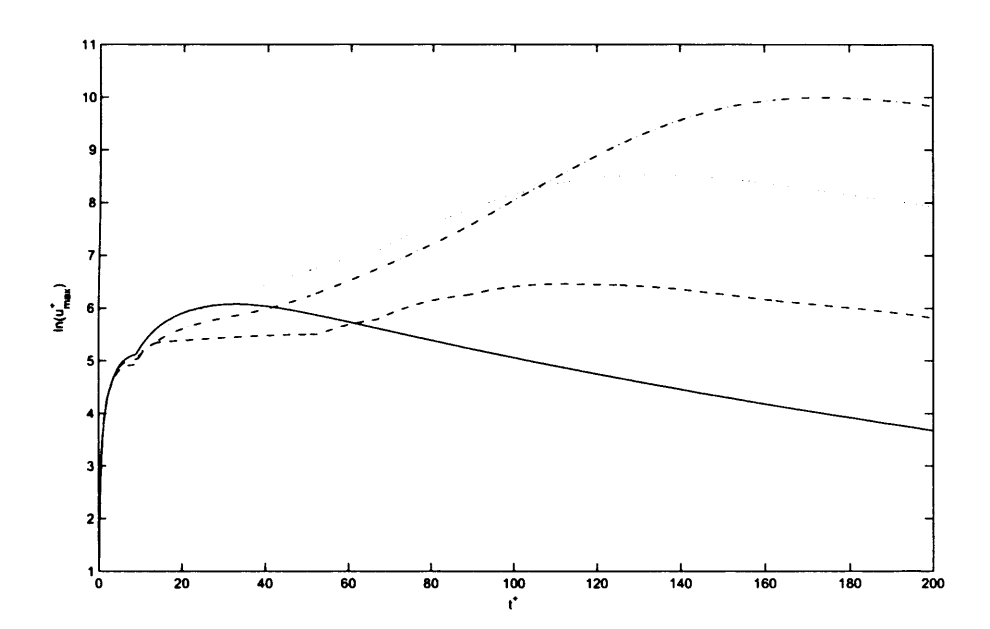


Figure 6.26: Development of streak magnitude in time for the optimum streak, with a spanwise wall oscillation magnitude of 10% of freestream velocity. $T^+ = 500$. Dotted line: $\phi = 0$, dashed line: $\phi = \pi/6$, dash-dotted line: $\phi = 5\pi/6$, solid line: streak with no wall oscillation. t^+ is zeroed to the switching on of the streak forcing in each case.

Profiles of these disturbances in the (x^+, z^+) -plane are shown in figures 6.27 to 6.29. We see that the form of the perturbations resembles that of the linearly growing wavepackets seen in the frozen oscillation cases (figures 6.18 to 6.20). However, these perturbations do not appear so purely wavelike. We observe that unlike the frozen oscillation cases, where the wavepacket alignment was purely parallel to the wall, part of the leading edge of the perturbations is lifted away from the wall in the same manner as a streak in an unforced boundary layer. This is particularly visible in figure 6.27. A simulation of the $\phi = 5\pi/6$ case (illustrated in figure 6.29) on a refined grid produced results indistinguishable from those presented here. This indicates that these results are genuine and not artifacts of an insufficiently resolved flow field (assuming, of course, that the $\phi = 5\pi/6$ case is representative). It seems, then, that in some cases where there is an oscillating basic state, normal-mode-like disturbances can grow and then decay, and in the process produce (or rather sustain) streaky structures until much later times than is possible in a basic turbulent boundary layer state without any wall oscillation.

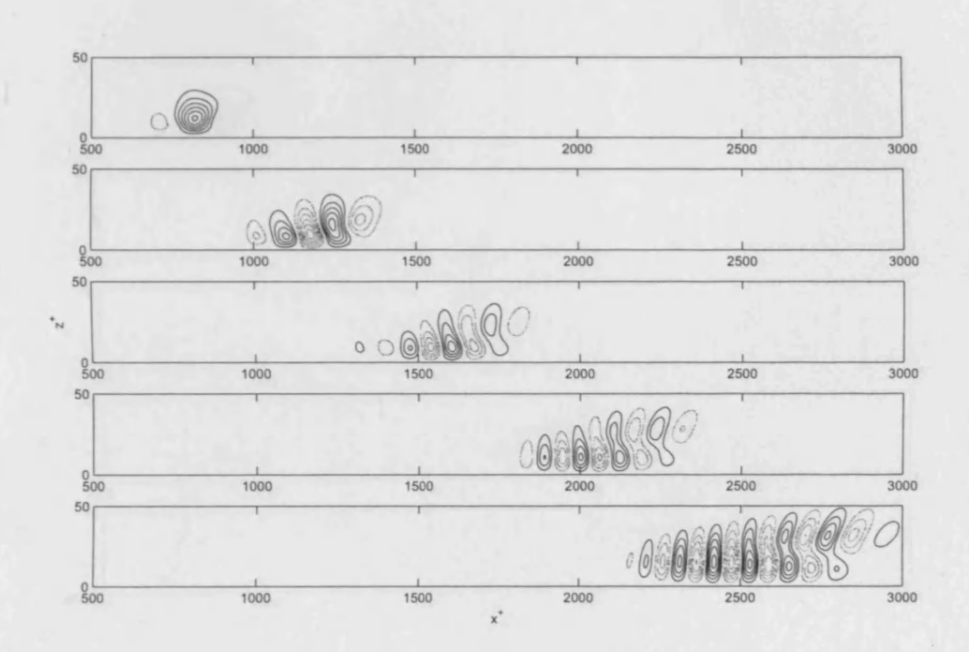


Figure 6.27: Profiles of $Re(u_x^+)$ for optimum streak based on a half-width of 15 wall units, subject to a spanwise wall oscillation of magnitude 10% of freestream velocity with $T^+ = 500$. $\phi = 0$. Values shown for times $t^+ = 40, 80, 120, 160, 200$ from top to bottom. Contour intervals are different in each plot. From top to bottom, the intervals are 100, 300, 1000, 1000, 500. In each case, positive contours are solid and negative contours dotted. The zero contour is omitted.

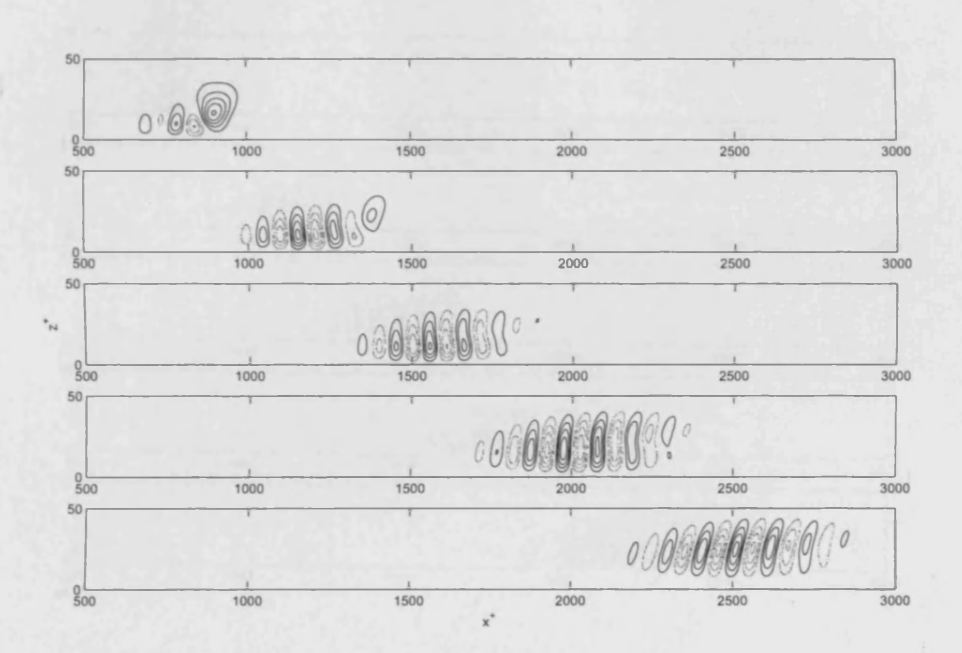


Figure 6.28: Profiles of $Re(u_x^+)$ for optimum streak based on a half-width of 15 wall units, subject to a spanwise wall oscillation of magnitude 10% of freestream velocity with $T^+ = 500$. $\phi = \pi/6$. Values shown for times $t^+ = 40, 80, 120, 160, 200$ from top to bottom. Contour intervals are different in each plot. From top to bottom, the intervals are 40, 100, 150, 100, 75. In each case, positive contours are solid and negative contours dotted. The zero contour is omitted.

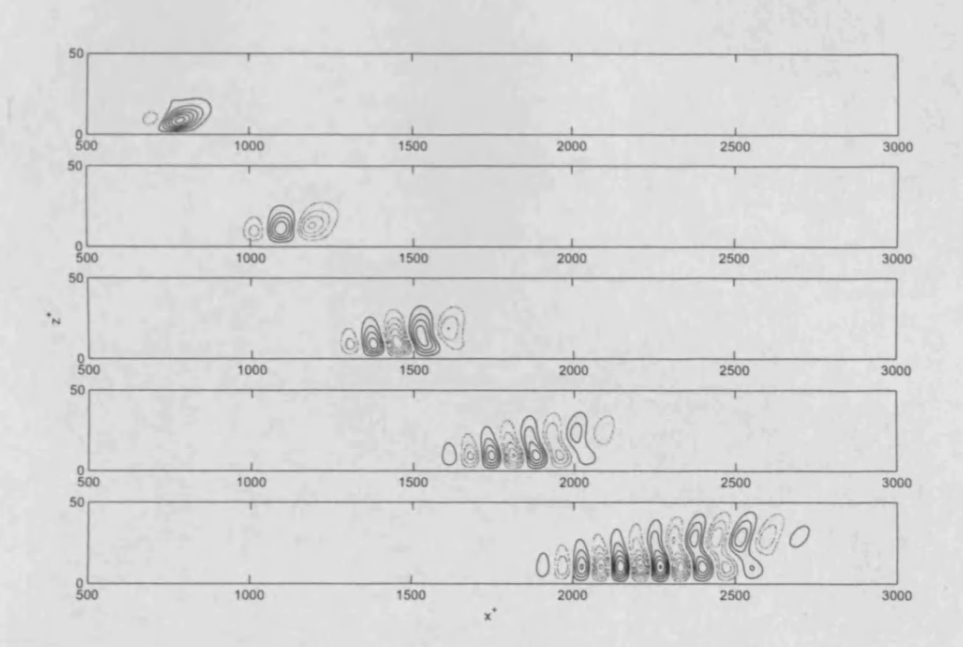


Figure 6.29: Profiles of $Re(u_x^+)$ for optimum streak based on a half-width of 15 wall units, subject to a spanwise wall oscillation of magnitude 10% of freestream velocity with $T^+ = 500$. $\phi = 5\pi/6$. Values shown for times $t^+ = 40, 80, 120, 160, 200$ from top to bottom. Contour intervals are different in each plot. From top to bottom, the intervals are 50, 250, 1250, 4000, 3000. In each case, positive contours are solid and negative contours dotted. The zero contour is omitted.

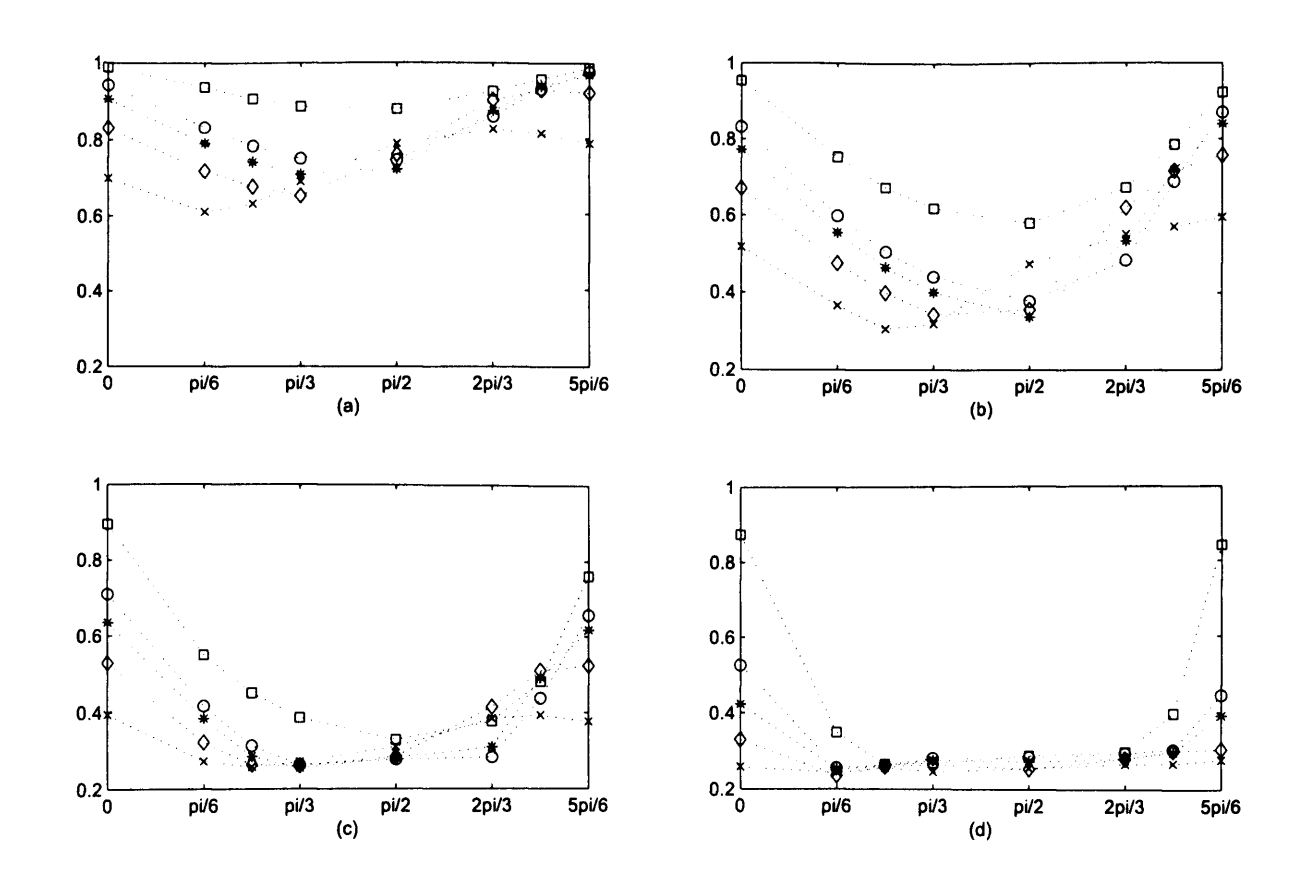


Figure 6.30: Ratio of maximum streak strength attained in various cases with wall oscillation to the unforced case. Different frames show different forcing amplitudes. Clockwise from top left: amplitude 1%, amplitude 2.5%, amplitude 10%, amplitude 5%. Within each frame, different symbols correspond to different oscillation periods: squares, $T^+ = 250$; circles, $T^+ = 125$; stars, $T^+ = 100$; diamonds, $T^+ = 75$; crosses, $T^+ = 50$. Streak strength, on the vertical axis, is expressed as a fraction of the strength attained by the optimum streak in the unforced case.

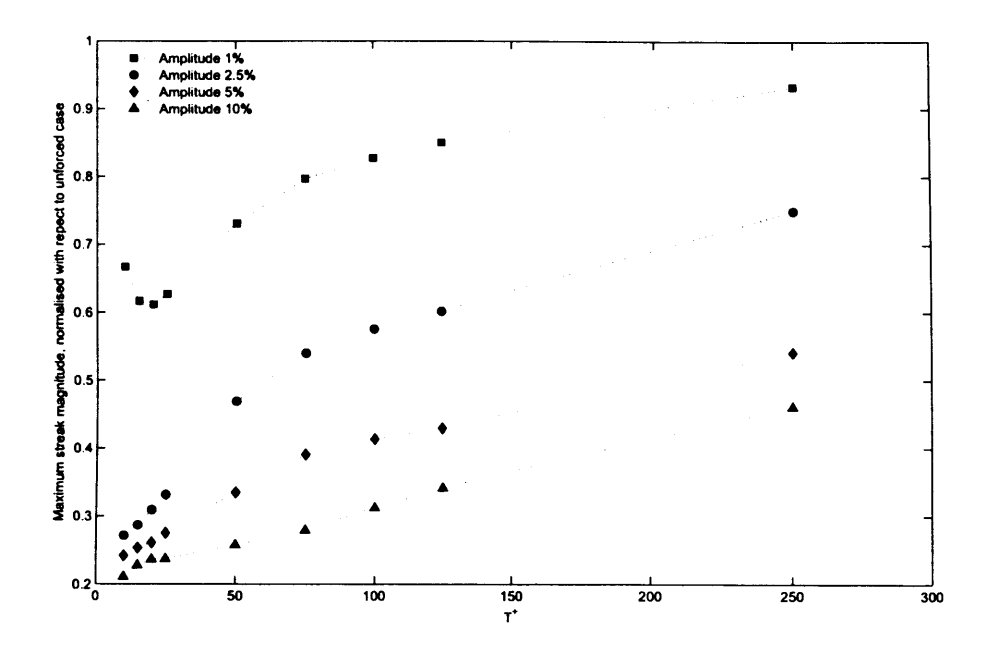


Figure 6.31: Dependence of the maximum streak strength attained in various wall oscillation cases on oscillation period. Streak strength is expressed as a fraction of the streak strength attained by the optimum streak in the unforced case.

Results from simulations at a wider range of frequencies are given in figures 6.30 and 6.31. Figure 6.30 shows the variation of streak magnitude with ϕ , and we see that as a general rule there is a U-shaped trend, such that values of ϕ specifying a forcing switch-on at or near extrema produce less of a reduction, and intermediate values produce a greater reduction. Figure 6.31 uses a weighted average across a range of phase angles to produce a single averaged streak magnitude for any given amplitude- T^+ pair. We see that increasing the amplitude of the oscillation produces a greater reduction in streak strength, as do higher frequencies. The exception to this rule is the 1% amplitude case, where $T^+ = 20$ yields an optimum reduction of the streak strength and higher frequencies are less effective.

The averaged streak magnitude shown in figure 6.31 is calculated in the following man-

ner. For the cases with $T^+>25$, we performed simulations for the phase angles $\phi=0,\frac{\pi}{6},\frac{\pi}{4},\frac{\pi}{3},\frac{\pi}{2},\frac{2\pi}{3},\frac{3\pi}{4}$ and $\frac{5\pi}{6}$. This is the set of phase angles used to produce the results shown in, for example, figures 6.3 and 6.22. To obtain our weighting, we place these values of ϕ on the interval $0\leq\phi<\pi$ and assign a weight to the data obtained at a given value of ϕ according to the proportion of this interval which is closer to this value than any other of the values used. Note that the interval was considered to be cyclic for the purpose of calculating this weight; thus the points $\frac{11\pi}{12}<\phi<\pi$ are treated as being closer to $\phi=0$ than $\phi=\frac{5\pi}{6}$. In this scheme, the data obtained using $\phi=0$ or $\frac{\pi}{2}$ has a weight of $\frac{1}{6}$, the data obtained using $\phi=\frac{\pi}{4}$ or $\frac{3\pi}{4}$ has a weight of $\frac{1}{12}$, and the data obtained using any other value of ϕ has a weight of $\frac{1}{8}$. For cases with $T^+\leq 25$, we found that the changes in the streak development as ϕ was altered were no longer so pronounced, as is illustrated in figure 6.32. Thus we performed calculations for only four different values of ϕ , $\phi=0,\frac{\pi}{4},\frac{\pi}{2}$ and $\frac{3\pi}{4}$: the weighting was correspondingly simplified, with each of these cases having a weighting of $\frac{1}{4}$ for the calculation of the average maximum magnitude.

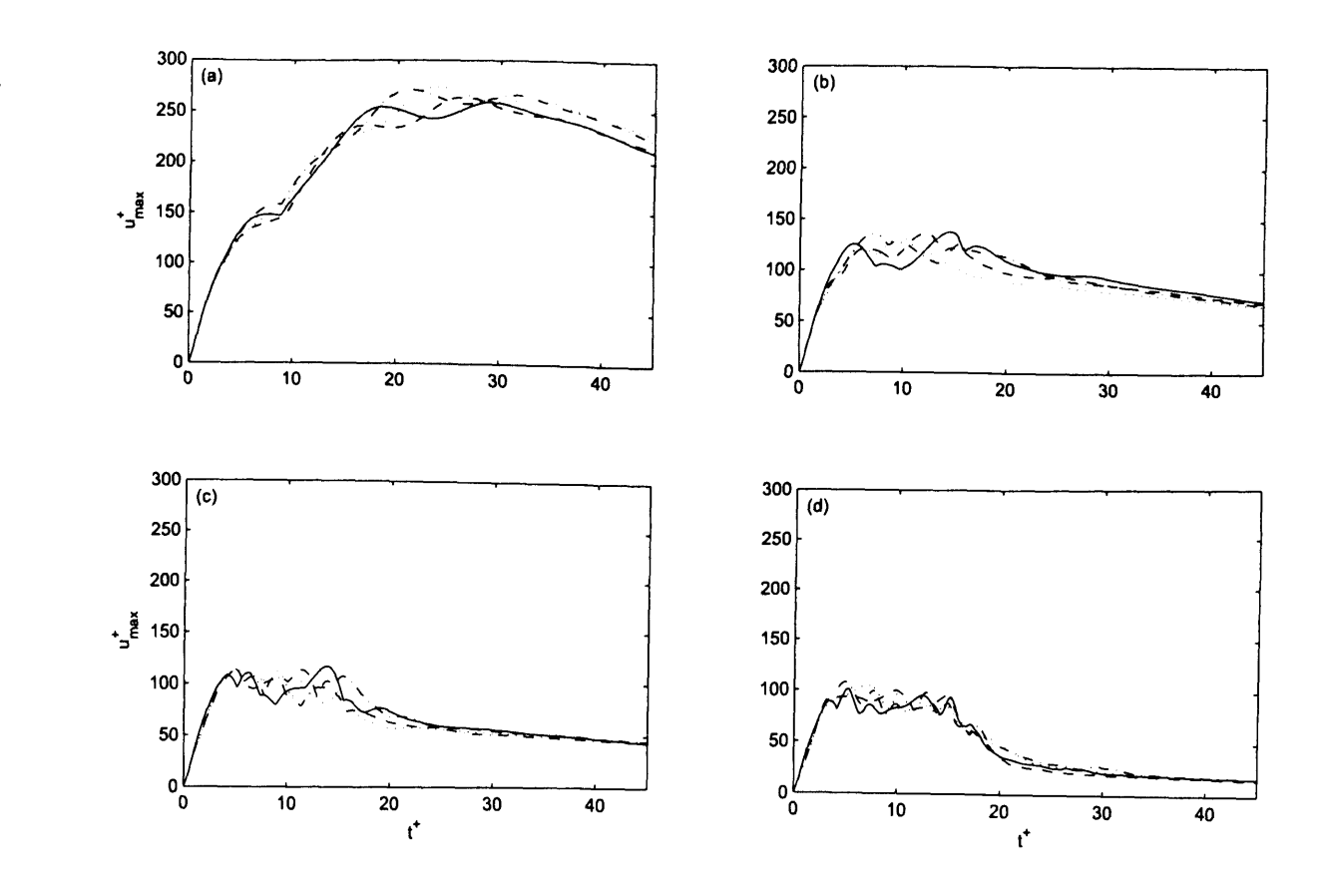


Figure 6.32: Development of streak magnitude in time for the streak with $\lambda^+ = 75$ for a variety of wall oscillations with $T^+ = 20$. Different frames show different forcing amplitudes: (a) amplitude 1%, (b) amplitude 2.5%, (c) amplitude 5%, (d) amplitude 10%. Within each frame, different plots show different phases ϕ : solid line $\phi = 0$, dashed line $\phi = \pi/4$, dotted line $\phi = \pi/2$, dash-dotted line $\phi = 3\pi/4$.

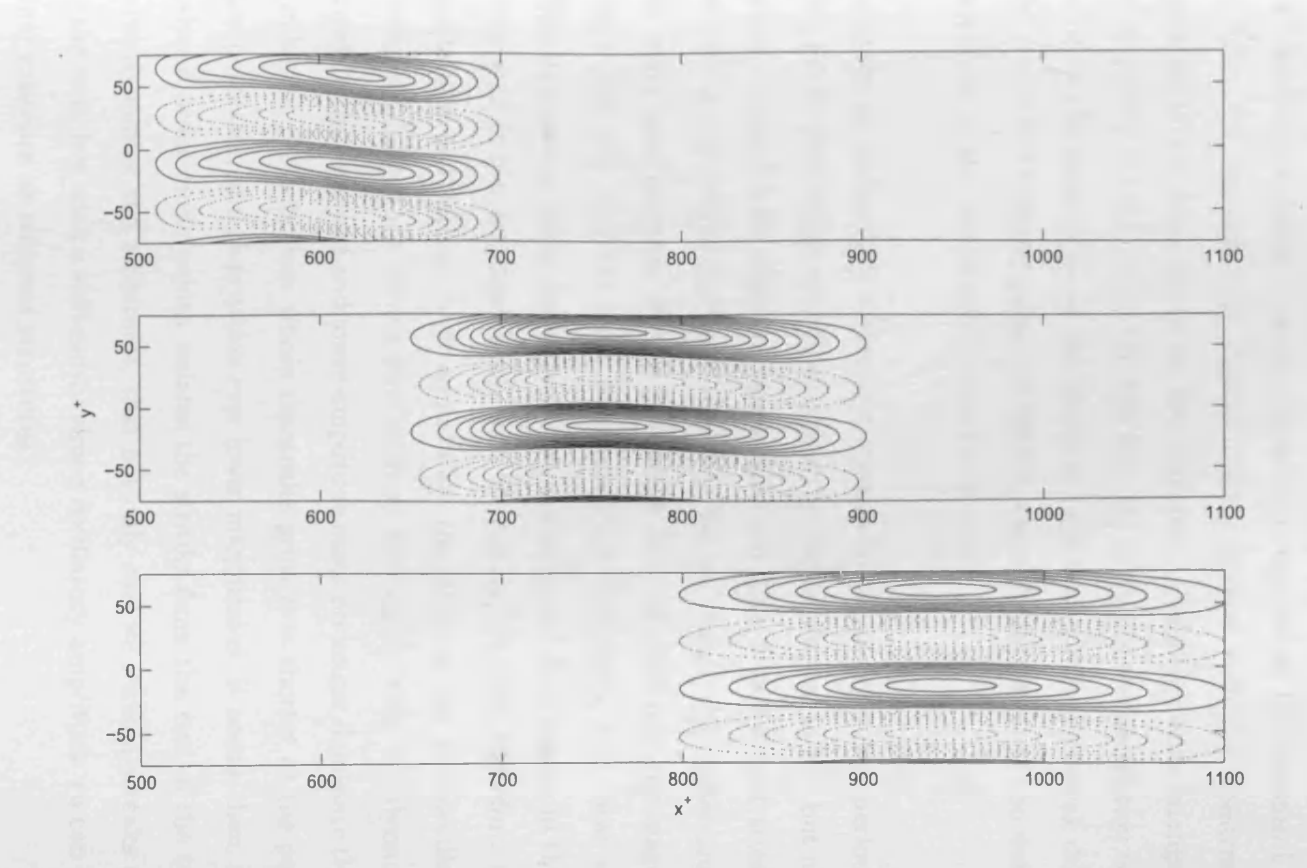


Figure 6.33: Contours of $Re(u_x^+)$ for optimum streak based on a half-width of 15 wall units, subject to a spanwise wall oscillation with magnitude 1% of freestream velocity and period $T^+=20$. $\phi=\pi/2$. Values are taken from a wall-normal location $z^+=15$. Contours are at intervals of 25, with positive contours solid and negative contours dashed. The zero contour is omitted. Values shown for times $t^+=18,36,54$ from top to bottom.

The streaks from the amplitude 1% case with an oscillation period $T^+=20$ are illustrated in plan view in figure 6.33. There do not appear to be any significant structural changes for these high-frequency oscillations when compared to the canonical case, as illustrated in figure 6.5; we still have streaks roughly aligned with the freestream, but exhibiting some deviation from the mean flow direction. One observable change with the increase in frequency is that due to the fact that the period of the oscillation is now short enough to be on the same order as the length of time over which the streak develops, we see that the streak has become somewhat kinked, since the direction of the wall forcing changes a few times of the course of the streak's lifetime.

In order to understand why there appears to be an optimum period for streak reduction in the case where the amplitude of the wall oscillation is 1%, but not if the amplitude is any higher, let us compare figures 6.34 and 6.35, which depict streaks subject to wall oscillations at amplitudes of 1% and 5%. We see that in the higher-amplitude case, there are more local extrema present in the flow field, of relatively low magnitude. The loweramplitude case still has more than one local extremum, but these are much stronger. This structure is more similar to the streak structure that is seen in the unforced case, as illustrated in (for example) figure 5.6. We can hypothesise, therefore, that for low-period oscillations at relatively high amplitudes, the effect of the wall oscillation is sufficiently strong to disrupt the streak formation so thoroughly that the dynamics governing the streak in the unforced and lower-amplitude cases no longer dominate the flow. This leaves incoherent perturbations whose timescales grow ever shorter as the period of the oscillation decreases, and thus attain ever lower magnitudes. It seems then, that at least in our reduced order model which isolates the streaks from the rest of the turbulent boundary layer dynamics and structures, that not only can we weaken streaks through oscillation of the wall, but with a sufficiently strong oscillatory amplitude we can completely disrupt their existence as coherent structures.

An alternative way of characterising the wall oscillations is by the maximum displacement

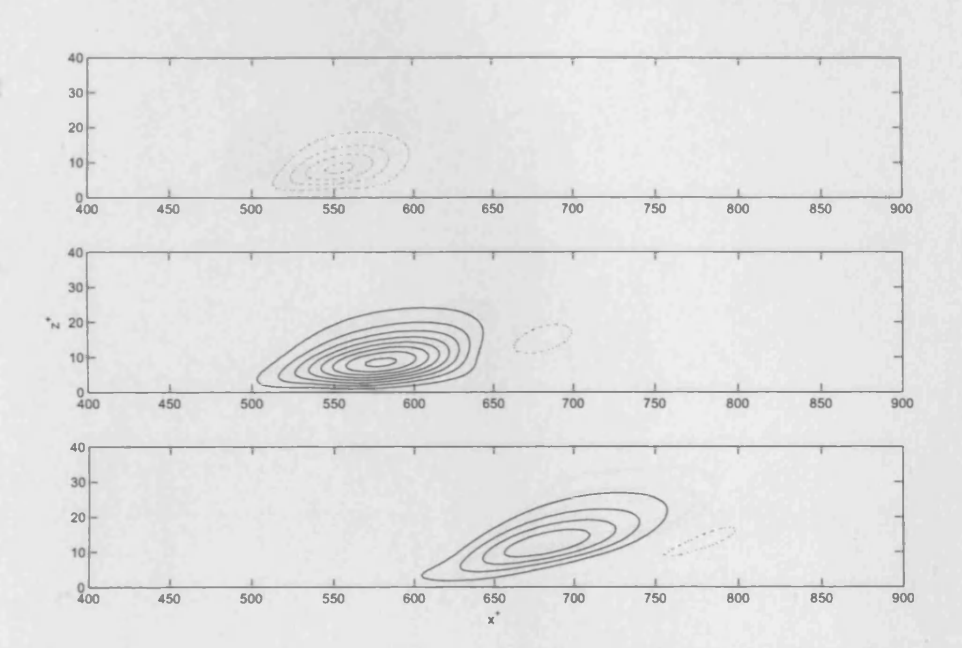


Figure 6.34: Profiles $Re(u_x^+)$ for the perturbation generated by the streak forcing with $z_f^+ = 12.5, \lambda^+ = 75$, subject to a wall oscillation of amplitude 1% (equivalent to a wall oscillation amplitude of $\hat{u}_y^{+*} = 0.271$) with period $T^+ = 15$. Contours are at intervals of 20, with positive contours solid and negative contours dashed. The zero contour is omitted. Values shown for times $t^+ = 10, 20, 30$ from top to bottom.

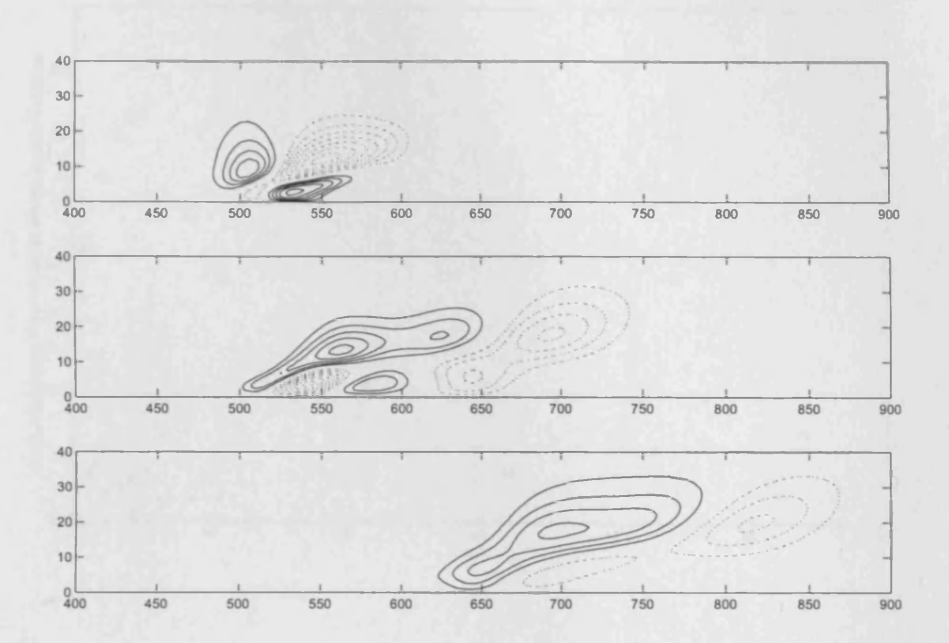


Figure 6.35: Profiles $Re(u_x^+)$ for the perturbation generated by the streak forcing with $z_f^+ = 12.5$, $\lambda^+ = 75$, subject to a wall oscillation of amplitude 5% (equivalent to a wall oscillation amplitude of $\hat{u}_y^{+*} = 1.35$) with period $T^+ = 10$. Contours are at intervals of 5, with positive contours solid and negative contours dashed. The zero contour is omitted. Values shown for times $t^+ = 10, 20, 30$ from top to bottom.

the wall goes through from its initial at-rest position, which we calculate as $D^+ = \hat{u}_y^{*+}/\gamma^+$. We hoped that this might be a useful means of parametrising the wall oscillation in such a way as to show commonalities among the cases with different velocity amplitudes, but as seen in figure 6.36, no such relationship is apparent.

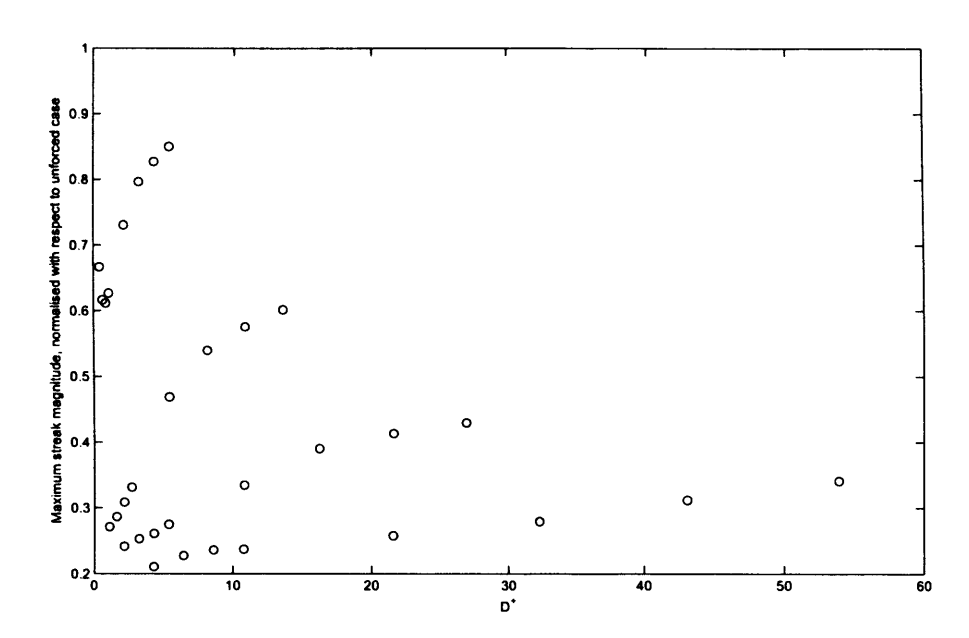


Figure 6.36: Dependence of the maximum streak strength attained in various wall oscillation cases on maximum displacement of wall. Streak strength is expressed as a fraction of the streak strength attained by the optimum streak in the unforced case.

There is another point worth considering, before we press on. We have assumed in our examination of the wall oscillation that the spanwise spacing λ^+ which gives the optimum streak in the unforced case will continue to give the optimum streak in the case with oscillations. However, we have no a priori reason to assume this; the situation may instead be that the oscillations reduce the strength of the $\lambda^+ = 75$ streaks significantly more than streaks of other spanwise wavenumbers, thus creating a new optimum; it is plausible that there are streaks that are in fact strengthened by the wall motion. We investigate this possibility by performing a series of simulations with a range of different

 λ^+ values, the results of which are presented in figure 6.37. The streak magnitudes shown were calculated using the same weighted average that was employed for the results shown in figure 6.31.

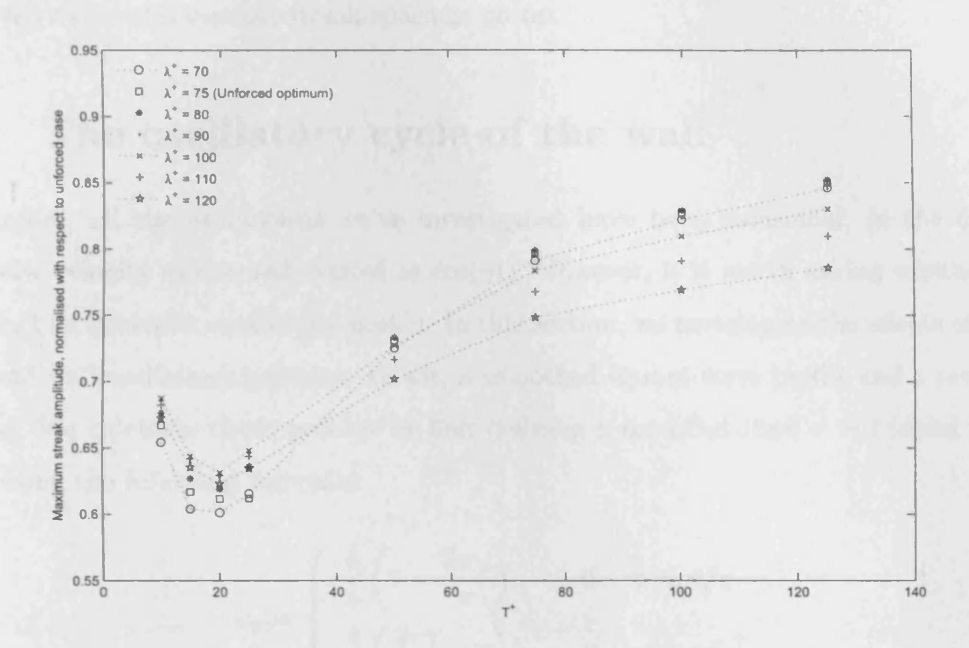


Figure 6.37: Dependence of the maximum streak strength attained on T^+ , with a wall oscillation of amplitude 1%. Streak strength is expressed as a fraction of the streak strength attained for the optimum streak ($z_f^+ = 12.5, \lambda^+ = 75$) in the unforced case. Different symbols show different values of λ^+ ; lines are included for some values of λ^+ to illustrate upper and lower limits of the streak magnitudes for different values of T^+ .

We see that varying λ^+ does indeed change the amount of reduction of the streak magnitude, although the overall trend is preserved, and the change is not very large. For large values of T^+ , there is a tight clustering of magnitudes for λ^+ -values near the unforced optimum of $\lambda^+ = 75$, although for $\lambda^+ > 100$ there is a significant drop-off. Below $T^+ = 50$, however, we find that the optimum (i.e., least reduced in magnitude by the oscillation) streaks occur at $\lambda^+ = 100$, and it is the streaks at lower values of λ^+ that now drop off. This is consistent with the observation reported by di Cicca et al. and Choi et

al. [17,24], who noted that streaks in fact occur at a wide range of spanwise scales, even though the median or mean scale may be taken as representative. With the imposition of an oscillatory wall, many of the lower- λ^+ scales are forced to coalesce, meaning that the observed mean and median streak spacings go up.

6.5 The oscillatory cycle of the wall

Heretofore, all the oscillations we've investigated have been sinusoidal, in the \hat{u}_y , the spanwise velocity of the wall, varied as $\cos(\gamma t)$. However, it is worth asking whether this is in fact an optimum oscillatory profile. In this section, we investigate the effects of using different wall oscillation patterns: to wit, a smoothed square-wave profile and a sawtooth profile. We calculate these profiles by first defining a modified time $\tau = t \pmod{2\pi/\gamma}$, then using the following formulae:

$$\hat{u}_{y} = \begin{cases} \frac{4}{\pi} \left(1 - \frac{2\tau\gamma}{\pi} \right) & \text{if } \tau \leq \pi/\gamma \\ \frac{4}{\pi} \left(\frac{2\tau\gamma}{\pi} - 3 \right) & \text{if } \tau > \pi/\gamma \end{cases}$$

$$(6.2)$$

$$\hat{u}_{y} = \begin{cases} \frac{1}{\ln (\cosh \pi/2\gamma)} \tanh \left(\frac{\pi}{2\gamma} - \tau\right) & \text{if } \tau \leq \pi/\gamma \\ \frac{1}{\ln (\cosh \pi/2\gamma)} \tanh \left(\tau - \frac{3\pi}{2\gamma}\right) & \text{if } \tau > \pi/\gamma \end{cases}$$
(6.3)

Equation 6.2 defines the sawtooth profile and equation 6.3 the smoothed square-wave profile. The magnitude of these profiles has been normalised such that the integral over a half-period is the same among the different profiles i.e., such that the total displacement of the wall is the same for any oscillatory pattern. When we talk about the amplitude of the oscillation in the square-wave and sawtooth cases, then, we do not mean the actual peak velocity attained by the wall, but the peak velocity that would be reach in a sinusoidal wall oscillation of the same total displacement. These profiles are depicted in figure 6.38. Plots of the development of streak magnitude for the square-wave and sawtooth cases, with an oscillation period of $T^+ = 250$ are given in figures 6.39 to 6.42; the equivalent data

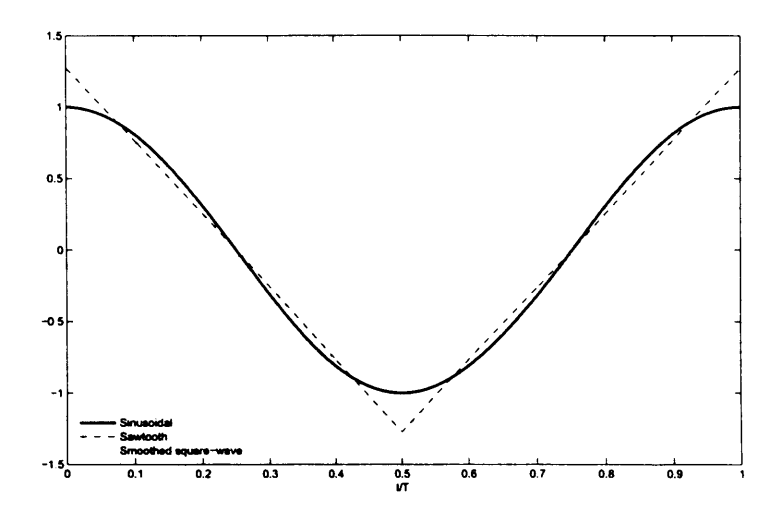


Figure 6.38: Depiction of the different oscillatory profiles. Time, on the horizontal axis, is expressed as a fraction of the oscillatory period. Magnitude, on the vertical axis, is expressed as a fraction of the amplitude of the sinusoidal oscillation.

for sinusoidal wall oscillation are presented in figures 6.1 and 6.3. We see largely similar characteristics as the sinusoidal oscillations for both square-wave and sawtooth profiles: significant changes in streak development for different values of ϕ and generally stronger reductions in streak strength as the oscillation amplitude is increased, for example. Note, however, for the square-wave oscillation in the cases with adjusted amplitudes of 5% and 10%, there are some cases for which there is significant amplification of the streaks. Presumably these cases are those for which, during the part of the oscillation when the wall velocity stays relatively constant, the modified secondary basis is unstable.

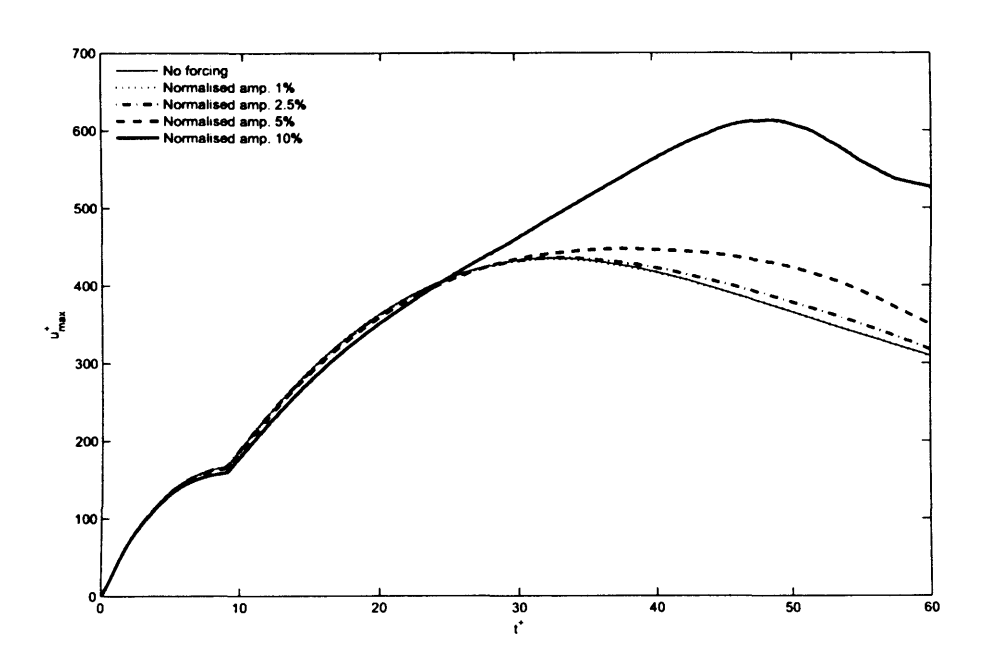


Figure 6.39: Development of streak magnitude in time for the optimum streak for a range of spanwise square-wave wall oscillation magnitudes. $T^+=250$. $\phi=0$ in all cases

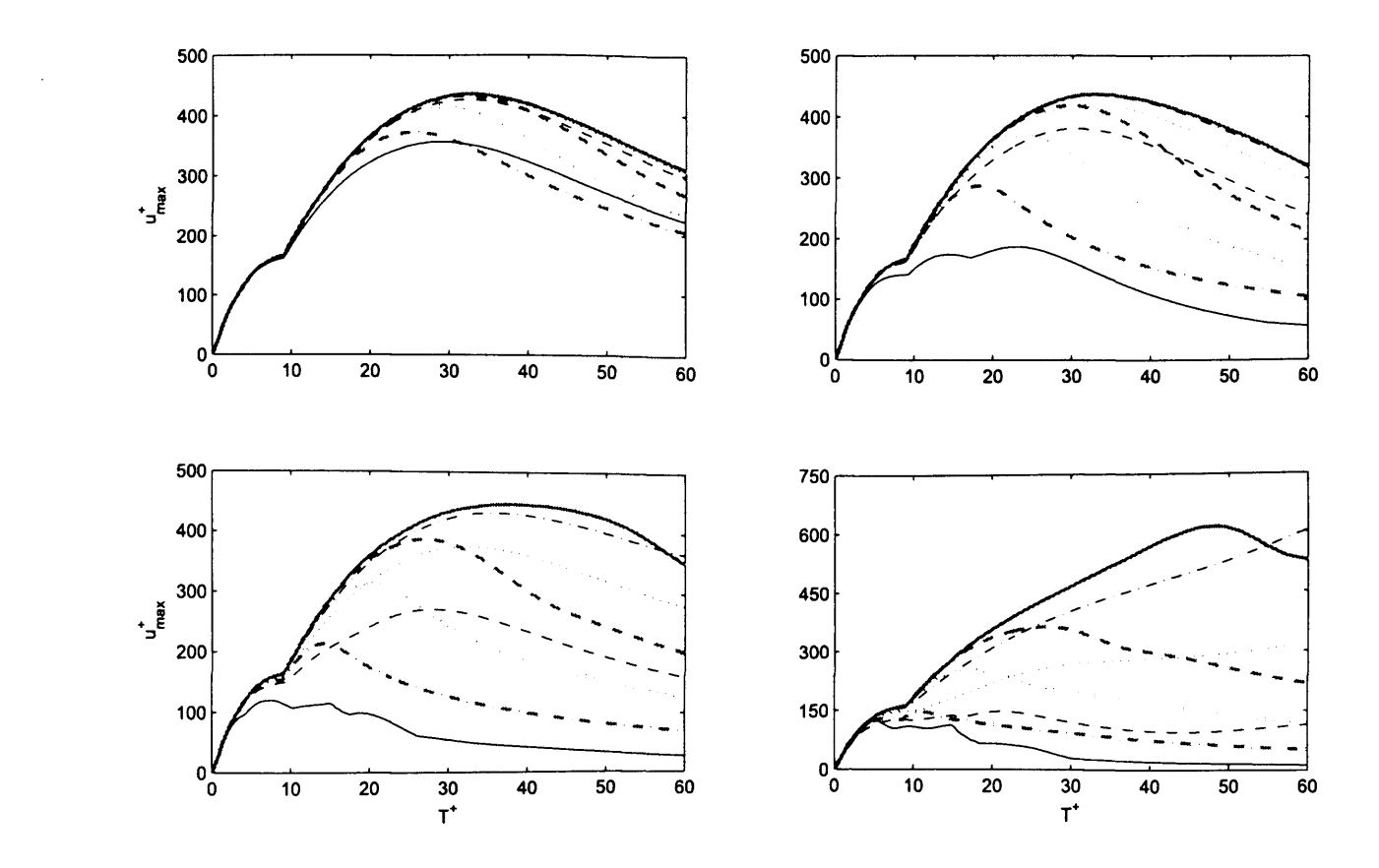


Figure 6.40: Development of streak magnitude in time for the streak with $\lambda^+=75$ for a variety of wall oscillations with a square-wave profile and $T^+=250$. Different frames show different forcing amplitudes. Clockwise from top left: amplitude 1%, amplitude 2.5%, amplitude 10%, amplitude 5%. Within each frame, different plots show different phases ϕ : solid grey $\phi=0$, dashed grey $\phi=\pi/6$, dotted grey $\phi=\pi/4$, dash-dotted grey $\phi=\pi/3$, solid black $\phi=\pi/2$, dashed black $\phi=2\pi/3$, dotted black $\phi=3\pi/4$, dash-dotted black $\phi=5\pi/6$.

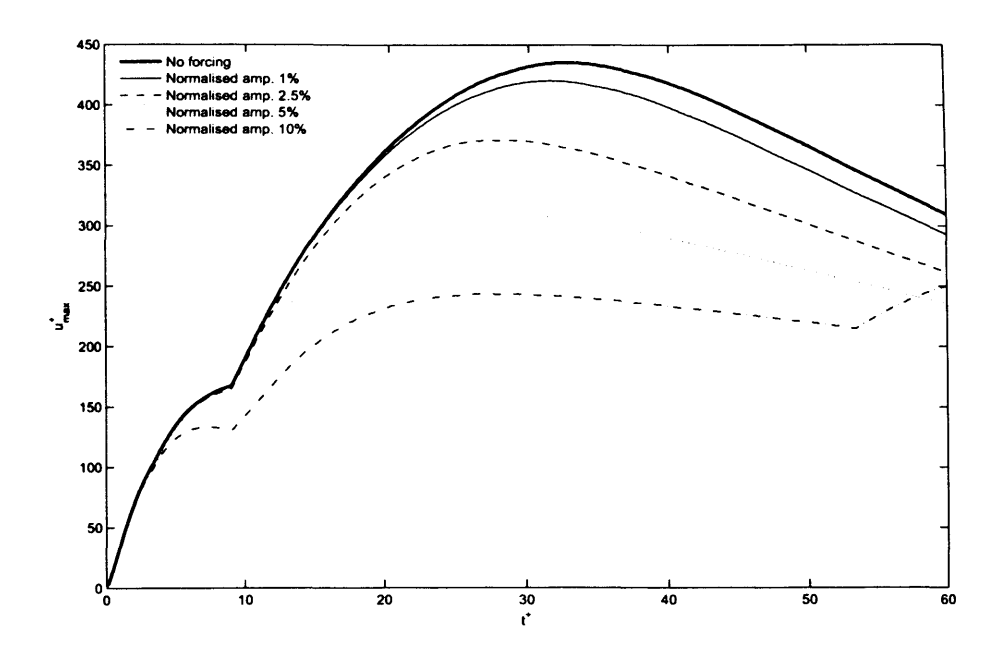


Figure 6.41: Development of streak magnitude in time for the optimum streak for a range of spanwise sawtooth wall oscillation magnitudes. $T^+ = /250$. $\phi = 0$ in all cases

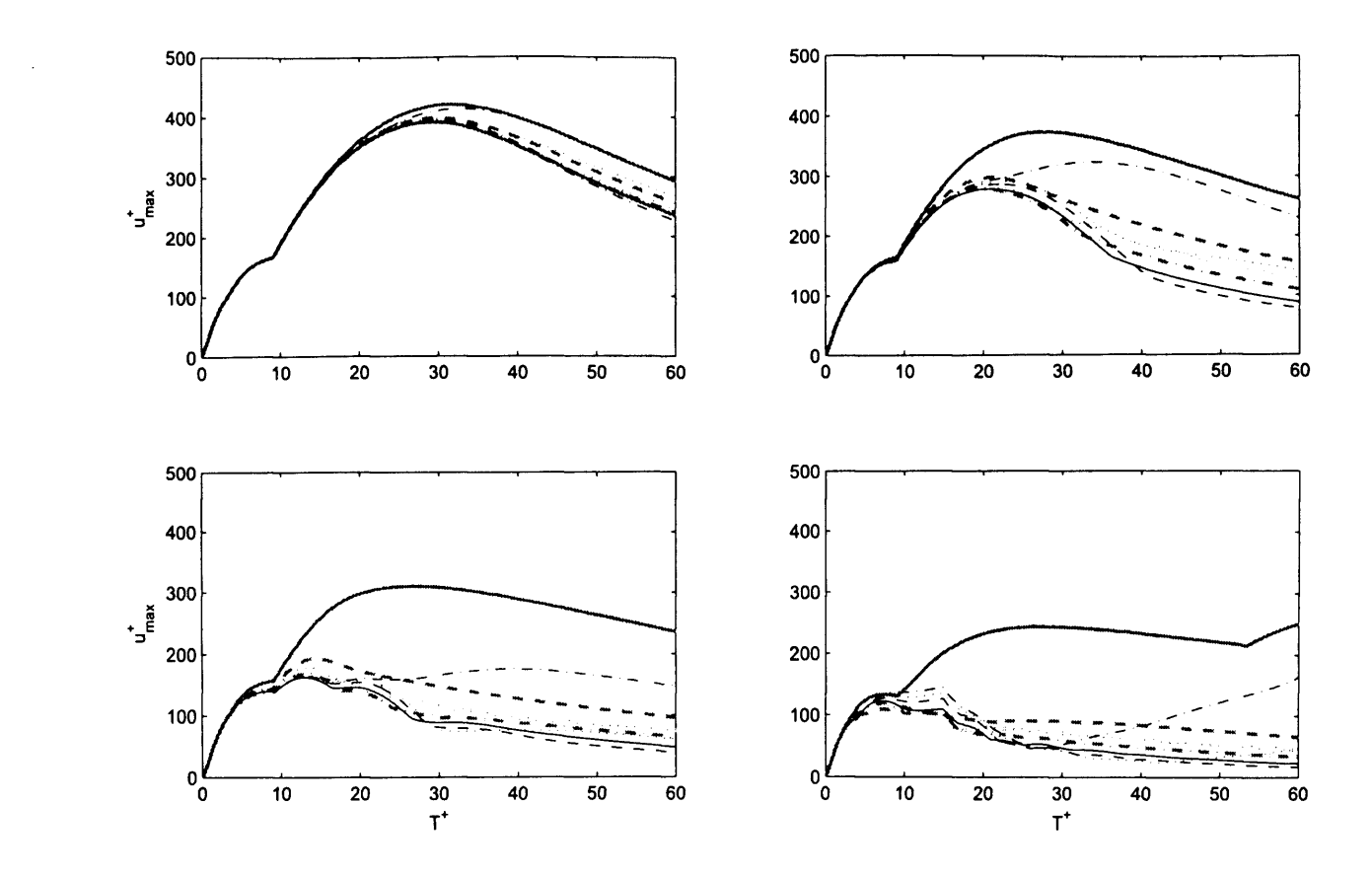


Figure 6.42: Development of streak magnitude in time for the streak with $\lambda^+=75$ for a variety of wall oscillations with a sawtooth profile and $T^+=250$. Different frames show different forcing amplitudes. Clockwise from top left: amplitude 1%, amplitude 2.5%, amplitude 10%, amplitude 5%. Within each frame, different plots show different phases ϕ : solid grey $\phi=0$, dashed grey $\phi=\pi/6$, dotted grey $\phi=\pi/4$, dash-dotted grey $\phi=\pi/3$, solid black $\phi=\pi/2$, dashed black $\phi=2\pi/3$, dotted black $\phi=3\pi/4$, dash-dotted black $\phi=5\pi/6$.

A high-level summary of the effects of changing the oscillatory profile is depicted in figure 6.43. We see that changing the profile of the wall oscillation can alter the effectiveness of the wall forcing in inhibiting streak development. Both the square-wave and sawtooth profiles cause a stronger reduction in maximum streak strength than the sinusoidal profile for periods near the optimum, and there is little to choose between them in this region. For longer periods, however, we find that although the sawtooth oscillation still produces greater strength reductions than the sinusoidal oscillation, the difference between the square-wave and sinusoidal profiles gradually reduces. Indeed, for periods $T^+ > 100$, the square-wave oscillation is less effective than the sinusoidal.

We find, then that careful tailoring of the oscillatory profile can indeed provide stronger streak reduction than the naive implementation of a sinusoidal oscillation. It is possible, of course, that there are other profiles that are yet more effective than those described here, since we have not performed a systematic search of all possible oscillatory profiles. Nonetheless, the same general trends are found regardless of the exact profile used, down to the optimum value of T^+ for the amplitude 1% oscillation, so it seems unlikely that gross changes in results are possible by fine-tuning the oscillatory profile.

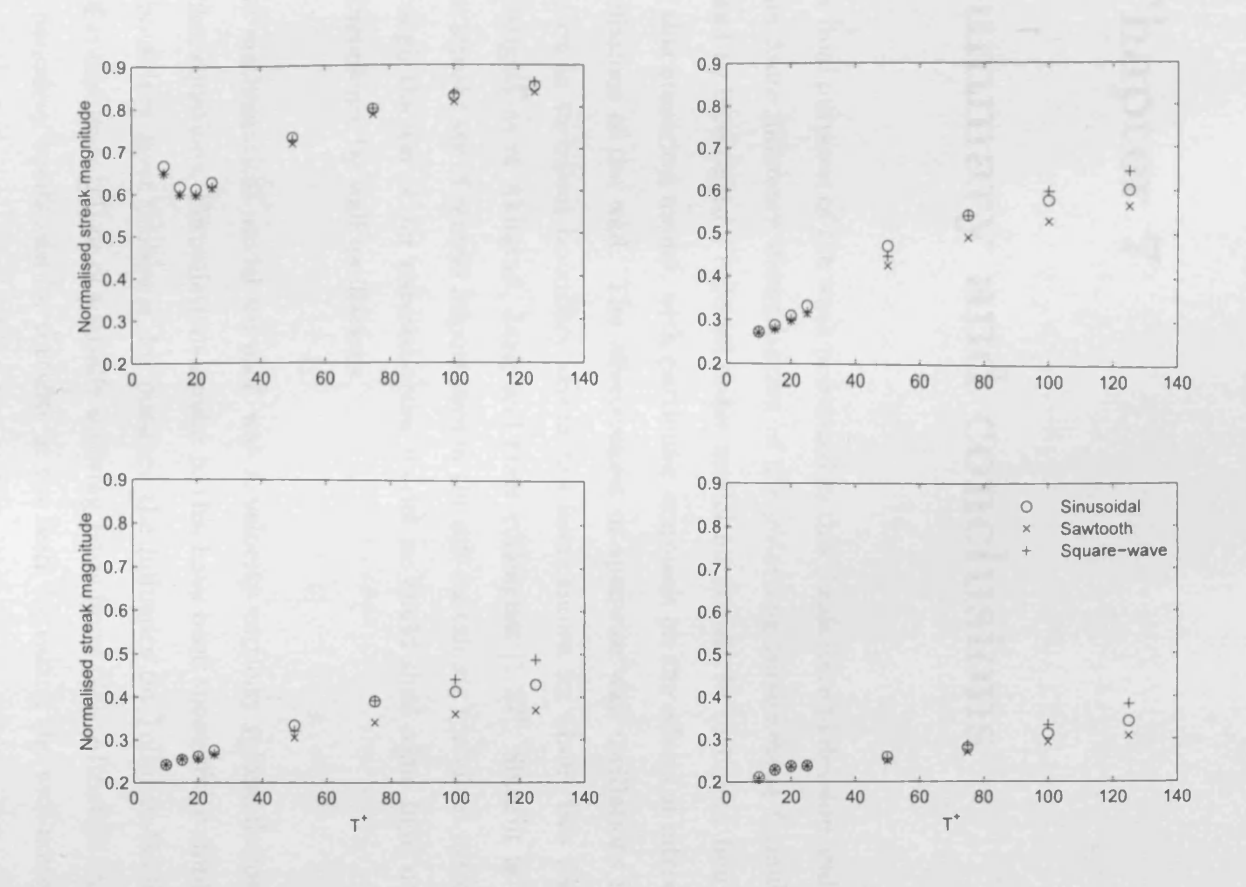


Figure 6.43: Dependence of the maximum streak strength attained in various wall oscillation cases with wall oscillation. Streak strength is expressed as a fraction of the streak strength attained for the optimum streak ($z_f^+ = 12.5, \lambda^+ = 75$) in the unforced case.

Chapter 7

Summary and conclusions

The dual purposes of the work presented in this thesis were to develop and validate a high-order finite difference discretisation of the governing equations as formulated in chapter 2, and to investigate a reduced-order model for streaks in turbulent boundary layers using this numerical model, with particular emphasis on the effects of introducing spanwise oscillations of the wall. The effectiveness of spanwise wall oscillations in reducing wall friction in turbulent boundary layers has been known for about two decades, since the investigations of Akhavan, Jung and their colleagues [1,37]. Since it is widely accepted that streaks are of central importance in the self-sustaining turbulent cycle, we hoped that through the use of our reduced-order model we could shed some light on the disruption of turbulence by wall oscillations.

The mathematical model we used was a velocity-vorticity reformulation of the Navier-Stokes equations. Formulations similar to this have been successfully employed for a range of boundary layer problems, for instance the influence on Tollmien-Schlichting waves of wall compliance [21] or of spatially evolving basis flows [26]. Although there are no natural boundary conditions for vorticity at the wall, by taking the wall-normal dimension to be semi-infinite, we can apply an integral constraint on vorticity across the entire domain which is fully equivalent to the no-slip conditions on velocity. Another useful feature of this set of six equations (the three components of the vorticity transport equations

plus the three velocity Poisson equations that formally close the system, see equations 2.3 and 2.5) is that it is only necessary to solve three of them. The remaining variables can be defined in terms of the variables which are calculated explicitly; see equations 2.12.

The numerical treatment of the governing equations centred around the use of fourthorder compact finite diffences. This allowed a relatively high-accuracy discretisation,
while retaining a narrow grid stencil. This means that our higher accuracy is achieved
without an increase in computational effort. The same compact finite difference scheme
used to discretise the wall-normal and streamwise derivatives was adapted to treat the
integral conditions and the numerical quadrature used to calculate the secondary variables. In the spanwise dimension we perform a Fourier decomposition and take only a
single mode. A fully implicit iterative scheme was employed to advance the solution in
time. Chapter 3 explains the numerical scheme in more detail.

By decoupling the solvers for the vorticity transport equation and the Poisson equation, then testing them with analytic solutions, we were able to verify the order of accuracy of our numerical scheme. Posing a problem with an analytic solution for the coupled system of equations is not so straightforward; instead, we tested the coupled solver against a more realistic problem: the generation of Tollmien-Schlichting waves. The performance of the solver in this test problem is discussed in some detail in chapter 4, but in summary we can say that the results obtained were satisfactory, particularly in that the solver was shown to be robust up to a Reynolds number of 10⁶.

The reduced-order model of the streaks treated them, in a sense, as of a kind with the Tollmien-Schlichting waves; that is, as linearised perturbations to a known basis solution. Of course, a different basis flow was used: the streaks develop on a parallelised mean turbulent flow rather than a parallelised Blasius (i.e., laminar) profile. The other principal difference was the forcing used to generation the perturbations. Instead of a continuous, time-harmonic forcing, the streak were generated with a non-physical source of stream-

wise vorticity. This source was meant to be generically pointlike, in the hope that there existed spatial and temporal limits of sensitivity; by this we mean scales below which the streak response would not substantially alter if the fine details of the forcing were changed.

Our results indicated that such limits did not exist in a straightforward sense. Only if we fix a temporal scale for the forcing does a sensitivity limit on the spatial extent of the forcing become apparent, and vice versa. Within the practical resolution limits of our solver, then, it seems impossible to find a generic pointlike force for the generation of streaks, at least using Gaussian distributions of the form that we considered. We concluded that it was necessary to impose some sort of scale on the forcing based on empirical data; this is discussed in more detail in chapter 5.

Since our formulation is restricted to a single spanwise wavenumber, we needed to determine which wavenumber would best model real streaks. The details of this determination are available in section 5.1; suffice it to say here that we found an optimum spanwise spacing $\lambda^+ = 75$, which is on the low end of experimental measures of the mean streak spacing [82], but very close to the observed median spacing $\lambda^+ = 80$ [71]. It is reasonable that our simulations would pick out the median rather than the mean streak spacing, since the optimum (i.e., most strongly amplified) streak will be the streak that is most often seen in a turbulent boundary layer. This analysis is contingent on the assumption that the forcings which generate streaks of different spanwise spacing are approximately equally likely to occur.

We incorporated spanwise forcing by solving the governing equations twice. The first solution was spanwise uniform, and the only excitation was a spanwise oscillation of the walls. This solution therefore approximated a Stokes oscillatory solution; it was not identical to this because the amplitude of the oscillation varied along the streamwise direction. As shown in section 6.1, the solution we obtain under these circumstances using our linear formulation is identical to the nonlinear formulation. By adding this solution to our orig-

inal parallelised boundary layer solution, we create a modified basis flow. If we then solve the governing equations a second time on this new secondary basis using the same forcing parameters that generate the optimum streak, we can observe how the introduction of spanwise forcing alters the streak response.

Our initial investigation employed an oscillation of period $T^+=250$; since our streaks typically reach their maximum after 30-40 wall units have elapsed from the switching-on of the forcing, the point in the wall cycle at which the streak forcing is introduced will significantly change the basis on which the streak develops during its lifetime. We measure this by a phase angle, ϕ , between the nominal start of the wall cycle and the forcing switch-on. As can be seen in figure 6.3, altering ϕ can significantly influence the streak development, particularly for higher amplitudes.

The observation of apparent delayed streak growth in some high-amplitude cases led us to surmise that there were certain parts of the wall cycle more prone to promoting streak growth than others, and this hypothesis was borne out by the results of longer-term simulations, as presented in figure 6.12. We also found that, by freezing the wall oscillation at certain instants, it was possible to find (unphysical) basis flows which supported exponentially growing normal modes. Thus we can say that some of our oscillating basis flows, even if their overall effect is to reduce streak strength, pass through conditions in which they are instantaneously unstable. By tailoring the oscillatory profile so that it spends less time in the unstable conditions, we hoped to be able to improve the performance of the wall oscillations. This is discussed in section 6.5, where we show that some improvement is indeed possible by tweaking the oscillatory profile.

We found that altering the period of the wall oscillation had a number of interesting effects. As a general rule, increasing the frequency of the oscillation resulted in a greater reduction of streak strength, although for the lowest amplitude oscillations an optimum oscillatory period $T^+ = 20$ was apparent. This is significantly lower than the optimum

period for turbulent drag reduction reported in experimental and DNS studies, which implies that there are perhaps multiple mechanisms by which spanwise wall oscillations interfere with the autonomous cycle of turbulence production, rather than the streaks being the only important turbulence-producing structure directly affected.

In the other direction, significantly increasing the period of the wall oscillations produced certain cases where the streaks grew to significantly greater magnitudes than in the unforced case, a factor of 50 being the largest increase observed. It is possible, then, that there are some spanwise wall oscillations which will amplify turbulence rather than reduce it.

A potentially more illuminating way of looking at the cases where we have growth of normal modes (i.e., the frozen basis case) or perturbations that show very strong transient growth and have a normal mode-like form is to consider the stability of the turbulent mean profile. Although it is a well-known result that turbulent profiles are asymptotically stable to any normal mode perturbation at all Reynolds numbers [64], it appears that relatively small stable modifications of this profile (such as our frozen oscillations) can produce a basis flow which supports exponentially growing disturbances. Similarly, we can greatly increase the transient growth factor with a careful choice of oscillatory modification to the turbulent profile.

This suggests a promising area of research into which the results of this thesis could be extended. It is plausible that a more detailed search of the space of profiles formed from the sum of the turbulent mean profile and transverse oscillatory flows might find yet greater transient growth factors, or even a basis flow which can support an exponentially growing quasi-periodic disturbance. Similarly, it would be interesting to explore the space of steady modifications to the turbulent profile (at least that part of the space which can be obtained from freezing wall oscillations, as in section 6.2) to try to determine the minimal modification that still produces exponential growth. There would be additional

interest in investigating whether the conditions for creating an asymptotically unstable modified basis depend on Reynolds number. Perhaps the most promising aspect of these results is that it suggests another mechanism by which turbulence might sustain itself: if at high Reynolds number even small modifications to the mean profile can produce a basis capable of supporting exponential growth, it is easy to see that relatively long-lived structures might create a situation in which smaller perturbations could be rapidly amplified through linear mechanisms.

There are a number of other ways in which this research could be extended: for instance, we could investigate the effects of multiple oscillating panels, or incorporate spanwise varying wall motion, perhaps by applying Floquet theory. Nevertheless, in having applied and validated a novel numerical formulation to the vorticity-velocity equations of fluid motion, and having found a number of interesting results by applying this formulation to a reduced-order model of streaks in a turbulent boundary layer, the work presented in this thesis represents a novel and potentially useful addition to the body of research on turbulent boundary layer flows and their numerical modelling.

Bibliography

- R. Akhavan, W. Jung, and N. Mangiavacchi. Control of Wall Turbulence by High Frequency Spanwise Oscillations. AIAA Paper 93-3282 (Shear Flow Conference, July 6-9, 1993), 1993.
- [2] N. Aubry, P. Holmes, J.L. Lumley, and E. Stone. The dynamics of coherent structures in the wall region of a turbulent boundary layer. *Journal of Fluid Mechanics*, 192:115– 173, 1988.
- [3] A. Baron and M. Quadrio. Turbulent Drag Reduction by Spanwise Wall Oscillations. Applied Scientific Research, 55:311–326, 1996.
- [4] T. Bewley. Flow control: new challenges for a new Renaissance. *Progress in Aerospace Science*, 37:21–58, 2001.
- [5] P.J. Blennerhassett and A.P. Bassom. The linear stability of flat Stokes layers. Journal of Fluid Mechanics, 464:393–410, 2002.
- [6] P.J. Blennerhassett and A.P. Bassom. A Note on the Linear Stability of a Two-Dimensional Stokes Layer. The Quarterly Journal of Mechanics and Applied Mathematics, 60(3):391–396, 2007.
- [7] K.S. Breuer. Control of Turbulent Flows Using Lorentz Force Actuation. Lecture Notes Series Institute for Mathematical Sciences, National University of Singapore -Vol. 8: Transition and Turbulence Control, pages 325-356, 2005.

- [8] K.S. Breuer, J. Park, and C. Henoch. Actuation and control of a turbulent channel flow using Lorentz forces. *Physics of Fluids*, 15(4):897–907, 2004.
- [9] K.M. Butler and B.F. Farrell. Optimal Perturbations and Streak Spacing in Wall-Bounded Turbulent Shear Flow. *Physics of Fluids A*, 5(3):774-777, March 1993.
- [10] B.J. Cantwell. Organized Motion in Turbulent Flow. Annual Review of Fluid Mechanics, 13:457-515, 1981.
- [11] P.W. Carpenter, K.L. Kudar, R. Ali, P.K. Sen, and C. Davies. A deterministic model for the sublayer streaks in turbulent boundary layers for application to flow control. *Philosophical Transactions of the Royal Society A*, 365, 2007.
- [12] S.F. Chernyshenko and M.F. Baig. Streaks and vortices in near-wall turbulence. Philosophical Transactions of the Royal Society A, 363:1097–1107, 2005.
- [13] H. Choi, P. Moin, and J. Kim. Active turbulence control for drag reduction in wall-bounded flows. *Journal of Fluid Mechanics*, 262:75–110, 1994.
- [14] J. Choi, C.-X. Xu, and H. J. Sung. Drag reduction by spanwise wall oscillation in wall-bounded turbulent flows. AIAA Journal, 40(5):842-850, 2002.
- [15] K.-S. Choi. Near-wall structure of a turbulent boundary layer with riblets. *Journal of Fluid Mechanics*, 208:417–458, 1989.
- [16] K.-S. Choi and B.R. Clayton. The mechanism of turbulent drag reduction with wall oscillation. *International Journal of Heat and Fluid Flow*, 22:1–9, 2001.
- [17] K. S. Choi, J. R. DeBisschop, and B. R. Clayton. Turbulent boundary layer control by means of spanwise wall oscillations. *AIAA Journal*, 36(7), 1998.
- [18] D. Coles. The Law of the Wake in the Turbulent Boundary Layer. Journal of Fluid Mechanics, 1:191–226, 1956.

- [19] C. Cossu, G. Pujals, and S. Depardon. Optimal transient growth and very large-scale structures in turbulent boundary layers. *Journal of Fluid Mechanics*, 619:79–94, 2009.
- [20] C. Davies. Numerical simulation of boundary-layer disturbance evolution. *Philosophical Transactions of the Royal Society A*, 363:1109–1118, 2005.
- [21] C. Davies and P.W. Carpenter. Numerical simulation of the evolution of Tollmien-Schlichting waves over finite compliant panels. *Journal of Fluid Mechanics*, 335:361–392, 1997.
- [22] C. Davies and P.W. Carpenter. A Novel Velocity-Vorticity Formulation of the Navier-Stokes Equations with Applications to the Boundary Layer Disturbance Evolution. *Journal of Computational Physics*, 172:119–165, 2001.
- [23] M.R. Dhanak and C. Si. On reduction of turbulent wall friction through spanwise wall oscillations. *Journal of Fluid Mechanics*, 383:175–195, 1999.
- [24] G.M. di Cicca, G. Iuso, P.G. Spazzini, and M. Onorato. Particle image velocimetry of a turbulent boundary layer manipulated by spanwise wall oscillations. *Journal of Fluid Mechanics*, 467:41–56, 2002.
- [25] M. Gad el Hak and F. Hussain. Coherent structures in a turbulent boundary layer. Part 1: generation of 'artificial' bursts. *Physics of Fluids*, 4:774–777, 1986.
- [26] H. Fasel and U. Konzelmann. Non-parallel stability of a flat-plate boundary layer using the complete Navier-Stokes equations. *Journal of Fluid Mechanics*, 221:311– 347, 1990.
- [27] H.F. Fasel. Numerical investigation of the interaction of the Klebanoff-mode with a Tollmien-Schlichting wave. *Journal of Fluid Mechanics*, 450:1–33, 2002.
- [28] J.M Hamilton, J. Kim, and F. Waleffe. Regeneration mechanisms of near-wall turbulent structures. *Journal of Fluid Mechanics*, 287:317–348, 1995.

- [29] D.S. Henningson and S.C. Reddy. On the role of linear mechanisms in transition to turbulence. *Physics of Fluids*, 6(3):1396–1398, 1994.
- [30] N. Hutchins and I. Marusic. Evidence of very long meandering features in the logarithmic region of turbulent boundary layers. *Journal of Fluid Mechanics*, 579:1–28, 2007.
- [31] S. Jeon, H. Choi, J.Y. Yoo, and P. Moin. Space-time characteristics of the wall shear-stress fluctuations in a low-Reynolds-number channel flow. *Physics of Fluids*, 11(10):3084-3094, 1999.
- [32] J. Jeong, F. Hussain, W. Schoppa, and J. Kim. Coherent structures near the wall in a turbulent channel flow. *Journal of Fluid Mechanics*, 332:185–214, 1997.
- [33] J. Jiménez. On the structure and control of near-wall turbulence. *Physics of Fluids*, 6(2):944–953, 1994.
- [34] J. Jiménez, J.C. del Álamo, and O. Flores. The large-scale dynamics of near-wall turbulence. *Journal of Fluid Mechanics*, 505:179–199, 2004.
- [35] J. Jiménez and P. Moin. The minimal flow unit in near-wall turbulence. *Journal of Fluid Mechanics*, 225:213-240, 1991.
- [36] J. Jiménez and A. Pinelli. The autonomous cycle of near-wall turbulence. *Journal of Fluid Mechanics*, 389:335–359, 1999.
- [37] W.J. Jung, N. Mangiavacchi, and R. Akhavan. Suppression of turbulence in wall-bounded flows by high-frequency spanwise oscillations. *Physics of Fluids A*, 4(8):1605–1607, 1992.
- [38] G.E. Karniadakis and Kwing-So Choi. Mechanisms on Transverse Motions in Turbulent Wall Flows. Annual Review of Fluid Mechanics, 35:45-62, 2003.
- [39] N. Kasagi. Progress in direct numerical simulation of turbulent transport and its control. *International Journal of Heat and Fluid Flow*, 19:125–134, 1998.

- [40] J. Kim. Control of turbulent boundary layers. Physics of Fluids, 15(5):1093-1105, 2003.
- [41] J. Kim, P. Moin, and R. Moser. Turbulence statistics in fully developed channel flow at low Reynolds number. *Journal of Fluid Mechanics*, 177:133–166, 1987.
- [42] P.S. Klebanoff. Characteristics of Turbulence in a Boundary Layer With Zero Pressure Gradient. NACA Report 1247, 1953.
- [43] J.C. Klewicki and R.E. Falco. Spanwise vorticity structures in turbulent boundary layers. *International Journal of Heat and Fluid Flow*, 17:363–376, 1996.
- [44] J.S. Kline, W.C. Reynolds, F.A. Schraub, and P.W. Runstadler. The structure of turbulent boundary layers. *Journal of Fluid Mechanics*, 30:741-773, 1967.
- [45] F. Laadhari, L. Skandaji, and R. Morel. Turbulence reduction in a boundary layer by a local spanwise oscillating surface. *Physics of Fluids*, 6(10):3218–3220, 1994.
- [46] M.T. Landahl. On sublayer streaks. Journal of Fluid Mechanics, 212:593-614, 1990.
- [47] S.K. Lele. Compact Finite Difference Schemes with Spectral-like Resolution. *Journal of Computational Physics*, 103:16–42, 1992.
- [48] D.A. Lockerby, P.W. Carpenter, and C. Davies. Control of Sublayer Streaks Using Microjet Actuators. AIAA Journal, 43:1878–1886, 2005.
- [49] I. Marusic. Unravelling turbulence near walls. *Journal of Fluid Mechanics*, 630:1–4, 2009.
- [50] I. Marusic and N. Hutchins. Experimental Study of Wall Turbulence: Implications for Control. Lecture Notes Series Institute for Mathematical Sciences, National University of Singapore - Vol. 8: Transition and Turbulence Control, pages 207-246, 2005.

- [51] I. Marusic, B.J. McKeon, P.A. Monkewitz, H.M. Nagib, A.J. Smits, and K.R. Sreeni-vasan. Wall-bounded turbulent flows at high Reynolds numbers: Recent advances and key issues. *Physics of Fluids*, 22(065103), 2010.
- [52] P. Moin and T. Bewley. Feedback control of turbulence. Applied Mechanics Review, 47(2):S3-S13, 1994.
- [53] P. Moin, T.-H. Shih, D. Driver, and N.N. Mansour. Direct numerical simulation of a three-dimensional turbulent boundary layer. *Physics of Fluids A*, 2(10):1846–1853, 1990.
- [54] M. Onorato, G.M. di Cicca, G. Iuso, P.G. Spazzini, and R. Malvano. Turbulent Boundary Layers and Their Control: Quantitative Flow Visualization Results. Lecture Notes Series Institute for Mathematical Sciences, National University of Singapore - Vol. 8: Transition and Turbulence Control, pages 247–282, 2005.
- [55] P. Orlandi and M. Fatica. Direct simulations of turbulent flow in a pipe rotating about its axis. *Journal of Fluid Mechanics*, 343:43–72, 1997.
- [56] P. Orlandi and J. Jiménez. On the generation of turbulent wall friction. Physics of Fluids, 6(2):634-641, 1994.
- [57] R. L. Panton. Incompressible Flow. John Wiley & Sons, 1984.
- [58] R.L. Panton. Overview of the self-sustaining mechanisms of wall turbulence. *Progress in Aerospace Sciences*, 37:341–383, 2001.
- [59] L. Prandtl. Eine Beziehung zwischen Wärmeaustausch und Strömungswiderstand der Flüssigkeit. Zeitgeschrift Physik, 11:1072–1078, 1910.
- [60] M. Quadrio and P. Ricco. Initial response of a turbulent channel flow to spanwise oscillation of the walls. *Journal of Turbulence*, 4(7), 2003.
- [61] M. Quadrio and P. Ricco. Critical assessment of turbulent drag reduction through spanwise wall oscillations. *Journal of Fluid Mechanics*, 521:251–271, 2004.

- [62] M. Quadrio and S. Sibilla. Numerical simulation of turbulent flow in a pipe oscillating around its axis. *Journal of Fluid Mechanics*, 424:217–241, 2000.
- [63] K. N. Rao, R. Narasimha, and M.A.B. Narayanan. The 'bursting' process in a turbulent boundary layer. *Journal of Fluid Mechanics*, 48(2):339–352, 1971.
- [64] W.C. Reynolds and W.G. Tiederman. Stability of turbulent channel flow, with application to Malkus's theory. *Journal of Fluid Mechanics*, 27(2):253-272, 1967.
- [65] P. Ricco and M. Quadrio. Wall-oscillation conditions for drag reduction in turbulent channel flow. *International Journal of Heat and Fluid Flow*, 29(4):891–902, 2008.
- [66] P. Ricco and S. Wu. On the effects of lateral wall oscillations on a turbulent boundary layer. Experimental Thermal and Fluid Science, 29:41-52, 2004.
- [67] S.K. Robinson. Coherent Motions in the Turbulent Boundary Layer. *Annual Review of Fluid Mechanics*, 23:601–639, 1991.
- [68] H. Schlichting and K. Gersten. Boundary Layer Theory (8th Revised and Enlarged Edition). Springer-Verlag, 2000.
- [69] P.J. Schmid and D.S. Henningson. Stability and Transition in Shear Flows. Springer-Verlag, 2001.
- [70] W. Schoppa and F. Hussain. Coherent structure generation in near-wall turbulence. Journal of Fluid Mechanics, 453:57–108, 2002.
- [71] C.R. Smith and S.P. Metzler. The characteristics of low-speed streaks in the near-wall region of a turbulent boundary layer. *Journal of Fluid Mechanics*, 129:27–54, 1983.
- [72] D.B. Spalding. A Single Formula for the "Law of the Wall". Journal of Applied Mechanics, 28:455-458, 1961.

- [73] C.G. Speziale. On the Advantages of the Vorticity-Velocity Formulation of the Equations of Fluid Dynamics. *Journal of Computational Physics*, 73:476–480, 1987.
- [74] J.D. Swearingen and R.F. Blackwelder. The growth and breakdown of streamwise vortices in the presence of a wall. *Journal of Fluid Mechanics*, 182:255–290, 1987.
- [75] C. Thomas. Numerical simulations of disturbance development in rotating boundary-layers. PhD thesis, 2007.
- [76] L.N. Trefethen, A.E. Trefethen, S.C. Reddy, and T.A. Driscoll. Hydrodynamic Stability Without Eigenvalues. Science, 261:578–584, July 1993.
- [77] G. Vittori and R. Verzicco. Direct simulation of transition in an oscillatory boundary layer. *Journal of Fluid Mechanics*, 371:207–232, 1998.
- [78] F. Waleffe. Exact coherent structures in channel flow. Journal of Fluid Mechanics, 435:93-102, 2001.
- [79] F. Waleffe. On a self-sustaining process in shear flows. Physics of Fluids, 9(4):883–900, 2007.
- [80] X. Wu and P. Moin. Direct numerical simulation of turbulence in a nominally zeropressure-gradient flat-plate boundary layer. *Journal of Fluid Mechanics*, 630:5–41, 2009.
- [81] J. Xu, S. Dong, M.R. Maxey, and G.E. Karniadakis. Turbulent drag reduction by constant near-wall forcing. *Journal of Fluid Mechanics*, 582:79–101, 2007.
- [82] M. Zacksenhouse, G. Abramovich, and G. Hetsroni. Automatic spatial characterization of low-speed streaks from thermal images. Experiments in Fluids, 31:229–239, 2001.

